1995

A new particle image velocimetry technique for three-dimensional flows.

Satya. Kurada
University of Windsor

National Library of Canada

Acquisitions and Bibliographic Services Branch

395 Wellington Street
Ottawa, Ontario
K1A 0N4

Bibliothèque nationale du Canada

Direction des acquisitions et des services bibliographiques

395, rue Wellington
Ottawa (Ontario)
K1A 0N4

Your file Votre référence

Our file Notre référence

NOTICE

The quality of this microform is heavily dependent upon the quality of the original thesis submitted for microfilming. Every effort has been made to ensure the highest quality of reproduction possible.

If pages are missing, contact the university which granted the degree.

Some pages may have indistinct print especially if the original pages were typed with a poor typewriter ribbon or if the university sent us an inferior photocopy.

Reproduction in full or in part of this microform is governed by the Canadian Copyright Act, R.S.C. 1970, c. C-30, and subsequent amendments.

AVIS

La qualité de cette microforme dépend grandement de la qualité de la thèse soumise au microfilmage. Nous avons tout fait pour assurer une qualité supérieure de reproduction.

S'il manque des pages, veuillez communiquer avec l'université qui a conféré le grade.

La qualité d'impression de certaines pages peut laisser à désirer, surtout si les pages originales ont été dactylographiées à l'aide d'un ruban usé ou si l'université nous a fait parvenir une photocopie de qualité inférieure.

La reproduction, même partielle, de cette microforme est soumise à la Loi canadienne sur le droit d'auteur, SRC 1970, c. C-30, et ses amendements subséquents.

Canada

A NEW PARTICLE IMAGE VELOCIMETRY TECHNIQUE FOR THREE-DIMENSIONAL FLOWS

by

Satya Kurada

A Dissertation
Submitted to the Faculty of Graduate Studies and Research
through the Department of Mechanical and Materials Engineering
in Partial Fulfillment of the Requirements for
the Degree of Doctor of Philosophy at the
University of Windsor

Windsor, Ontario, Canada

ISBN 0-612-01462-2

Satya Kurada

Name MECHANICAL E...

Dissertation Abstracts International is arranged by broad, general subject categories. Please select the one subject which most nearly describes the content of your dissertation. Enter the corresponding four-digit code in the spaces provided.

SUBJECT TERM

SUBJECT CODE 0548

U·M·I

Subject Categories

THE HUMANITIES AND SOCIAL SCIENCES

COMMUNICATIONS AND THE ARTS

Architecture 0729
Art History 0377
Cinema 0900
Dance 0378
Fine Arts 0357
Information Science 0723
Journalism 0391
Library Science 0399
Mass Communications 0708
Music 0413
Speech Communication 0459
Theater 0465

EDUCATION

General 0515
Administration 0514
Adult and Continuing 0516
Agricultural 0517
Art 0273
Bilingual and Multicultural 0282
Business 0688
Community College 0275
Curriculum and Instruction 0727
Early Childhood 0518
Elementary 0524
Finance 0277
Guidance and Counseling 0519
Health 0680
Higher 0745
History of 0520
Home Economics 0278
Industrial 0521
Language and Literature 0279
Mathematics 0280
Music 0522
Philosophy of 0998
Physical 0523
Psychology 0525
Reading 0535
Religious 0527
Sciences 0714
Secondary 0533
Social Sciences 0534
Sociology of 0340
Special 0529
Teacher Training 0530
Technology 0710
Tests and Measurements 0288
Vocational 0747

LANGUAGE, LITERATURE AND LINGUISTICS

Language
- General 0679
- Ancient 0289
- Linguistics 0290
- Modern 0291

Literature
- General 0401
- Classical 0294
- Comparative 0295
- Medieval 0297
- Modern 0298
- African 0316
- American 0591
- Asian 0305
- Canadian (English) 0352
- Canadian (French) 0355
- English 0593
- Germanic 0311
- Latin American 0312
- Middle Eastern 0315
- Romance 0313
- Slavic and East European 0314

PHILOSOPHY, RELIGION AND THEOLOGY

Philosophy 0422
Religion
- General 0318
- Biblical Studies 0321
- Clergy 0319
- History of 0320
- Philosophy of 0322

Theology 0469

SOCIAL SCIENCES

American Studies 0323
Anthropology
- Archaeology 0324
- Cultural 0326
- Physical 0327

Business Administration
- General 0310
- Accounting 0272
- Banking 0770
- Management 0454
- Marketing 0338

Canadian Studies 0385
Economics
- General 0501
- Agricultural 0503
- Commerce-Business 0505
- Finance 0508
- History 0509
- Labor 0510
- Theory 0511

Folklore 0358
Geography 0366
Gerontology 0351
History
- General 0578
- Ancient 0579
- Medieval 0581
- Modern 0582
- Black 0328
- African 0331
- Asia, Australia and Oceania 0332
- Canadian 0334
- European 0335
- Latin American 0336
- Middle Eastern 0333
- United States 0337

History of Science 0585
Law 0398
Political Science
- General 0615
- International Law and Relations 0616
- Public Administration 0617

Recreation 0814
Social Work 0452
Sociology
- General 0626
- Criminology and Penology 0627
- Demography 0938
- Ethnic and Racial Studies 0631
- Individual and Family Studies 0628
- Industrial and Labor Relations 0629
- Public and Social Welfare 0630
- Social Structure and Development 0700
- Theory and Methods 0344

Transportation 0709
Urban and Regional Planning 0999
Women's Studies 0453

THE SCIENCES AND ENGINEERING

BIOLOGICAL SCIENCES

Agriculture
- General 0473
- Agronomy 0285
- Animal Culture and Nutrition 0475
- Animal Pathology 0476
- Food Science and Technology 0359
- Forestry and Wildlife 0478
- Plant Culture 0479
- Plant Pathology 0480
- Plant Physiology 0817
- Range Management 0777
- Wood Technology 0746

Biology
- General 0306
- Anatomy 0287
- Biostatistics 0308
- Botany 0309
- Cell 0379
- Ecology 0329
- Entomology 0353
- Genetics 0369
- Limnology 0793
- Microbiology 0410
- Molecular 0307
- Neuroscience 0317
- Oceanography 0416
- Physiology 0433
- Radiation 0821
- Veterinary Science 0778
- Zoology 0472

Biophysics
- General 0786
- Medical 0760

EARTH SCIENCES

Biogeochemistry 0425
Geochemistry 0996
Geodesy 0370
Geology 0372
Geophysics 0373
Hydrology 0388
Mineralogy 0411
Paleobotany 0345
Paleoecology 0426
Paleontology 0418
Paleozoology 0985
Palynology 0427
Physical Geography 0368
Physical Oceanography 0415

HEALTH AND ENVIRONMENTAL SCIENCES

Environmental Sciences 0768
Health Sciences
- General 0566
- Audiology 0300
- Chemotherapy 0992
- Dentistry 0567
- Education 0350
- Hospital Management 0769
- Human Development 0758
- Immunology 0982
- Medicine and Surgery 0564
- Mental Health 0347
- Nursing 0569
- Nutrition 0570
- Obstetrics and Gynecology 0380
- Occupational Health and Therapy 0354
- Ophthalmology 0381
- Pathology 0571
- Pharmacology 0419
- Pharmacy 0572
- Physical Therapy 0382
- Public Health 0573
- Radiology 0574
- Recreation 0575
- Speech Pathology 0460
- Toxicology 0383

Home Economics 0386

PHYSICAL SCIENCES

Pure Sciences

Chemistry
- General 0485
- Agricultural 0749
- Analytical 0486
- Biochemistry 0487
- Inorganic 0488
- Nuclear 0738
- Organic 0490
- Pharmaceutical 0491
- Physical 0494
- Polymer 0495
- Radiation 0754

Mathematics 0405
Physics
- General 0605
- Acoustics 0986
- Astronomy and Astrophysics 0606
- Atmospheric Science 0608
- Atomic 0748
- Electronics and Electricity 0607
- Elementary Particles and High Energy 0798
- Fluid and Plasma 0759
- Molecular 0609
- Nuclear 0610
- Optics 0752
- Radiation 0756
- Solid State 0611

Statistics 0463

Applied Sciences

Applied Mechanics 0346
Computer Science 0984
Engineering
- General 0537
- Aerospace 0538
- Agricultural 0539
- Automotive 0540
- Biomedical 0541
- Chemical 0542
- Civil 0543
- Electronics and Electrical 0544
- Heat and Thermodynamics 0348
- Hydraulic 0545
- Industrial 0546
- Marine 0547
- Materials Science 0794
- Mechanical 0548
- Metallurgy 0743
- Mining 0551
- Nuclear 0552
- Packaging 0549
- Petroleum 0765
- Sanitary and Municipal 0554
- System Science 0790

Geotechnology 0428
Operations Research 0796
Plastics Technology 0795
Textile Technology 0994

PSYCHOLOGY

General 0621
Behavioral 0384
Clinical 0622
Developmental 0620
Experimental 0623
Industrial 0624
Personality 0625
Physiological 0989
Psychobiology 0349
Psychometrics 0632
Social 0451

To

My Wife Shanti

and

My Parents

ABSTRACT

A technique has been developed whereby the three-dimensional (3-D) motion of particles in a fluid flow is automatically analyzed. A CCD (Charge Coupled Device) camera was used in conjunction with a tri-split lens and a mirror arrangement to simultaneously record stereo and orthogonal views of the particle-seeded flow field. A two-stage calibration algorithm has been implemented to determine the coefficients for each view separately. The images were digitally enhanced to aid in separating the particles from the background. Algorithms were developed to match individual particles in the stereo and orthogonal views. The positional information obtained from the stereo views was used to match the particle images in orthogonal views. A 3-D cross-correlation algorithm has been implemented to follow the particles from frame to frame and compute the velocity vectors. Experiments have been carried out to obtain the velocity profiles in a cubical test section. The results obtained from the experimental investigation were compared with numerical simulation data obtained from FLUENT and STAR-CD.

ACKNOWLEDGEMENTS

I wish to express my sincere gratitude to Dr. K. Sridhar and Dr. G.W. Rankin for their excellent guidance and continuous support. They have been a great source of inspiration to me over the years. I would also like to thank Dr. W.P.T. North, Dr. J. Soltis and Dr. N.W. Wilson for their expertise and encouragement.

Phil and Rambod were a great help and were always there when I needed them. Their advice proved to be invaluable and their humour kept me going during the hard times. I am thankful to Dinakara, Somasundhar, Hugh and Vijayakanthan for their helpful suggestions and their willingness to spend time. I would also like to acknowledge the technical help of Bob Tattersall in constructing the experimental facility.

Thanks are also due to Dr. Lakshmi Sridhar, whose interest and motivation went a long way in helping me finish my thesis. I appreciate the love, support and understanding provided by my family throughout the duration of this study.

The work was financially supported through Natural Science and Engineering Research Council of Canada Grant Numbers A-2190 and A-1403.

TABLE OF CONTENTS

LIST OF FIGURES

LIST OF TABLES

NOMENCLATURE

A	Vector of unknown coefficients
{*a*'s}	Calibration coefficients for view 1
B	Bias
{*b*'s}	Calibration coefficients for view 2
{*c*'s}	Calibration coefficients for view 3
(C_x, C_y)	Centre of image frame co-ordinates
d_p	Distance between particle images
d_r	Fringe spacing
d_i	Distance of the filtering hole from the optical axis
E	Average deviation
f	Focal length of the converging lens
f_n	Fringe number
f_t	Focal length of the transform lens
F_x	Uncertainty of the image scale factor
g	grey scale values
k	Radial distortion
L	Characteristic length
{l's}	Least square coefficients
M	Magnification of the imaging system
M_X	Maximum deviation in *X*-direction

M_Y	Maximum deviation in *Y*-direction
M_Z	Maximum deviation in *Z*-direction
N	Number of points considered
n	Iteration number
N_s	Number of pixels along horizontal direction of sensor
N_f	Number of pixels along horizontal direction of frame buffer
P	Precision
p	tangential distortion
px	Pixel size in the horizontal direction
py	Pixel size in the vertical direction
r	Radius from centre of the image plane to the image point
S	Shift function
S_x	Standard deviation
$t_{v,P}$	Student-t distribution
Δt	Time interval
{u}	Coefficients of a 3x3 mask
w	Homogeneous parameter
(X,Y,Z)	World co-ordinate system
(x_s, y_s)	Sensor co-ordinates
(x_f, y_f)	Frame buffer co-ordinates
(x'_c, y'_c)	Corrected image co-ordinates
(x_p, y_p)	Probable position

Z_c	Closest allowable distance from object to optical system
Z_f	Farthest allowable distance from object to optical system
μ	Absolute viscosity
ρ	Density
ψ	Error criterion
ϕ	Cross-correlation function
λ	Wavelength of light

CHAPTER I Introduction

1.1 Background

Flow visualization provides insight into the physical processes of complex flow fields and helps in the interpretation of local probe measurements. This approach is successful in assigning broad boundaries to the parameters of the problem. However, the qualitative nature of flow visualization is not sufficient to provide detailed information. Furthermore, it is impossible to validate numerical studies using the qualitative data. This has initiated research on various quantitative aspects of flow visualization as applied to fluid velocity measurement.

Among the flow measurement techniques, laser Doppler anemometry (LDA) is now a standard means of measuring fluid velocities. In LDA, the fluid velocity can be measured accurately as a function of time but only at a single point. A number of scanning laser

Doppler velocimetry (LDV) systems have been developed, and more recently there have been efforts to develop multi-point LDV systems with up to six measuring volumes. These systems are limited by two factors: the cost and the difficulties involved in the simultaneous measurement of three velocity components.

The devices that have contributed tremendously to the understanding of fluid motion include interferometer, schlieren and shadowgraph. The principle of these devices involve path integration and hence cannot be used for characterizing the details of complex or unsteady flow fields except in limited circumstances. Tomography is just a technique of controlled blurring of parts of the image out of the focal plane. Computed tomography is a method of determining 3-D information and involves numerical processing of information from tomographic images (Curry III *et al.*, 1990). Optically computed tomography is a relatively new technique that provides a means for obtaining quantitative information from the above techniques.

In flow tagging methods, a fluid element is tagged at a particular location and the motion of those marked molecules is tracked to obtain quantitative velocity information. Time lines similar to those of the hydrogen bubble technique can be achieved. Early work in this area relied on using a tracer liquid, present in the test fluid, which underwent a reversible photochromic reaction when exposed to ultraviolet light (Popovich and Hummel, 1967). These techniques have not been established as viable tools for quantitative velocity measurement in complex flows.

Another technique which has been used for velocity measurement over the complete plane of interest is laser speckle velocimetry (LSV). Speckle patterns are formed by the interference of light rays scattered from many randomly located sites on the surface (Adrian, 1986). Speckle formation occurs only when the density of the scattering sites is high. The majority of flows dealt with in the literature do not possess a high enough particle concentration to produce speckle and consequently particle images are recorded.

Particle image velocimetry (PIV), which has emerged in the past decade as an important tool in fluid velocity measurement is a logical extension of flow visualization. The basic assumption made is that the motion of particles accurately represents the fluid motion.

The application of PIV to the measurement of fluid velocity consists of two steps: recording and processing (Figure 1.1). There are two types of media that are commonly used to record particle images. Traditional photographic imaging involves the use of a camera in conjunction with light sheet illumination to record particle images. By using multiple views and photogrammetric imaging, traditional photographic techniques can be extended to achieve 3-D measurements. Secondly, holographic imaging can also be used to record the displacements of particles in three-dimensions.

In photogrammetric imaging, either stereoscopic or orthogonal images are recorded depending on the orientation of the optical axes (Figure 1.2). Stereoscopic image pairs are recorded using two adjacent lenses, whose separation is the same as the average spacing of the human eyes. An alternate geometry is the arrangement with perpendicular views. In

this approach, each view virtually gives a direct measurement of two of the three spatial co-ordinates of a tracer, one co-ordinate being common to both views. The 3-D particle locations are determined from the particle image projections on the two recording media and from the geometrical characteristics of the set-up used.

In the second step, the fluid velocity is determined as the ratio of the measured spacing between images of the same particle and the time between exposures. The methods commonly used to convert the information contained in the multiply-exposed photographs to flow field data such as velocity, can be grouped into two categories. In the first category, the distance between particle pairs is evaluated by tracking particles from one frame to another, or by measuring the length of their trace images obtained using a long exposure time. In the second category, the displacement between particle images is determined indirectly from an image which has been transformed in some way. The velocity field is obtained by scanning the image on a point-by-point basis or by viewing the whole field using a filtering technique.

1.2 Motivation

Knowledge of the instantaneous spatial distribution of all three components of velocity plays a significant role in understanding the physical nature of various complex flow phenomena. Such information is much needed for studies of blood flow patterns in the cardiovascular circulatory system of the human body, which could yield valuable information about various diseases. Furthermore, information of this type is needed to

provide benchmark data for the validation of various other experimental and numerical techniques.

The current implementation of the 3-D PIV technique involves photogrammetric recording of particle images. Stereoscopic photography has the advantages of using a simple optical accessory directly attached to the camera, and of requiring access to only one side of the apparatus under study. Even small inaccuracies in image matching may lead to gross misplacement of points along the depth dimension due to the short baseline between the viewpoints. The accuracy of the stereoscopic method can be increased, while retaining most of its advantages, by increasing the distance between the two viewpoints. Perpendicular views are more advantageous as they do not suffer from an intrinsically less accurate dimension as in stereoscopic imaging. The lack of obvious similarities between the two views makes the task of identifying and following individual tracers an arduous one in orthogonal-view photogrammetry. Incorporating stereo and orthogonal views into a photogrammetric system can greatly reduce the complexity in the orthogonal-view matching process and improve the accuracy of the depth measurement. In situations where the observation volume allows it, stereo and orthogonal views can be recorded by a single camera through a suitable split-view system. This eliminates the problem of camera synchronization and reduces the overall cost of the equipment

Velocity information is obtained by processing 3-D data sets corresponding to different time instants. The most commonly used approach involves the tracking of individual particles from frame to frame. Complications arise when tracks cross, requiring specific logic for dealing with the problem. The transformation approach, which involves

transforming information from the spatial domain to the Fourier domain, has been implemented optically and digitally for two-dimensional flows. The possibility of extending these techniques to 3-D flows should be investigated as it would eliminate the problems commonly encountered in tracking.

1.3 Objectives

The overall objectives of the present study are:

1. To develop a photogrammetric system that incorporates both stereoscopic and orthogonal views to record the 3-D particle positions at different time instants.

2. To develop a 3-D cross-correlation algorithm for processing the data sets obtained from the photogrammetric system.

3. To experimentally determine the 3-D flow characteristics of a fluid in a cubical chamber.

4. To compare the experimental measurements with numerical results obtained from two packages, FLUENT (FLUENT Incorporated, Lebanon, NH, USA) and STAR-CD (Computational Dynamics Limited, London, England).

1.4 Overview

This study deals with the development of a hybrid photogrammetric system for the automatic analysis of 3-D particle motion. The visual data from experiments were recorded on a CCD camera via a tri-split lens system, incorporating both stereo and orthogonal

coefficients. After calibration, the system was secured in place for recording the particle images and subsequent determination of their relative motion.

The recorded images were transferred to the computer as digitized matrices of intensity values. First, the digitized images were processed to isolate the particles from the background and locate their centres in the three views. The brightness of the particle image edges was used as a recognition criterion. Next, the particle positions in orthogonal views were combined to yield the 3-D locations. Matching of orthogonal views was accomplished by using the positional information obtained from the stereo views. Similarity of the location along the axis common to both views was incorporated into the matching routine. The last step consists of correlating small cubical regions in the test volume, at different time frames, to obtain the average displacement of the particles in that region.

The method was tested on flow patterns generated in a cubical chamber with an offset inlet and outlet. The flow in the chamber is of interest, as it provides many important internal 3-D flow features. The offset arrangement of the inlet and outlet was made so as to create a strong 3-D flow in the chamber such that the three velocity components have appreciable magnitude. Pliolite particles, with density close to that of water, were used as tracers.

The dissertation is presented in the following format. Chapter 2 includes the literature relevant to the study and a description of the PIV technique with an emphasis on the various recording and processing methods available. The experimental facility used for

recording the 3-D particle location is presented in chapter 3. The methodology used in the present work, with special emphasis on the image enhancement, camera calibration and the 3-D cross-correlation algorithm, is discussed in chapter 4. The system performance and the comparison of the experimental and numerical results are presented in chapter 5. A summary of the significant conclusions of the present work and recommendations for further study are outlined in chapter 6.

CHAPTER II Literature Review

This chapter contains a review of the recording and processing techniques that are employed in particle imaging for quantitative velocity measurement. The advantages and limitations of these techniques for various applications are considered. The general principle of PIV is discussed, followed by an overview of the recording techniques employed in previous studies. The next section deals with processing techniques used in conjunction with these recording techniques.

2.1 Particle Image Velocimetry

Particle imaging techniques involve the interaction between radiation and seed particles resulting in the formation of a particle image. The two optical mechanisms that play an important part are scattering and diffraction. Assuming that the particle is non-absorbing, all of the light that falls within the cross-sectional area of the particle is

scattered. An additional amount of light is diffracted from the edge of the particle. For very large particles, this light is separable from other scattering and is usually neglected. For very small particles the diffraction angle is very large and the diffracted component is no longer separable from the reflected component.

For photographic reasons, large particle sizes are desirable, however, large particle size and density mismatch between the particle and the fluid result in large differences between particle and fluid velocity. The elements of a typical particle imaging system are shown in Figure 2.1. The system consists of a light source to illuminate the particles in the flow field, a flow test section, imaging optics to redirect the scattered light, a recording medium to sense light from the particles and a processing system for analyzing the information in the recording medium. Laser light is often used as the illumination source since it can be easily manipulated by necessary optics to illuminate particles in a thin slice in the flow. Various recording techniques used in the literature are presented in the following section.

2.2 Imaging and Recording Techniques

Two-dimensional particle images can be recorded by using photographic film, photographic plates and high speed video cameras. The primary difference between film and video is the spatial resolution. A typical resolution offered by a video camera is in the range of 512 x 512 to 2048 x 2048 pixels compared with that of a standard 35 mm photographic film (300 lines/mm Kodak Technical Pan) which contains 10500 x 7500 pixels. On the other hand, video cameras provide immediate access to the information

stored in the pixels by means of frame grabbers, and this facilitates the rapid control of experimental conditions. Particles can be imaged onto a photographic medium by using photogrammetric techniques.

2.2.1 Photogrammetry

Photogrammetry provides a means of making three-dimensional measurements of position using images of the flow taken from two distinct camera locations. In order to determine the particle position, certain camera parameters are obtained by calibrating it with respect to some pre-measured points. The required number of points depends on the equation model selected. After the trajectories of individual particle images from each camera are tracked, the next step is to match the location of the same particle in both views. The similarity of the two views in the stereogrammetric approach has led Chang *et al.* (1984) to adopt criteria, such as, colour, size, and brightness to match particles. Maas *et al.* (1993) used an epipolar line to detect the stereo pair. In the orthogonal approach, the task of finding particle pairs can only be performed on the basis of geometrical considerations because of the large difference in the two views. The three-dimensional co-ordinates of each particle are then obtained by using the calibration equations.

2.2.1.1 Stereoscopic Recording

A typical arrangement for recording a stereo pair is shown in Figure 2.2. There is a change in parallax between the views obtained from the two lenses as they are located at slightly different locations. Hence, the relative positions of objects in the near field will

exhibit a greater shift in the two views than the objects in the far field. The depth information is stored in such a way that the human mind can mentally reconstruct the original image in its full three-dimensionality. The stereoscopic approach has the advantage of presenting two images which are so similar that most particles visible in one view will also appear in the other.

Stereoscopic records of neutrally buoyant particles were successfully employed for constructing the detailed numerical history of a turbulent velocity field (Johnson, 1974). The film was read manually by projecting each frame onto graph paper, where the locations of particle image pairs were measured. The above method was modified slightly so that the events in the mapped region could be visualized in great detail. As the process was manual, the amount of work involved was overwhelming and hence not practical. The first attempt to automate the data reduction process was reported by Elkins *et al.* (1977).

The next step in the development of the stereoscopic approach was initiated by photographing the motion of small tracer particles with a medium-speed camera equipped with a Bolex stereo lens (Praturi and Brodkey, 1978). One of the main drawbacks of this work was that the observer had to use a special screen and glasses for stereoscopic viewing. The same technique with minor modifications was used by Tatterson *et al.* (1980) to study the large scale flows in the impeller region of pitched blade turbines.

Sheu *et al.* (1982) computed the precise position of the tracer particles by mathematically correlating the measurements taken from two views. Doi and Miyake

(1983) used three TV cameras located at different points to obtain views from different directions to track spherical polystyrene particles suspended in the flow.

Chang *et al.* (1984, 1985a & 1985b) used a cine camera equipped with a Bolex C-mount stereoscopic lens to photograph the flow. The large uncertainty in the depth dimension was mainly attributed to the small distance between the collection lenses compared with the distance from the scatterers. Kent and Eaton (1982) obtained better depth measurements by using a larger separation between the lenses. One of the drawbacks of the above two experiments is the very low concentration of particles for successful data processing. Brodkey (1986) increased the density by colour coding particles so that the task of tracking and matching in both views of a stereo pair was simplified.

Kasagi *et al.* (1988) refined the stereogrammetric method by automating all the image processing routines. Three CCD cameras located at different angles were used in conjunction with an image processor to obtain the position of a particle at a given time. The three-dimensional position was identified as an intersection of three lines, where each of these lines was determined by a set of collinear equations with known calibration parameters.

Nishino *et al.* (1989) developed a three-camera particle tracking velocimeter for studying laminar and turbulent flows. The three-dimensional position of the tracer particles was obtained as an intersection of the three perspective rays, where a perspective ray is a line passing through the perspective point of the camera and the centroid of the particle

image. Arroyo and Greated (1991) devised a mirror system to record stereoscopic images of the flow with a single camera. The system consisted of a pair of mirrors oriented perpendicular to the illuminated sheet so that the optical axis of the two equivalent lenses was perpendicular to the sheet. A second pair was used to redirect the light so that the two images were formed on the back of the camera, each one on a different half of the film.

Prasad and Adrian (1993) developed a twin-camera stereoscopic system with image shifting to accurately measure three-dimensional velocity fields in liquids. Stereo matching was performed by implementing a new image registration technique, by superposing the two negatives. When these negatives were close to being aligned, a strong Moire pattern appeared and this pattern was very sensitive to small displacements of one negative with respect to the other. Auto-correlation was used to process these negatives to obtain three-dimensional velocity information. Maas *et al.* (1993) developed a three-camera digital photogrammetric system based on particle tracking. Mathematical modelling of the multi-media environment and a thorough calibration of the system were performed.

2.2.1.2 Orthogonal-View Recording

It was found by Gauthier and Reithmuller (1988) that the error in measuring the displacement is minimized when the optical axes are incident at an angle of 45° to the illuminated plane (Figure 2.3). In this approach, the two views are perpendicular to each other, hence the name orthogonal-view photogrammetry. Unlike in the stereoscopic approach, it is extremely difficult for the human mind to correlate the two distinct images obtained from orthogonal views.

Caffyn and Underwood (1952) developed an optical system based on overlapping perpendicular views to measure velocity profiles in liquids by stroboscopic photography of tracers. A travelling microscope was employed to measure the displacement between tracer images on film. Winter (1958) implemented an orthogonal-view approach with separate camera positions to photograph the complex three-dimensional flow field in a free jet. The lack of obvious similarities between the two views made the task of identifying and following individual tracers difficult without computer assistance. Peskin (1972) designed a perpendicular-view optical system to obtain high speed cinematographic records of the motion of tracers through heart valves (in vitro).

Racca and Dewey (1988) correlated the centres of particle images recorded from perpendicular views to obtain the three-dimensional spatial location of tracers. In the absence of parallax, orthogonal pairs (two images, one in each view, that correspond to the same point in space) would have identical positions in the direction common to both views. More accurate results were obtained by applying the parallax correction.

Adamczyk and Rimai (1988) used a cylindrical column of light to illuminate a transparent test section, and viewed it in two orthogonal directions using a pair of synchronized intensified target (SIT) video cameras. The output from camera 1 occupied the right half of the video image, while the output from camera 2 occupied the left half. A precise flow field reconstruction from the two orthogonal vector projections was made by utilizing the transformation functions specifying object-space co-ordinates in terms of their corresponding video projections of each camera.

Kobayashi *et al.*(1989) used two CCD cameras in conjunction with an image processing system to obtain quantitative information about a swirling flow around or between rotating coaxial parallel discs. The uncertainty in the measurement was about 8%. Okamoto *et al.* (1991) used a mirror arrangement to direct the side and bottom views of the test section onto different parts of a single image plane. The upper half of the picture represented the x-z image and the lower half was the x-y image. If only one particle existed at the same x co-ordinate in both the images, its three-dimensional position could be uniquely determined. If more than one particle was present at the same x location, all the positions were considered to be potential particle positions and the most probable was identified using a velocity vector histogram.

2.2.2 Holographic Particle Imaging

A conventional photograph is a record of only the amplitude information of the image projected onto the photographic film, while the phase information is lost. This results in the loss of depth information in the recording process. Holography, however, differs from photography in that both amplitude and phase information are recorded; the phase information is encoded by using a reference beam in addition to light scattered or diffracted from the object.

Holographic velocimetry (HV) is an extension of conventional holography. A major consideration with HV is that the objects of interest are not stationary. This poses a problem in recording a stable interference pattern on the film. Since the object is moving during an exposure interval, the distance travelled by the object wave to the film may also

change, thus altering the interference pattern at the film plane. If the object motion causes a difference in the object path length of greater than one half of a wavelength of the radiation used, the regions of constructive interference become regions of destructive interference and vice versa, causing the hologram to be destroyed.

The first step in holographic imaging is to seed the flow field under study with small spherical particles. When recording the hologram, the first exposure yields the initial three-dimensional particle location. The second exposure produces images of the same particles but in different positions as determined from their corresponding velocities. Re-illumination of the hologram results in reconstructed images from both exposures. As long as the particle pairs are recognizable and distinct from one another, the reconstructed images will allow for measurement of x, y and z displacements. The optical set-ups used in the recording and re-construction processes in HV are shown in Figures 2.4 and 2.5 respectively.

Trolinger *et al.* (1969) were the first to show that multiple exposure holography could be used to study the dynamic properties of particle fields. They altered the intensity of the second pulse with respect to the first so that the second exposure could be differentiated. Menzel and Shoffner (1970) recorded the diffracted images of a spherical particle which consisted of several concentric circular fringes. This facilitated the determination of the particle's spatial position, since the radii of the interference patterns are unique functions of the particle size and the distance from the recording plane.

To reduce the time required for data acquisition, Ewan (1979a & 1979b) proposed a system which extracted velocity information from the optical transform plane of a doubly exposed far-field hologram rather than from the reconstructed image. The intensity pattern in the transform plane contained a set of co-sinusoidal fringes associated with each velocity component. Carder *et al.* (1982) recorded the image of each particle in three-dimensional space on a series of successive holograms with respect to time. Images of particles recorded sequentially on individual holographic frames were reconstructed using an in-line far-field configuration. Malyak and Thomson (1984) examined a method for measuring particle displacements and velocities in the optical Fourier transform plane of an in-line far-field hologram.

Yuan *et al.*(1986) utilized the holographic technique for measuring velocities in a hypersonic wind tunnel (Mach number = 6), where the particles were injected from the hypersonic region into the test section at constant pressure. Schuster and Wagner (1988) recorded holograms of spherical seed particles in an aortic flow chamber using a double pulsed Q-switched Nd:YAG laser, and a continuous wave argon-ion laser was used for reconstruction. The in-plane displacements were easily measured using the reconstructed particle images. The out-of-plane displacement (depth) was obtained by using a combination of image processing and triangulation by allowing for multiple viewing of particle pairs in a rotated co-ordinate system.

2.3 Processing Techniques

Multiply-exposed particle images can be processed either by a manually operated visual system or in an automated environment. The human visual system has tremendous processing power but is incapable of making accurate quantitative comparisons between different segments of the image. Current digital image processing techniques complement our visual system. The images are usually processed on a pixel-by-pixel basis. The application of digital image processing techniques to flow visualization is relatively new and largely motivated by the present emphasis on identifying and classifying large-scale structures in flows.

The particle images to be recorded by a camera constitute an analogue signal. The images are transferred to a high speed analogue-to-digital converter which digitizes the images and stores the pixel information in a buffer memory. The digital information is then transferred at a lower rate from the digital frame buffer to other auxiliary peripheral storage, where it can be accessed for further processing. Two approaches that can be used for accomplishing this processing are discussed in the following sections.

2.3.1 Tracking Approach

It is convenient to track particle images from one frame to another when the displacement of each individual particle image during the exposure interval, is more than its own size, and the density of particles is small enough to prevent overlap. Algorithms to track two-dimensional particle images were successfully implemented by Marko and

Rimai (1985), Khalighi and Lee (1989) and Hassan *et al.*(1992). Tracking of particle images in three-dimensions was performed by Majumdar *et al.* (1987) and Racca and Dewey (1988).

The tracking of particle images from one frame to another involves the following steps. The first step is to enhance the recorded image so that it is suitable for processing. One of the simplest methods of improving the contrast is a linear scaling transformation that normalizes the actual intensity values so that they are distributed over the entire range. In fluid flow applications, the image typically consists of flow tracers and the background.

The next step involves the task of image segmentation. A value of 1 is assigned to particle image pixels and 0 to background pixels. Bright particles in a dark background yield a bimodal intensity histogram and an optimum threshold lies between the peaks. Non-uniform background illumination makes the application of global thresholding techniques inaccurate. The edges of tracers give relatively sharp discontinuities in intensity level. Edge detection techniques such as the Sobel or Robert's operator can be used to detect these edges [Gonzalez and Wintz, 1987]. The particle recognition stage serves to locate the particles in a binary image and acts as a bridge between edge detection and tracking.

Park *et al.* (1989) found, from preliminary analysis, that particles, in the edge detected binary images, usually appeared two or three pixels wide and three or more pixels long. They suggested a method of locating them by examining one column at a

time, sequentially, in the direction of flow. When two or three white pixels were found next to one other, the start of the particle streak was indicated.

Chang *et al.* (1985a & b) accomplished tracking of particle images by establishing a feasible search region, using the time interval between frames and an estimation of the maximum velocity. Basically, the displacement of a particle image cannot exceed a certain value. However, there can be quite a few particles in the feasible region. The second part of the frame-to-frame tracking was to match the same particle in different frames. It was observed that the direction and displacement of the particle did not change drastically but rather gradually between the frames and therefore the slope and displacement were used as tracking criteria.

Racca and Dewey (1988) presented a method which was similar in principle to that used by Chang *et al.*[1985a & b), but several differences existed in the way the search for particle trajectories was continued. Moreover, the method was based on three-dimensional locations obtained from the matching of orthogonal pairs, whereas Chang *et al.*(1985a & b) performed tracking in two-dimensions and then associated similar trajectories in the two views. The process of following a tracer was based on the assumption that the velocity vector of that particle will not change drastically, either in magnitude or direction from one frame to the next. As a first approximation, linear interpolation of the displacement in one time interval was used to predict the path in the next interval. To allow for changes in the velocity vector, a spherical search range was established around the predicted position and the next frame was scanned to see if unassigned particles were present within that range. If any were found, the nearest one to

the predicted position was assigned a successor and the trajectory was extended to it. If none were found, the trajectory was considered lost.

Gharib and Willert (1988) developed a fully automated particle tracing technique. The first step in the analysis of digital images was to define the region of interest. By pre-examination of a sample image, a grey-level threshold was input to determine the minimum pixel value of that would be considered as a trace. In the next step the image was scanned, line by line, to detect the first pixel greater than zero for any potential trace region. The next step was an automatic search inside the trace region for the reference points by scanning the pixel values greater than a computed peak threshold. Once the outline boundary of a reference region was defined in the same fashion that a trace region was defined, the centroid of it was determined and assigned to the corresponding region. The length of the line that connected the reference points was measured as the magnitude of the velocity vector and assigned to the halfway point between the two reference points.

2.3.2 Transformation Approach

Two methods are commonly used to process the multiply-exposed images. The first method is a point-by-point procedure which uses the classical Young's fringe interference phenomenon to accurately determine the local velocity vector. The second method employs Fourier filtering to extract the global distribution of the velocity components.

2.3.2.1 Pointwise Processing

Pointwise processing can be implemented in two ways:

i) **Optical Approach** In this method a small region of the film, over which velocity can be assumed to be constant, is illuminated by a parallel beam of coherent light (Figure 2.6). Each combination of particle images within the interrogation spot of the laser beam forms a system of interference fringes. The random pairings of these particle images produce a fringe pattern which averages to zero. However, those image pairs which move the same distance and in the same direction during exposure will result in interference fringes of same spacing. The fringe spacing is inversely proportional to the distance between the image pairs. The orientation of the fringes is perpendicular to the direction of the movement of particles. The spacing between Young's fringes is given by (Larijani, 1992)

$$d_f = \frac{\lambda f}{d_p} \tag{2.1}$$

where d_f is the fringe spacing, d_p is the distance between particle images, λ is the wavelength of the coherent illumination used and f is the focal length of the converging lens. The magnitude of the velocity is given by (Larijani, 1992)

$$|V| = \frac{\lambda f}{M d_f \Delta t} \tag{2.2}$$

where M is the magnification of the imaging system and Δt is the time interval.

The determination of fringe spacing has been attempted by integrating the fringe pattern along an axis parallel to the orientation, either optically using a cylindrical lens arrangement (Kauffmann et al. 1980), or digitally, using a video camera and an image processor. However, the main disadvantage of the above methods is that the fringes must

be aligned manually before measuring the fringe wavelength. Meynart (1982) used autocorrelation in several directions to determine the fringe spacing and orientation. Pickering and Halliwell (1985) scanned a detector along an axis perpendicular to the fringe orientation to obtain one-dimensional data. However, these results proved to be unreliable due to a poor fringe signal-to-noise ratio. Kirita *et al.*(1986) presented an automated analysis of a fringe pattern by using the cross-correlation between two separated lines of fringe data.

A two-dimensional Fourier transformation of the fringe intensity distribution provides an extremely powerful method for analyzing Young's fringes (Adrian, 1986). In this system, the intensity of the fringes is recorded on an optical device that transmits a coherent wave with an amplitude proportional to fringe intensity. The transmitted wave is Fourier transformed by a lens to form an optical field whose amplitude is proportional to the correlation function. The intensity of this field can be processed by the usual peak detection and centroid calculations.

***ii)* Digital Approach.** In digital processing, a time sequence of images is captured with a high speed camera or video camera with each frame containing a single exposure image. A finite number of such images are sampled in a prescribed time interval. The sampled images are digitized, enhanced and linearly superimposed to construct an image field. This image field is equivalent to a multiply-exposed photograph obtained from the optical processes.

The image field is divided into sub-regions of equal size which are then transformed into the Fourier domain by using a two-dimensional fast Fourier transform (FFT). This produces a pattern equivalent to the Young' s fringes. As in the case of optical processing, the magnitude of the local velocity vector is inversely proportional to the fringe spacing and the fringes are oriented perpendicularly to the direction of the velocity vector. Cho (1989) formulated the equations associated with the digital counterpart of the Young's fringe phenomenon and applied them to a numerically generated flow.

Willert and Gharib (1991) implemented a two-dimensional cross-correlation algorithm for obtaining velocity information. Single exposure images at time t and $t + \Delta t$ were transformed into the Fourier domain by using a two-dimensional FFT. The operation of the cross-correlation in the Fourier domain is the multiplication of one image with the complex conjugate of the other. The resulting image was then transformed back into the spatial domain by using an inverse FFT algorithm. The correlation between the two images indicated a large spike, displaced from the origin, corresponding to a spatial shift of particle images from t to $t + \Delta t$. The velocity information was obtained by measuring this shift (dx and dy) from the origin and dividing it by the known time period.

2.3.2.2 Whole-Field Processing

Whole-field processing can be implemented in two ways:

i) **Optical Approach** [Larijani, 1992]. The spatial or whole-field Fourier filtering technique allows the photograph to be processed in its entirety through the use of the

filtering set-up shown in Figure 2.7. A lens with a focal length f_1 produces the Fourier transform of the multiply-exposed image in its back focal plane where an opaque mask with a circular aperture is located. After bandpass filtering by the aperture, an inverse Fourier transform is performed by a second lens. The filtered image is reconstructed in its back focal plane or the Fourier plane of the second lens. Using this set-up, an operator can observe the evolution of fringes which represent lines of constant velocity component and assign a number to each one of them, as they appear. These fringes are contours of the constant displacement component in the direction of the aperture offset.

The filtering operation blocks all but a small range of frequencies, which corresponds to specific velocity vectors. A filtered image displays fringes which correspond to velocity components in a direction along the line joining the optical axis and the filter hole centre. If di is the distance of the filtering hole from the optical axis, the magnitude is given by:

$$V = \frac{f_t f_n \lambda}{\Delta t d i M} \tag{2.3}$$

where f_t is the focal length of the transform lens, f_n is the fringe number, λ is the wavelength of coherent illumination used, M is the magnification of the imaging system and Δt is the time interval. The u and v component distributions are obtained by recording filtered images for two orthogonal x and y aperture offsets. Low contrast, de-correlation and speckle noise effects are usually worse with the whole-field technique than with the Young's fringe method.

ii) **Digital Approach.** Larijani (1992) developed algorithms to implement the digital whole-field Fourier filtering technique by using computer generated images. Particles were uniformly distributed on a regular grid and their new locations were determined using prescribed flow equations. The multiply-exposed image was then transformed into the frequency domain by using a two-dimensional FFT. A digital approximation to the optical filter was applied to the resulting image. The image was then transformed back into the spatial domain by using a two-dimensional inverse FFT. The resulting fringes are the iso-velocity component contours within the flow field. The particular velocity component represented depends on the location of the passband of the filter relative to the origin. The effects of input variables such as filter shape and location, image resolution and particle size, on the visibility of the whole-field iso-velocity fringes were investigated.

2.4 Quantitative Errors

Error analysis involves the determination of uncertainties in various quantities that lead to the measurement of fluid velocity. The errors that are commonly encountered in the measurement of fluid velocity can be grouped into two categories: recording and processing. The errors encountered in the recording phase are inherent to the visualization procedure. These lead to an incorrect position being associated with a given particle image. The processing errors result from the attempt to translate the particle displacement information into velocities. The recording errors tend to propagate through the processing sequence and may even get amplified.

2.4.1 Recording Errors

The recording errors are classified into three categories: particle location, exposure time and digitization errors.

2.4.1.1 Particle Location

Selecting a correct threshold value, that is separating particles from the background, has been identified as one of the most important operations in obtaining accurate velocity information. Once an appropriate threshold has been selected, the error in locating particles increases with the number of particles, the size of the particles and image noise (Guzennec and Kiritsis, 1989). Those particles associated with a large error correspond to cases of particle overlap, that is two or more particles are detected as one and hence their centres may be off by a distance of the order of a particle radius.

2.4.1.2 Exposure Time

The image capture process requires a small but non-zero time which leads to an uncertainty in the effective duration of the illumination pulse. However, an electronic switching system can be used to control the length of the light pulse so as to minimize the uncertainties.

2.4.1.3 Digitization Error

The accuracy of the digitization process and the resolution of the photographic film determine the precision with which the length of particle traces can be measured. Agui and

Jimenez (1987) tested the repeatability of manual digitization by comparing successive digitization of a single, sharp point. Automatic digitization reduces this error by a factor of two, by eliminating manual positioning uncertainty.

2.4.2 Processing Errors

The processing errors are classified into two categories: tracking and sampling errors.

2.4.2.1 Tracking Errors

Several parameters influence the accuracy of the particle tracking method. In this case, the Lagrangian velocity of the particles is generally used to represent the Eulerian instantaneous velocity vector. This assumption was shown to be a reasonable approximation, if the velocity changes slowly in space and time (Gharib and Willert, 1989). One of the common problems encountered in the tracking process is the erroneous trace length recorded due to the lack of information regarding entrance and exit of the particles from a light sheet (Agui and Jimenez, 1987).

2.4.2.2 Sampling Error

The aliasing problem is common in sampling systems. The Nyquist sampling criterion suggests that the shortest resolvable wavelength in a flow image is twice the average distance between traces. To avoid any trace overlap problem, this average distance is usually set close to the average trace length in the image. Therefore, features of flow with a wavelength shorter than twice the average trace length will be undersampled. Agui and

Jimenez (1987) showed that this error will not affect the mean velocity measurements but contributes significantly to turbulence intensity measurements. Large interpolation errors due to a lack of ideal interpolating methods for randomly distributed samples have been reported (Agui and Jimenez, 1987). In most turbulent flows, these errors were found to range from 20 to 30%. This has been attributed to the fact that the particle traces are much longer compared to the flow scales.

CHAPTER III Experimental Facility

A micro computer based hybrid photogrammetric system for obtaining 3-D position information from a single camera is presented. This system was developed to measure the particle locations in a cubical chamber with an offset inlet and outlet. A tri-split lens was used in conjunction with a CCD camera to simultaneously record three views of the test section. Both stereo and orthogonal views were obtained. A detailed description of the experimental set-up and its various components is presented in the following sections.

3.1 Experimental Set-up

A schematic diagram of the experimental set-up is shown in Figure 3.1. The camera was positioned on a tripod and locked in place by means of threaded screws. The mirrors were mounted on two optical benches, which were bolted to a rigid frame. They were arranged in such a way that the stereo and orthogonal views of the test section are imaged

side-by-side onto the sensor of a CCD camera. The output of the CCD camera was of the NTSC RS-170 video source format. The time interval between captured frames was 1/5 sec and the exposure time was set at 1/500 sec. The digitized image was then stored in the frame buffer for subsequent analysis by a PC-486 micro computer. A photograph of the optical system is shown in Figure 3.2.

3.2 System Components

The hardware components of the 3-D PIV system consists of an imaging system, an image digitization and storage unit, an illumination facility, particles and a data processing unit. To reduce the cost, off-the-shelf components were used as much as possible.

3.2.1 Camera and the Lens System

A Model TM-745 PULNiX CCD camera (PULNiX America Inc., Sunnyvale, CA, USA) with a resolution of 768 by 493 pixels (cell size of 11.0 x 13.0 μm) was used in this study. It is possible to externally control the electronic shutter rate from 1/60 sec. to 1/10000 sec. Shuttering is accomplished by reducing the normal field integration time according to an externally supplied signal. The minimum sensitivity of the camera is 0.5 lux at an f-number of 1.4. The camera was fitted with a Model TL-153 tri-split lens (Visual Methods Inc., Westwood, NJ, USA), which consists of three female C-mounts (Figure 3.3). Three 25 mm lenses were attached to these C-mounts. The tri-split lens provides different scenes with the same or different magnifications on one monitor. Adjustable offset optics enable proper setting of lens and viewing angle without moving the camera.

The lens produces inverted images on the monitor which are transposed by inverting the camera.

3.2.2 Image Digitization and Storage

The entire image analysis, starting with the digitized intensity matrix and ending in a list of centroid co-ordinates of the selected image features, was performed on a micro computer. A photograph of the data processing unit is shown in Figure 3.4. The analogue signal from the camera was then transferred to an EPIX silicon video mux frame grabber (EPIX Inc., Buffalo Grove, Illinois, USA) (with 4 mega bytes of memory on board) which digitized the image into 752 x 480 x 8-bit pixels. Eleven frames can be stored for each triggering in the computer system. The digitized image was displayed on a separate monitor.

3.2.3 Illumination

One of the most important parts of the hardware configuration is the illumination system. In order to obtain adequate scattering from small, moving particles in a 3-D observation volume, the light source must fulfil the following conditions:

- High intensity to enable the use of small tracers.
- Uniform illumination of the entire test volume.

Several lighting devices were tried in this work, with the goal of maximizing light intensity and uniformity while preventing reflections off the walls of the flow chamber

reaching the camera. Two 100W indoor flood lamps were positioned on the top of the test section and a slide projector lamp was located at its bottom so as to illuminate the entire test section uniformly.

3.2.4 Particles

The particles used for flow visualization must meet the following criteria.

- The physical density of the particles should match that of the fluid medium.
- The particles should be spherical and have a reflecting surface.
- They should be small enough to follow the flow and large enough to be made visible under suitable illumination.

In this work, Pliolite particles (Goodyear Chemical, Akron, Ohio, USA) were used. Pliolite is a white opaque plastic with a density of 1020 kg/m^3. In order to obtain particles of desired size (200-250 μm), they were ground and the resultant powder was passed through a series of sieves. Although the particles were not perfectly spherical in shape, their reflection properties proved to be good.

To prevent the particles from sticking to the walls of the test section, they were wetted with a double strength solution of photoflow (Kodak Canada Inc., Toronto, Ontario, Canada) following a procedure given by Altman (1994). This was done by placing them in a large beaker containing the solution and constantly stirring the mixture. After a few hours, the particles were rinsed in water to prevent foaming. They were then kept in a

beaker containing water and left overnight. The particles separated according to their density, and those of appropriate density were selected while the rest were discarded.

3.3 Flow Facility

This section includes a general description of the closed loop flow circuit used in the present study, followed by a discussion of the test section and the test fluid used in the study.

3.3.1 General Test Facility

An existing flow facility was modified for the present study. This closed loop design permitted the particles to be recirculated. A schematic diagram of the test flow facility is shown in Figure 3.5. The test fluid contained in a 50 cm x 50 cm x 30 cm reservoir was pumped by a small centrifugal pump (1/25 HP) to an upstream constant head tank. The constant head tank (made of Plexiglas) had a diameter of approximately 43 cm, height of 25 cm, and had a 5 cm diameter overflow tube located at the centre.

The upstream tank was fastened to a steel I beam located near the ceiling (about 5 m from the floor). The overflow from the upstream tank was returned to the reservoir. The upstream tank was connected, through a flow meter (provided with a regulating valve), to the inlet tube of the test section by means of a flexible tubing. The test section was positioned on a frame attached to a three-axes translation table, with high precision anti-backlash ball screws used as motion actuators. This facilitated the positioning of the test section, making it visible in all the three views. The flow meter was calibrated by

passing a steady flow of water through it, and the time required for a certain mass of fluid to be collected was recorded. The calibration curve is given in Appendix A.

3.3.2 Test Section

The test section was a cubical chamber (10 x 10 x 10 cm^3) with offset inlet and outlet ducts shown in a horizontal position in Figure 3.6. When installed in the test facility the inlet and outlet tubes were vertical to optimize optical accessibility. The offset arrangement of the inlet and outlet caused a strong three-dimensional flow in the chamber such that all the three velocity components had significant magnitudes at various locations within the test section. The inlet duct (made of Plexiglas) had a cross-section of 2 cm x 2 cm and was located at the bottom left-hand corner, near the front. The outlet duct had the same cross-section as the inlet and was located at the top right-hand corner, near the back. The two ducts were located at a distance of 1 cm from their neighbouring edges. Figure 3.7 indicates the placement of the outlet and the inlet on the top and the bottom surfaces. Both inlet and outlet ducts had a length of 50 cm to generate the fully developed condition. An average inlet flow velocity of 2 cm/s was set in the present study. The Reynolds number based on the inlet hydraulic diameter and average velocity was 400.

3.3.3 Test Fluid

To match the density of the particles, a test solution (90% water and 10% glycerine) with an approximate density of 1024 kg/m^3 was prepared. Pliolite particles were tested in this solution and found to follow the flow quite accurately. The liquid was, however,

nebulous and could not be imaged unless a more powerful light source was used. Hence, this was not used as the test fluid. It was found that when de-ionized distilled water was used, the particles responded well and the liquid was sufficiently clear to be imaged. Hence it was selected as the test fluid.

3.4 Calibration Target

In this work, a calibration target was designed and used in conjunction with a tri-split lens system. It consisted of two parallel square plates, which were connected to each other by means of bars placed at the four corners of the structure. Within this framework, a set of wires was positioned between the top and bottom plates (Figure 3.8). Fifty five beads (2 mm in diameter) were strung on the wires and fixed at pre-determined locations, in such a way that they were visible in all of the three views. The locations of the beads were chosen in such a way that they covered almost the entire test volume. The distances between the centres of the beads were accurately measured by means of a vernier calliper (resolution of 0.01 mm). The beads were painted flat white to reduce any unwanted reflection from their surfaces.

CHAPTER IV Methodology

The development of the PIV system consisted of a recording stage and a processing stage. The objective of the recording stage was to log the 3-D co-ordinate positions of the particles in the flow field at various times. In the processing stage, the particle image displacement between two time frames was obtained by processing the information obtained in the recording stage. These steps are discussed in detail in the following sections.

4.1 Recording

The recording process was carried out in two steps: calibration and measurement. Camera calibration was performed to establish a relationship between the image co-ordinate system and the world co-ordinate system. The calibration coefficients for all the three views were determined using both linear and non-linear schemes. A direct linear

transformation was used to obtain an overdetermined set of equations, which were solved to obtain the calibration coefficients. Lens distortion was incorporated into the calibration algorithm to fine tune these coefficients. The next step in the recording process was to use these calibration coefficients to determine the 3-D co-ordinate positions of the particles in the flow field. This involves the pre-processing of the digitized image to enhance the important features. Next, the particle images were matched in orthogonal views by making use of the stereo views to determine their 3-D position information. These steps are discussed in detail in the following sections.

4.1.1 Calibration

Camera calibration is the process of determining the camera's extrinsic and intrinsic parameters by establishing a relationship between the 3-D world co-ordinates and their two-dimensional image co-ordinates. Extrinsic parameters are the 3-D position and orientation of the camera frame relative to a world co-ordinate system. Intrinsic parameters are the camera's geometric and optical characteristics.

The calibration procedure adopted for each view is similar to the one described by Gonzalez and Wintz (1987) and Sid-Ahmed and Boraie (1990). It requires no prior knowledge of the focal length, position and angular orientation of the camera. A schematic diagram of the imaging system is shown in Figure 4.1. The reference co-ordinate system (X,Y,Z) has its origin located at O and is the same for all the three views. Consider a known target point P = (X,Y,Z) in the world co-ordinate system and its homogeneous counterpart expressed as P = (X,Y,Z,w). Let the position of the point P in the imaging

plane of view 1 be given by (x', y'), measured relative to the centre of the plane. The basic procedure is to bring the camera and world co-ordinate into alignment by applying a set of transformations (see Appendix B). Similar procedures were carried out for views 2 and 3.

4.1.1.1 Linear Scheme

The 3-D transformation matrix relating the point P to the image co-ordinates is given by:

$$\begin{bmatrix} x'w_1 \\ y'w_1 \\ w_1 \end{bmatrix} = \begin{bmatrix} a_1 & a_2 & a_3 & a_4 \\ a_5 & a_6 & a_7 & a_8 \\ a_9 & a_{10} & a_{11} & a_{12} \end{bmatrix} \begin{bmatrix} X \\ Y \\ Z \\ 1 \end{bmatrix} \tag{4.1}$$

where w_i is non-zero and is dependent on the transformation. The parameter a_{12}, which represents the scaling factor between the world and the imaging co-ordinate system, was assigned a value of 1 without any loss of generality. By eliminating w_i in these equations, they were rearranged to yield

$$\begin{bmatrix} X & Y & Z & 1 & 0 & 0 & 0 & 0 & -x'X & -x'Y & -x'Z \\ 0 & 0 & 0 & 0 & X & Y & Z & 1 & -y'X & -y'Y & -y'Z \end{bmatrix} [a] = \begin{bmatrix} x' \\ y' \end{bmatrix} \tag{4.2}$$

where $a = [a_1, a_2, \ldots\ldots, a_{11}]^T$.

The unknown calibration coefficients were determined by considering at least 6 world points with known co-ordinates (X,Y,Z) relative to any desired axes, and their

corresponding positions on the imaging plane (x'_j, y'_j), where j = 1..6. It is a common practice to consider more than 6 points in the calibration procedure, so that the effects of small measurement errors are minimized, and to reduce lens distortion effects [Gonzalez and Wintz, 1987]. Substituting these values into equation (4.2), an overdetermined set of equations of the form $Ca = B$ were formed. A least squares fit leads to $C^tCa = C^tB$, which were solved by Crout's method [Press *et al.*, 1992].

4.1.1.2 Non-Linear Scheme

In order to improve the accuracy of the calibration procedure, a correction for lens distortion must be incorporated into the equations. Generally, lens distortion is defined as the failure of a lens to image a straight line in object space as a straight line in image space, and is characterized by two distinct components: radial and tangential [Sid-Ahmed and Boraie, 1990]. The commonly used model for correcting lens distortion was given by Brown [1971]

$$x'_l = x' + \Delta x \tag{4.3a}$$

$$y'_l = y' + \Delta y \tag{4.3b}$$

Δx and Δy are the errors to be added to x' and y' respectively, to account for both types of distortion.

$$\Delta x = x'(k_1 r^2 + k_2 r^4 + k_3 r^6) + p_1(r^2 + (2x')^2) + 2p_2 x'y' \tag{4.4a}$$

$$\Delta y = y'(k_1 r^2 + k_2 r^4 + k_3 r^6) + 2p_1 x'y' + p_2(r^2 + (2y')^2) \tag{4.4b}$$

where $r = (x'^2 + y'^2)^{0.5}$ is the radius from the centre of the image plane to the image point. The constants k_1, k_2 and k_3 represent the radial distortion and p_1 and p_2 denote the

tangential distortion. These constants, which are determined from calibration, are represented by a_{13} , a_{14} , a_{15}, a_{16} and a_{17}. To compensate for the effects of digitization and storage, especially the unknown difference between the pixel rate of the CCD cameras and the clock rate of the frame grabber and line jitter, an additional affine transformation was performed (Maas *et al.*, 1993).

$$x'_c = a_{18}\, x'_l \tag{4.5a}$$

$$y'_c = a_{19}\, y'_l \tag{4.5b}$$

The transformation matrix of equation (4.1) can be rewritten by substituting (x'_c , y'_c) for (x' , y'), where x'_c and y'_c are the corrected co-ordinates of the imaging point x' and y'.

$$\begin{bmatrix} x'_c w \\ y'_c w \\ w \end{bmatrix} = \begin{bmatrix} a_1 & a_2 & a_3 & a_4 \\ a_5 & a_6 & a_7 & a_8 \\ a_9 & a_{10} & a_{11} & 1 \end{bmatrix} \begin{bmatrix} X \\ Y \\ Z \\ 1 \end{bmatrix} \tag{4.6}$$

By substituting equations (4.3), (4.4) and (4.5) into equation (4.6), the following two equations were obtained:

$$f_1(A) = a_{18}\{[x'_c(1+a_{13}r^2 + a_{14}r^4 + a_{15}r^6) + a_{16}(r^2 + (2x'_c)^2) + a_{17}(2x'y')] * [a_9 X + a_{10} Y + a_{11} Z + 1] - [a_1 X + a_2 Y + a_3 Z + a_4]\} = 0 \tag{4.7a}$$

$$f_2(A) = a_{19}\{[y'_c(1+a_{13}r^2 + a_{14}r^4 + a_{15}r^6) + a_{16}(2x'_c y'_c) + a_{17}(r^2 + (2y'_c)^2)] * [a_9 X + a_{10} Y + a_{11} Z + 1] - [a_5 X + a_6 Y + a_7 Z + a_8]\} = 0 \tag{4.7b}$$

where A is a vector of unknown calibration coefficients given by $(a_1, a_2 \ldots\ldots, a_{19})^t$.

Altogether there are 18 parameters modelling the geometry of each view: 11 for exterior and interior orientation, 5 for lens distortion and 2 for electronic influences. An overdetermined set of non-linear equations was formed by considering at least 9 points with known (X,Y,Z) and (x', y') values. The Marquardt method as described in Marquardt(1963) was used to solve these non-linear equations using a least square fit. In this method, the first derivatives of $f_1(A)$ and $f_2(A)$ are needed as follows:

$$\begin{bmatrix} \frac{\partial f_1(A)}{\partial a_1} & \frac{\partial f_1(A)}{\partial a_2} & \cdots & \frac{\partial f_1(A)}{\partial a_{19}} \\ \frac{\partial f_2(A)}{\partial a_1} & \frac{\partial f_2(A)}{\partial a_2} & \cdots & \frac{\partial f_2(A)}{\partial a_{19}} \end{bmatrix} \tag{4.8}$$

A D-matrix was formed by substituting the set of measured values of (X,Y,Z) and (x', y') in equation (4.8). A vector f was defined by substituting the values of (X, Y, Z) and (x', y') in

$$\begin{bmatrix} f_1(A^{(n)}) \\ f_2(A^{(n)}) \end{bmatrix} \tag{4.9}$$

where n is the iteration number. From this substitution, a set of linear equations was obtained in the form given by:

$$(D^T D + \lambda I)\Delta A^{(n)} = -D^T f \tag{4.10}$$

The vector ΔA in this equation is defined by

$$\Delta A = (\Delta A_1, \Delta A_2, ..., \Delta A_{19}) \tag{4.11}$$

and

$$\Delta A^{(n)} = A^{(n+1)} - A^{(n)} \tag{4.12}$$

where $A^{(0)}$ is an initial guess of the calibration coefficients. The initial guesses for $a_1^{(0)}$ to $a_{11}^{(0)}$ were obtained from the solution of the linear equations, and $a_{13}^{(0)}$ to $a_{19}^{(0)}$ are set to zero.

The parameter λ was initially selected as 0.01 and modified in further iterations to ensure minimization of error criterion

$$\psi(n) = \Sigma(f_1^2(A^{(n)}) + f_2^2(A^{(n)})) \tag{4.13}$$

Convergence was obtained when the test

$$\frac{\left|\Delta A_j^{(n)}\right|}{10^{-3} + \left|A_j^{(n)}\right|} \leq 10^{-3} \tag{4.14}$$

holds true for j from 1 to 19.

4.1.1.3 Procedure

The calibration target was placed inside the test section filled with the test fluid (water) and was imaged in all the three views. The entire system was so arranged that the orthogonal images were approximately at the same vertical (y) location. After digitization, the first step was to separate the beads from the dark background by using a thresholding algorithm. The threshold level was selected by performing an analysis of the image's histogram. The value of each pixel was compared with the threshold level, and a new value (0 or 255) was assigned depending on its original value. The second step was to calculate the centroid of each bead in the binary image by using an intensity weighted algorithm. All non-zero pixels were assigned equal weight and the background pixels were ignored. The particle image's centre of mass was calculated by interpreting each pixel's numeric value as its mass.

The image co-ordinates obtained from the frame buffer (in terms of row and column numbers) were mapped onto the image sensor co-ordinates (x_s , y_s) in mm by the following expressions:

$$x_s = (x_f * \frac{N_s}{N_f} - C_x) * px * F_x^{-1} \qquad (4.15a)$$

$$y_s = (y_f - C_y) * py \qquad (4.15b)$$

(x_f, y_f) = Co-ordinates of the point as seen in the frame buffer

(x_s, y_s) = Corresponding co-ordinates in the sensor, measured from the centre of the sensor

(px, py) = Pixel size in the horizontal and vertical directions

(C_x, C_y) = Centre of the image frame co-ordinates

(N_s, N_f) = Number of pixels along the horizontal direction of the sensor and frame buffer

F_x = Uncertainty image scale factor [Lenz and Tsai, 1987]

Pixel sizes (px, py) in the horizontal and vertical directions were calculated from the camera sensor dimensions and the frame buffer size. The camera used in this work has a resolution of 768 (H) x 493 (V) pixels and its cell size is 11.0 (H) x 13.0 (V) μm. The frame grabber can digitize the image into 752 (H) x 480 (V) pixels. The pixel sizes can be calculated as follows:

px = 0.011*768/752 = 0.0112 mm

py = 0.013*493/480 = 0.01335 mm

In this work, the image centre for each view was assumed to be at the geometric centre. If a timing difference existed in the scanning hardware, this assumption will not be valid. This could lead to a black or white band that will appear along the image border and the image centre has to be adjusted to correct this error. The uncertainty in the horizontal scale factor was due to the imperfect match between the computer image acquisition

hardware and the camera hardware. Since the practical value of F_x is close to 1, in the present study it was assumed to be equal to 1. The calibration coefficients for each view were determined separately and a typical set of values is given in Table 4.1.

4.1.2 Measurement

After the calibration, the system was locked in place for recording particle images. The calibration coefficients obtained in the previous section were used to determine the X,Y,Z locations of the particles. This section describes the various steps involved in the measurement of 3-D particle locations in the flow field.

4.1.2.1 Image Enhancement

Figure 4.2 shows a photograph of the digitized image, which is an 8-bit grey level image consisting of the flow tracers and the background. In an optimal situation, the pixels from the background and the particles form well separated peaks in the intensity distribution, with a trough between them where the probability function is almost zero. The threshold value, which lies within that low probability region, could be identified quite accurately. The intensity distribution of most images studied in this work did not reflect the optimal situation. In most cases, the histogram consisted of a pronounced peak in the dark section of the spectrum which gradually decreased into a broad, low distribution at the bright end. This can be attributed to the brightness variation of both background and particle pixels in different areas of the image.

The edges of particles gave relatively sharp discontinuities in the intensity level as compared to the background. This was used to enhance the particle images in the following way. Let u_1 , u_2 ,....., u_9 represent the coefficients of the 3 x 3 mask shown in Figure 4.3 (a). Let x_1 , x_2 ,...., x_9 represent the greylevels of the pixels under the mask (Figure 4.3 (b)), when the mask is in a arbitrary position in the image. The coefficients and their corresponding grey levels can be expressed as column vectors:

$$u = \begin{bmatrix} u_1 \\ u_2 \\ . \\ . \\ . \\ u_9 \end{bmatrix} \qquad x = \begin{bmatrix} x_1 \\ x_2 \\ . \\ . \\ . \\ x_9 \end{bmatrix} \tag{4.16}$$

A Laplacian operator was used to perform the image sharpening (Gonzalez and Wintz, 1987). It is a second order derivative defined as

$$L[f(x,y)] = \frac{\partial^2 f}{\partial x^2} + \frac{\partial^2 f}{\partial y^2} \tag{4.17}$$

With reference to Figure 4.3 (b) , the digital Laplacian at point (x,y) with grey level x_5 can be defined as

$$L[f(x,y)] = x_2 + x_4 + x_6 + x_8 - 4x_5 \tag{4.18}$$

This operation was implemented by convolving the mask shown in Figure 4.3 (c) with an image $f(x,y)$. The Laplacian can be expressed in vector form:

$$L[f(x,y)] = u'x \tag{4.19}$$

where u' is the vector transposition of u. The Laplacian replaces each pixel with the result of the convolution. This enhanced the edges by subtracting a blurred image from the original image. The resulting image appeared sharper and more well defined.

The resulting 8-bit grey level image was converted into a binary image by using a thresholding algorithm. The use of the Laplacian operator deepened the valley between the histogram peaks, thus facilitating the selection of a threshold level (Gonzalez and Wintz, 1987). Pixels with value below the threshold level were set to 0 (black) and those with value above the threshold level were set to 255 (white). This resulted in a binary image with the particle images appearing white over a dark background (Figure 4.4). The threshold selected for the first frame in a sequence was applied to all the remaining images without re-adjustment.

4.1.2.2 Location of Particle Images

An algorithm was implemented to identify particle images in the thresholded image field. A particle image was defined as a blob, a blob being a group of pixels with values equal to or greater than the defined threshold level which are either in direct contact with one another or indirect contact with one another through other pixels. The starting point was located by scanning the image along each row until a pixel with value higher than the threshold was found. Except for a few isolated pixels, which were usually eliminated, at least one neighbour of the current position was identified as a particle pixel. Starting from the current position, all the particle pixels were connected to form a blob. Once the blob was identified, the blob statistics (width, height and centroid) were determined and stored

in a file. The pixel values on and inside of the blob were then set to 0 so that they would not be reprocessed. Scanning along rows resumed until the next blob was found or the whole image had been examined. Since the particle images in this study had a typical size, it was possible to include a procedure to discard the blobs whose width exceeded the given minimum, thus removing extraneous features that might be present in the given field of view.

The centroid of each blob in the binary image was calculated using an intensity weighted algorithm, in which all non-zero pixels were assigned equal weight and the background pixels were ignored. The image's centre of mass was calculated by interpreting each pixel's numeric value as its mass.

Despite careful specification of the threshold parameters, some particularly low quality images still lead to faulty location of the centroids. In such circumstances (about 5%), manual adjustments were performed. Most image processing functions that were available were region oriented, that is, they operated on all the blobs in an interactively defined area. These included deletion of unwanted blobs and averaging of selected blobs into a single one. The latter operation was often effective when a feature of interest was split by the thresholding process into similarly sized fragments. For images of reasonable quality, manual editing was not necessary.

4.1.2.3 Matching

The reconstruction of the spatial position of a point from its location in each distinct view was done in two stages. In the first stage, measurements taken separately in the

stereoscopic views were correlated using a matching routine. The second stage involved the matching of orthogonal pairs. This was even more crucial than stereo matching because orthogonal images appeared widely different from each other making it difficult to match them physically.

(*i*) Stereo Matching

Once the centres of particle images had been located in the stereo views, they were correlated to give the spatial position of the particles. The locations in stereo images that correspond to the same point in space will be referred to as a stereo pair. Although the images appeared similar to each other, it was very difficult to use factors such as similarity in shape, size and the brightness of particle images to identify the stereo pair. The general procedure used for determining the correspondence between points in stereo views is summarized below:

(a) Determination of the probable position

For a given point in view 1 of Figure 4.1, its probable position in view 2 was determined using linear least square coefficients. A calibration target with 55 beads was considered and the locations of these points in the two views were noted. The relationship between the location of a given point in view 1 (x', y') and its corresponding location in view 2 (x'', y'') was assumed to be linear and given by the following equations:

$$l_1 x' + l_2 y' + l_3 = x'' \tag{4.20a}$$

$$l_4 x' + l_5 y' + l_6 = y'' \tag{4.20b}$$

The locations of the calibration points were substituted in the equation (4.20), resulting in 55 equations with three unknowns. Solving this overdetermined set of equations in the least square sense, the coefficients l_1 , l_2 and l_3 were determined. Using the same procedure, the coefficients l_4 , l_5 and l_6 were determined. Substitution of the co-ordinates of a given point (x', y') in view 1 into equations (4.20 a and b), its probable position in view 2 (x_p'', y_p'') was determined using the linear least square coefficients.

(b) Identification of the search neighbourhood

The probable position in view 2 just determined was then compared to every actual point in its neighbourhood which was defined by the epipolar method as described below. The selection of a search neighbourhood in the second view for a given point in view 1 reduces the possibility of finding false matches. For any optical system, there is a specific depth of field within which the object must be located for accurate measurement. In a given application, this depth of field is assumed constant and is given by Z_c and Z_f (see Figure 4.5). Z_c is the closest allowable distance from the object to the optical system and Z_f is the farthest distance the object can be located from the optical system and still be in focus.

Once the system has been calibrated, a given point (x', y') on the imaging plane of view 1 is related to the world co-ordinates by the following equations:

$$\begin{bmatrix} (a_4 - x') \\ (a_8 - y') \end{bmatrix} = \begin{bmatrix} (a_9x' - a_1) & (a_{10}x' - a_2) & (a_{11}x' - a_3) \\ (a_9y' - a_5) & (a_{10}y' - a_6) & (a_{11}y' - a_7) \end{bmatrix} \begin{bmatrix} X \\ Y \\ Z \end{bmatrix} \qquad (4.21)$$

Equation (4.21) represents an underdetermined set of equations (with 2 equations and 3 unknowns X, Y, Z).

Since a prior knowledge of depth of field was assumed, the values for Z_c and Z_f were known. Substituting these values in equation (4.21), (X_c , Y_c) and (X_f , Y_f) were obtained. For a point in 3-D space to have a projected co-ordinate (x', y') on the two-dimensional image plane and to satisfy equation (4.21), the point must lie on line 1 (the line joining the two points (X_c , Y_c , Z_c) and (X_f , Y_f , Z_f)), assuming negligible lens distortion. Once this line is defined, it can be related to the second view by the following equations [Sid-Ahmed and Boraie, 1990].

$$x'' = \frac{b_1X+b_2Y+b_3Z+b_4}{b_9X+b_{10}Y+b_{11}Z+1} \qquad (4.22a)$$

$$y'' = \frac{b_5X+b_6Y+b_7Z+b_8}{b_9X+b_{10}Y+b_{11}Z+1} \qquad (4.22b)$$

Equation (4.22) must be solved twice; once by substituting (X_c , Y_c , Z_c) to obtain (x''_c , y''_c) and a second time by substituting (X_f , Y_f , Z_f) to obtain (x''_f , y''_f). Line 2 (the line joining (x''_c , y''_c) and (x''_f , y''_f)) is the two-dimensional projection of line 1 on the image plane of view 2, and is known as the epipolar line. Since the point with projected co-ordinate (x', y') on view 1 plane lies on line 1, then its projection on view 2 plane must lie on the line 2. Thus line 2 defines the search neighbourhood for the point corresponding to (x', y').

(c) Practical considerations

For a given point in view 1, its actual position in view 2 was found by comparing its probable position with every point in its neighbourhood (identified by the epipolar method) and selecting the match which gave the closest agreement. If the probable position did not lie in the search neighbourhood, the point was discarded. If a match was found, the resulting stereo pair was set aside for position determination. If not, the point was excluded from consideration. As a result, all points in one view were either matched or eliminated for lack of suitable match.

In a practical situation, the calculated probable position did not exactly coincide with the actual position due to errors in measurement. A small tolerance, hence, was allowed and pairs beyond a reasonable limit were excluded. If for a given point in one view there were several feasible matches in the other view, the match which gave the closest agreement was selected. If a selected point was already assigned, it was re-assigned to the new point if the resulting pair gave a better match than the previous one. The process of stereo matching was thus aimed at creating as many disjoint pairs as possible, while keeping discrepancies to a minimum.

(ii) Orthogonal Matching

The general procedure used for determining the correspondence between points in the orthogonal views is given below.

For a given point in view 1 (Figure 4.1), its probable location in view 3 was determined using the (X, Y, Z) values obtained from the stereo views in conjunction with the calibration coefficients $\{c's\}$ from the orthogonal view. The equations for obtaining the probable location (x_p''', y_p''') are given below:

$$x_p''' = \frac{c_1X+c_2Y+c_3Z+c_4}{c_9X+c_{10}Y+c_{11}Z+1} \tag{4.23a}$$

$$y_p''' = \frac{c_5X+c_6Y+c_7Z+c_8}{c_9X+c_{10}Y+c_{11}Z+1} \tag{4.23b}$$

The point (x_p''', y_p''') was compared with every actual point in its neighbourhood and the closest match was selected as in stereo matching. The calibration was done in such a way that the vertical locations of a given point in the orthogonal views (y' and y''') lie approximately on the same horizontal line To facilitate the selection of a match, this correspondence was incorporated into the matching routine. As a result, the number of points needed for comparison was minimized. By allowing a narrow tolerance limit, only pairs within a reasonable limit were considered. Thus the orthogonal pairs were identified.

(*iii*) Check

The accuracy of the matching routines was tested using the calibration points, whose locations in all three views were known. The positional information obtained from the stereo and orthogonal matching was found to be in perfect agreement with the actual values. To further check the validity of these routines, an experiment was carried out with a few particles in the flow field. The stereo and orthogonal pairs corresponding to these

particles were determined both by visual observation and the matching routine. These two sets of values were found to be in agreement.

4.1.2.4 Position Determination

Once all the three views were calibrated, equation (4.1) was rearranged to express X, Y, Z in terms of the imaging co-ordinates (x', y')

$$\begin{bmatrix} (a_1 - a_9 x_c') & (a_2 - a_{10} x_c') & (a_3 - a_{11} x_c') \\ (a_5 - a_9 y_c') & (a_6 - a_{10} y_c') & (a_7 - a_{11} y_c') \end{bmatrix} \begin{bmatrix} X \\ Y \\ Z \end{bmatrix} = \begin{bmatrix} x_c' - a_4 \\ y_c' - a_8 \end{bmatrix} \qquad (4.24)$$

For a point on the target, the imaging co-ordinates (x', y') on the camera plane were measured and substituted in the above two equations yielding an underdetermined set of equations (two equations and three unknowns). In order to complete the above set of equations, a second view was required.

$$\begin{bmatrix} (b_1 - b_9 x_c'') & (b_2 - b_{10} x_c'') & (b_3 - b_{11} x_c'') \\ (b_5 - b_9 y_c'') & (b_6 - b_{10} y_c'') & (b_7 - b_{11} y_c'') \end{bmatrix} \begin{bmatrix} X \\ Y \\ Z \end{bmatrix} = \begin{bmatrix} x_c'' - b_4 \\ y_c'' - b_8 \end{bmatrix} \qquad (4.25)$$

These four equations represent an overdetermined set of equations which were solved in the least square sense. Hence the location (X, Y, Z) of some unknown point was obtained by using the imaging points (x', y') and (x'', y'').

The 3-D co-ordinates of the target point were determined more accurately by using the orthogonal views. Equations which represent the orthogonal views were combined to form an overdetermined set of equations as shown in equation (4.26). These equations were solved in the least square sense to obtain the (X, Y, Z) coordinates.

$$\begin{bmatrix} (a_1 - a_9 x_c') & (a_2 - a_{10} x_c') & (a_3 - a_{11} x_c') \\ (a_5 - a_9 y_c') & (a_6 - a_{10} y_c') & (a_7 - a_{11} y_c') \\ (c_1 - c_9 x_c''') & (c_2 - c_{10} x_c''') & (c_3 - c_{11} x_c''') \\ (c_5 - c_9 y_c''') & (c_6 - c_{10} y_c''') & (c_7 - c_{11} y_c''') \end{bmatrix} \begin{bmatrix} X \\ Y \\ Z \end{bmatrix} = \begin{bmatrix} x_c' - a_4 \\ y_c' - a_8 \\ x_c''' - c_4 \\ y_c''' - c_8 \end{bmatrix} \qquad (4.26)$$

The 3-D data sets, containing the particle image locations, were obtained by repeatedly solving equation (4.26) for each particle. Several such data sets were obtained for various time instants. This information was then processed to obtain the 3-D displacements of the particles. This step will be considered in the next section.

4.2 Processing

The data sets containing the 3-D particle locations, obtained from the recording stage, were processed to obtain the 3-D displacements. A cross-correlation method was implemented for this purpose. The steps involved in the processing stage are described below

4.2.1 The Correlation Method

The correlation method can be used to statistically determine the most probable displacement of a group of particles in a sampled area. Two sequential images are

considered as spatial signals, the initial one represents the input signal and the second image, that contains the shifted particles, represents the output signal. Willert and Gharib (1991) modeled the relation between the two sequential images using a linear system. If the input and output signals are given, the only unknown is the transfer function or the shift function. The correlation method is used to find this shift function, which will provide the displacement information between two sequential images. The cross-correlation function represents the probability distribution of all possible displacements of the particles in the sampled area. The maximum of the cross-correlation function then represents the most probable displacement of the particles between the sampled images. The magnitude and direction of the displacement can be determined by locating the maximum value of the cross-correlation function.

In this work, the two-dimensional cross-correlation function has been extended to the 3-D case using the existing data sets. In the data set, each particle was represented by a voxel (i.e., a volume element) rather than by a pixel. The fluid motion in a small sampled volume, 20 x 20 x 20 mm^3, over a small time interval was modeled using a linear system. For two sequential data sets, the first set was treated as the input signal and the second as the output signal. Neglecting the noise effects, the linear system is expressed in mathematical form as

$$g(m,n,o) = [f(m,n,o) * s(m,n,o)] \tag{4.27}$$

where $f(m,n,o)$ represents the brightness of the input signal at voxel location (m,n,o), $g(m,n,o)$ denotes the brightness of the corresponding output signal and $s(m,n,o)$ represents the spatial shift function. The symbol * denotes the spatial convolution of the two

functions $f(m,n,o)$ and $s(m,n,o)$. This expression is represented schematically in Figure 4.6. Equation (4.27) can be expressed in the discrete form as:

$$g(m,n,o) = \left[\sum_{c=-\infty}^{\infty} \sum_{d=-\infty}^{\infty} \sum_{e=-\infty}^{\infty} s(c-m, d-n, e-o) f(c,d,e) \right] \qquad (4.28)$$

The shift function $s(m,n,o)$ is the Dirac delta function, $\delta(m-i,n-j,o-k)$, placed at i, j, k units from the origin. This displacement corresponds directly to the average displacement of the particles in the sampled region.

The spatial cross-correlation technique is used to determine the shift function $s(m,n,o)$. Mathematically, the cross-correlation function $\phi_{fg}(m,n,o)$ can be expressed as:

$$\phi_{fg}(m,n,o) = \frac{\sum_{c=-\infty}^{\infty} \sum_{d=-\infty}^{\infty} \sum_{e=-\infty}^{\infty} f(c,d,e) g(c+m, d+n, e+o)}{\sum_{c=-\infty}^{\infty} \sum_{d=-\infty}^{\infty} \sum_{e=-\infty}^{\infty} f(c,d,e) \sum_{c=-\infty}^{\infty} \sum_{d=-\infty}^{\infty} \sum_{e=-\infty}^{\infty} g(c,d,e)} \qquad (4.29)$$

When many particle images match up with their corresponding spatially shifted partners, a high cross-correlation value of 1 is observed. When individual particle images match up with other particle images, small correlation peaks may be observed. The best match of particle images between the functions $f(m,n,o)$ and $g(m,n,o)$ is represented by the highest correlation peak.

The maximum of the cross-correlation peak coincides with the displacement delta function $(m-i, n-j, o-k)$. To illustrate this, the discrete correlation function is expressed as an expectation function [Chen and Chen, 1991]

$$\Phi_{fg}(m,n,o) = E[f(m,n,o), g(m,n,o)] \qquad (4.30)$$

$$\Phi_{fg}(m,n,o) = E[f(m,n,o), f(m,n,o) * s(m,n,o)] \qquad (4.31)$$

$$\Phi_{fg}(m,n,o) = \Phi_{ff}(m,n,o) * s(m,n,o) \tag{4.32}$$

where $\phi_{ff}(m,n,o)$ is the autocorrelation function of the input function $f(m,n,o)$. Since the input function $f(m,n,o)$ correlates with itself in $\phi_{ff}(m,n,o)$, the maximum of the autocorrelation function is always located at the centre of the cross-correlation domain. From equation (4.32), $\phi_{fg}(m,n,o)$ is obtained by performing convolution on the autocorrelation function $\phi_{ff}(m,n,o)$ with shift function $s(m,n,o)$. This operation moves the autocorrelation peak away from the origin by the average spatial displacement of particles in the sampled region. The values of $\phi_{fg}(m,n,o)$ in the sampled volume of two sequential data sets are calculated. Once the maximum value of $\phi_{fg}(m,n,o)$ within the sub-cube is identified, the shift function is determined by measuring the distance between the origin and the location of the maximum value $\phi_{fg}(m,n,o)$.

4.2.2 Computational Implementation

The recording procedure resulted in several data sets of 3-D particle locations obtained at various time instants. Thus each particle in the cubical test section was associated with three spatial co-ordinates X, Y and Z. The cube was divided into 125 sub-cubes over which it was assumed that the velocity remained constant. These sub-cubes spanned the entire test volume. Each particle in the cube was assigned to a particular sub-cube based on its 3-D position relative to the test section. Each sub-cube was then gridded into 128 x 128 x 128 voxels (i.e., volume elements) for fast Fourier transform (FFT) purposes. The large number of computations needed to compute the 3-D FFT's placed a practical restriction on the number of grid elements. Thus each particle within a

sub-cube was associated with three voxel coordinates, which signified its position relative to the sub-cube. In each sub-cube, a value of 1 was assigned to every voxel location where a particle was present and all the remaining locations were assigned a value of 0. Thus each set of voxel coordinates corresponded to a 1 or a 0 indicating the presence or absence of a particle respectively.

Two data sets taken for the same sub-cube at different time frames were used for the cross-correlation. A schematic diagram of the correlation technique implementation is shown in Figure 4.7. By using a 3-D FFT algorithm, each sub-cube was transformed into the Fourier domain. The 3-D FFT algorithm has been developed by using the separability property of the Fourier transforms. This involves a successive application of three 1-D FFT transforms, along the row, column and height of the data set. More details are given in Appendix C.

In the Fourier domain, the operation of cross-correlation is reduced to a complex conjugate multiplication of each corresponding pair of Fourier coefficients. The resulting set of coefficients was then transformed into the spatial domain by using an inverse FFT algorithm to yield the cross-correlation function ϕ_{fg}. This resulted in a large spike displaced from the origin corresponding to the spatial shift of the particles from one time to the next. The location of this peak was determined by finding the highest value in the 3-D array of correlation values. The 3-D displacement, thus obtained, was used in conjunction with the time interval between frames to determine velocity information in that sub-cube. To obtain velocity values throughout the entire field, this procedure was repeated on the other sub-cubes within the test volume. In this work, entire test volume for

visualization was 100 mm x 100 mm x 100 mm. The volume of each sub-cube was 20 mm x 20 mm x 20 mm, thus yielding a total of 125 velocity vectors.

4.3 Factors Affecting System Performance

There are a number of factors that affect the performance of the measurement system.

4.3.1 Multimedia Geometry

The effect of a ray being twice broken due to different refractive indices in the optical path through water, glass and air constitutes a multimedia geometry. The multimedia environment causes some problems which were not included in the calibration scheme but do influence the accuracy of results. Some of the effects include:

- An apparent change in the object position
- A visual change in the image size
- Some increase in general optical aberrations

An object photographed underwater would appear closer than in the air, as the angle of convergence of the lens is reduced. As a result, they appear larger or magnified. By performing the calibration with the target under water, these factors are automatically incorporated into the calibration equations.

The aberrations, which lead to a degradation of the image quality, are present in the optical system if the lenses are corrected for use in air. The dispersion in water is much larger than in air leading to colour seams at the edges of the image objects, which will appear as blur in black and white images. Diffusion and absorption in water cause an extinction of the light and reduce the image contrast. Distortion affects the shape of the image. Pin cushion distortion results when the magnification of the outer portion of the image is greater than that of the central portion, and barrel distortion results when it is less. These effects are partly compensated by using the additional calibration parameters and calibrating the system in situ under the optical conditions of the experiment. All these effects cause a degradation of the multimedia image quality and systematic error, leading to larger errors in the particle co-ordinate determination compared with applications in air.

4.3.2 Noise in Camera and Imaging System

The electrical noise in the system includes random noise in the camera and imaging board electronics and drift due to temperature change. The electrical noise is inherent to the camera and the imaging system. The drift due to temperature change can be minimized by stabilizing the system, before making the measurements.

4.3.3 Calibration Scheme

Some of the factors which were not considered in the calibration model include: non-perpendicularity of the optical axis with respect to the image plane, uncertainty in

locating the centre of the image plane and scale variation in the horizontal and vertical directions. A more comprehensive model has to be used to compensate for these factors.

4.3.4 Correlation Algorithm

The grid size used in the correlation algorithm limits the resolution of the displacement measurement. If a smaller grid size is used, the measurement resolution would be improved but the computation time will be increased tremendously and vice versa. So a compromise should be reached to achieve a reasonable accuracy within a reasonable time.

4.4 Summary

The following is a summary of the steps in the methodology with certain comments and observations that were made:

1. A two-stage calibration of the optical system, involving both linear and non-linear schemes, was implemented. This procedure requires no prior knowledge of the focal length, position and angular orientation of the camera. Incorporation of the non-linear scheme improved the results significantly.

2. The use of a Laplacian operator in combination with a threshold algorithm provided sharp and well defined binary images.

3. The probable positions obtained using the linear least square coefficients were found to provide a good starting point for the stereo matching routine.

4. A new matching routine was developed to overcome the problem of matching orthogonal images which appear widely different from each other. The probable position obtained with the routine provided a good starting point for the identification of orthogonal pairs.

5. The stereo and orthogonal matching routines are independent of any geometrical considerations, eliminating the need for precise alignment of the optics.

6. It was observed that implementation of 3-D FFT's to perform the cross-correlation resulted in long computational processing times.

7. The procedure did not require the identification of individual particles in different time frames as required by the tracking scheme.

CHAPTER V Testing and Evaluation

In this chapter, the results of an analysis of the system performance is presented in the first section. The next section includes a brief review of the experimental test run followed by a discussion of the results. A description of numerical simulations of the flow inside the cubical chamber were given in the fourth section. Finally, the results obtained from the experimental investigation are compared with those from the numerical simulations and followed by a summary.

5.1 System Performance

Any strategy for the evaluation of performance of a photogrammetric system must take into account the repeatability of results as well as the absolute accuracy. Digital images are affected by various factors making it difficult to achieve repeatable and highly accurate measurements compared to measurements made using photographs, which have

excellent repeatability. The system performance is evaluated in terms of accuracy, repeatability and bias which are determined as presented below, from a number of measurements of the locations of targets.

5.1.1 Position Measurement

The accuracy, repeatability and bias of the position measurement are presented in the following sections.

5.1.1.1 Accuracy

Accuracy is defined as the degree of conformity between a measured quantity and a recognized standard or specification, which is considered to be the true value of the quantity. It is estimated as a statistical measure of the spatial deviation between the actual object position and those obtained from the photogrammetric system. In this work, the average and the maximum deviation between the actual and the measured value were used to indicate the accuracy. The average deviation is given by:

$$E_X = \frac{1}{N}\sum_{i=1}^{N} |X_a(i) - X_m(i)| \qquad (5.1)$$

where $X_a(i)$ is the actual co-ordinate, $X_m(i)$ is the measured co-ordinate, and N is the number of points considered. Similar definitions apply to E_Y and E_Z. The maximum deviation is the absolute maximum of the differences between the actual and measured values. It is given by:

$$M_X = abs[\max[X_a(i) - X_m(i)]] \qquad \text{for i} = 1,....,N \qquad (5.2)$$

Similar definitions apply for M_Y and M_Z .

The large number of beads on the calibration target made it possible to use some of them as control points (used in calibration) and the remaining as check points. These check points were treated as unknown points and the deviations between the determined co-ordinates and the known co-ordinates gave a good estimate of the system accuracy. The co-ordinates of these check points were obtained using the calibration coefficients determined from the control points.

To test the accuracy of the method under ideal conditions, a calibration was performed with the target in air to avoid the problems associated with a multimedia environment. Both the linear and non-linear schemes were used to describe the intrinsic and extrinsic measurement system parameters. The calibration errors (in terms of average and maximum deviation) for stereo views are presented in Tables 5.1 and 5.2. From Table 5.1, it can be observed that the results obtained by incorporating additional parameters for lens distortion and electronic influences (set B), are more accurate than those obtained without these parameters (set A). The amount of lens distortion is proportional to the distance between the image point and the image centre. It could be as large 2% near the edges of the field of view. The results for orthogonal views are given in Tables 5.3 and 5.4. These results show a considerable improvement (89%) in the accuracy of the Z (depth) values, over those obtained from the stereo views. This can be attributed to the large angle between the optical axes of the two views.

The calibration was repeated with identical equipment and the same field of view

except that the chamber was filled with water. Tables 5.5, 5.6 contain the calibration results for average deviation and maximum deviation for stereo views while Tables 5.7 and 5.8 contain results for orthogonal views. These results show that the accuracy of the hardware system is degraded as a result of the multimedia environment. The additional parameters used to correct for lens distortion and the affine transformation in the case with water were found to be significantly different than those determined for the case in air, although the lenses had not been moved. It is, therefore, crucial that the system calibration be performed under the actual optical conditions of the experiment.

5.1.1.2 Repeatability

Repeatability is of concern to any measurement system. It refers to the ability of the system to indicate a particular value upon repeated measurements of the same quantity. The noise and random effects that propagate through the measurement system determine the repeatability. It can be estimated by

$$P_X = t_{v,P} S_X \tag{5.3}$$

where $t_{v,P}$ is obtained from the Student-t distribution and S_x is the standard deviation given by

$$S_X = \sqrt{\frac{\sum_{i=1}^{N} [(X_m(i) - \bar{X}_m)^2]}{N-1}} \tag{5.4}$$

where $\bar{X}_m = \frac{\sum_{i=1}^{N} X_m(i)}{N}$. Similar definitions apply for P_Y and P_Z.

The repeatability of the photogrammetric system was evaluated by making repeated measurements of the calibration target at different times. This was carried out using the set-up previously described. The centroid co-ordinates of the same calibration point were measured repeatedly (nine different times) and the results are shown in Table 5.9. It can be observed that there is a small variation in the particle image co-ordinates which can be attributed to the noise in the CCD elements and other electrical noises in the digitizer. Table 5.10 presents the results of the measurement precision for 3-D position information.

5.1.1.3 Bias

Bias is defined as the average error in a series of repeated calibration measurements. Calibration against a standard provides the most direct way of measuring bias. It is given by:

$$B_X = [X_a - \bar{X}_m] \tag{5.5}$$

The results are shown in Table 5.10.

5.1.2 Displacement Measurement

The measurement system's ability to indicate displacement was evaluated in the following way. The cubical test section was filled with water and the calibration target was carefully placed inside it. The test section was then positioned on the three-axis translation table. High precision anti-backlash ball screws enable the translation table to move the test

section in all 3 directions. A set of dial gauges was mounted on the table to indicate the actual movement of the target. The photogrammetric system was used to photograph the test section before and after the movement and the 3-D position information was obtained. The cross-correlation algorithm was used to calculate the displacement and the results were then compared with the actual movement determined from the dial gauges. Table 5.11 presents the results of the system accuracy. The calibration error was computed as the maximum devitation between the actual and the calculated movement.

5.2 3-D PIV Experimental Method

The following measures were necessary to prepare the equipment for the collection of velocity data. The lower reservoir (see Figure 3.5) was filled with water, to which the particles were added, and the mixture was stirred well. The pump was turned on and water was pumped to the constant head tank. Once the constant head tank was full, the excess water was returned to the reservoir through the overflow tube. The flow rate was set to approximately the desired value using the regulating valve and the rotameter calibration curve. A quantity of water was collected over a certain period of time and the actual flow rate was calculated. The Reynolds number was then calculated, and if it differed from the desired value (Re = 400), the flow was adjusted and measured again.

The fluid entered the test section at the bottom and exited from the top. The images captured by the camera were digitized and stored in the frame buffer. In the initial test runs, the concentration of particles in the fluid was kept relatively low (about 10-15) to check the accuracy of the matching routines. In later test runs the concentration of

particles in the cubical test volume was increased until there were about 250 - 300 particles in each view.

5.3 3-D PIV Experimental Results

The following observations were made from visual observation of the flow in the test chamber. The fluid behaved like a jet at the chamber inlet, and then began to diffuse as it moved toward the outlet wall (The top surface of the test section on which the outlet is located at one corner). After the inlet jet spread as it hit the outlet wall, some fluid moved diagonally towards the outlet and some recirculated in the chamber. At the outlet, the flow behaved like a sink. The velocity in the centre of the chamber was appreciable, while the flow around the corner regions was quite stagnant or exhibited small, secondary circulation regions. The flow in the chamber at Re = 400 was found to be laminar and steady.

A 3-D velocity vector plot obtained from the experimental investigation is shown in Figure 5.1. The results confirm, in a qualitative sense, the observations made in the initial test run. Figures 5.2 through 5.6 present the profiles of the V component of velocity on the five planes (X = 10, 30, 50, 70, 90) along the lines Y = 10, 50, 90. In Figure 5.2, it can be observed that the profiles at Y = 10 display the strong inlet flow at Z = 70. As the flow reaches the corner located near the Y = 90 plane, the velocity decreases mainly due to the diffusion and divergence of the flow. When the flow reaches Y = 90, the flow reverses near the edges (i.e., at large and small values of Z). In these locations, the largest negative velocity occurs near Y = 50. This may be due to the influence of of the top and bottom

plates near $Y = 90$ and $Y = 10$ respectively. In Figure 5.3, the flow pattern is dominated by the strong inlet flow, except in the farther corner from the inlet (at $Z = 10$) where there is some convergence of flow. As the plane $X = 50$ (figure 5.4) is located halfway between the inlet and outlet, flow is influenced by the entrainment effects induced by the inlet and the sucking effects from the outlet. In Figures 5.5 and 5.6, the effect of the outlet is evident and is indicated by a peak on the left hand side.

The velocity profiles of U on the five projected planes ($X = 10, 30, 50, 70, 90$) along the lines $Y = 10, 50, 90$ are presented in Figures 5.7 through 5.11. The velocity profile at plane $Y = 10$ shows that the flow moves from the lower left-hand corner toward the upper right-hand corner as the inlet fluid is turned and spread out at the lower left-hand corner. It can be observed from Figures 5.9 through 5.11 that the velocity profiles in these planes are strongly influenced by the outlet flow. Figures 5.12 through 5.16 present the velocity profiles of W on the projected planes ($X = 10, 30, 50, 70, 90$) along the lines $Y = 10, 50, 90$. These figures indicate a general trend of relatively strong negative W component of velocity near the upper plate ($Y = 90$), which corresponds to a flow towards the outlet which become more peaked at locations closer to the outlet ($X = 70$ and 90 at $Z = 30$). The figures just presented are difficult to appreciate and interpret. In order to obtain a better understanding of the flow pattern, the symmetrical nature of the flow is investigated as follows.

Consider a horizontal cross-section (X-Z plane) of the test volume as shown in Figure 5.17. The test section has a plane of symmetry (X_1) which is perpendicular to the X-Z plane and passes through $X = 0$, $Z = 100$ and $X = 100$, $Z = 0$ (the diagonal plane cutting

through the inlet and the outlet). Z_1 is the diagonal passing through the points X = 0, Z = 0 and X = 100, Z = 100. It intersects the plane of symmetry X_1 at X_1 = 0 and is perpendicular to it. The planes A1 and A2 are located on either side of X_1 and are equi-distant from it. The planes B1 and B2, C1 and C2, D1 and D2 are similarly located. Based on geometrical symmetry, it can be expected that the corresponding points on the planes A1 and A2 have the same velocity magnitude. Similarly points on the planes B1 and B2, C1 and C2 and D1 and D2 would have the same velocity magnitude.

The plot of position versus the velocity magnitude, along the Z_1 axis, at different values of Y, is shown in figure 5.18. The points along the Z_1 axis form the abcissa and the corresponding velocities form the ordinate. The velocity magnitude $|\underline{V}|$ is calculated as follows:

$$|\underline{V}| = \sqrt{U^2 + V^2 + W^2} \qquad (5.6)$$

where U, V, W are the velocity components in X, Y, Z directions. The plot seems to indicate a reasonable degree of symmetry near the bottom plate (i.e. Y = 10) across the entire range of Z1. At larger values of Y, the symmetry is confined to the central portion of the chamber.

5.4 Numerical Simulation

In this study, FLUENT and STAR-CD were used for numerical simulation of the flow in the cubical chamber. The simulated results were then compared with those

obtained from the present technique. The 3-D incompressible fluid flow considered in this work is governed by the following dimensionless equations:

$$\frac{\partial u}{\partial t}+u\frac{\partial u}{\partial x}+v\frac{\partial u}{\partial y}+w\frac{\partial u}{\partial z} = -\frac{\partial p}{\partial x}+\frac{1}{Re}(\frac{\partial^2 u}{\partial x^2}+\frac{\partial^2 u}{\partial y^2}+\frac{\partial^2 u}{\partial z^2}) \quad (5.7)$$

$$\frac{\partial v}{\partial t}+u\frac{\partial v}{\partial x}+v\frac{\partial v}{\partial y}+w\frac{\partial v}{\partial z} = -\frac{\partial p}{\partial y}+\frac{1}{Re}(\frac{\partial^2 v}{\partial x^2}+\frac{\partial^2 v}{\partial y^2}+\frac{\partial^2 v}{\partial z^2}) \quad (5.8)$$

$$\frac{\partial w}{\partial t}+u\frac{\partial w}{\partial x}+v\frac{\partial w}{\partial y}+w\frac{\partial w}{\partial z} = -\frac{\partial p}{\partial z}+\frac{1}{Re}(\frac{\partial^2 w}{\partial x^2}+\frac{\partial^2 w}{\partial y^2}+\frac{\partial^2 w}{\partial z^2}) \quad (5.9)$$

$$\frac{\partial u}{\partial x}+\frac{\partial v}{\partial y}+\frac{\partial w}{\partial z} = 0 \quad (5.10)$$

where u, v and w are dimensionless velocity components in x, y and z directions respectively. The velocity components are non-dimensionalized with respect to the inlet average velocity U, and the dimensionless pressure p was normalized by ρU^2. Re is the Reynolds number or $\rho UL/\mu$, where L is the characteristic length (inlet height or 2 cm), ρ is the density and μ is the absolute viscosity. The boundary conditions must also be specified. All the velocity components are zero on the walls. The velocity is assumed to be uniform at the inlet with magnitude U. At the outlet, the velocity gradient was set to zero. The solution domain consisted of a 100 x 100 x 100 mm^3 cubical region comprising of the inlet and the outlet (see Figure 3.7).

5.4.1 FLUENT

FLUENT, a general purpose computer program for modelling fluid flow, was used to simulate the flow inside the cubical chamber. With this method, the fundamental equations governing fluid flow are solved by a finite difference numerical procedure. This

procedure involves the division of the domain of interest into a finite number of control volumes or cells. The governing equations are reduced to equivalent finite difference forms to obtain sets of simultaneous algebraic equations. These equations are solved by a semi-implicit iterative scheme, which starts from certain initial conditions and converges to a solution after performing a number of iterations. The iterative procedure is adopted because of the non-linearity and interdependence of the differential equations. The velocity components lie on the negative face of each finite difference cell. All the other dependent variables are calculated and stored at nodal points which the finite difference cells encompass.

FLUENT is a user friendly menu driven package where simulation is done interactively by responding to a series of prompts in a systematic fashion. The physical constants like the viscosity and density of the operating fluid are given as inputs. Since water was used as the working fluid in the experiments, the problem was simulated with the same fluid. In FLUENT, the number of iterations to be carried out are specified as input. The calculations are done in an iterative process until a converged solution is obtained. The residuals for each flow variable give a measure of the degree to which each equation is satisfied throughout the flow field. The effect of different sums of residuals (10^{-3}, 10^{-4} and 10^{-5}) on the results was checked by comparing the velocity values for all the 125 points that were determined from the experimental investigation (see Table 5.17). The maximum and average difference between different sums of residuals were computed. It can be observed that the results of all the runs do not differ significantly from each other. Hence for the present problem, convergence was said to have been achieved if the sum of

the normalized residuals was less than or equal to 1.0E-03 which indicates that all velocity components were determined to within ±0.01 mm/s.

A number of factors, such as, grid size, physical models selected and the geometric approximations determine the accuracy of FLUENT predictions. The effect of grid size on FLUENT predictions was checked for Reynolds number of 400. For this purpose FLUENT solutions were obtained for grid sizes of 12x12x12 and 21x21x21 (see Table 5.18). It can be observed that the results obtained using a 12x12x12 grid size were slightly different than the 21x21x21. Higher grid sizes could not be implemented because of the restrictions on the maximum number of elements that were allowed in the FLUENT software. The simulation results obtained using 21x21x21 grid size were used for comparison with the experimental results.

5.4.2 STAR-CD

STAR-CD is a self contained, fully integrated and user friendly CFD (computational fluid dynamics) code comprised of pre-processing, analysis and post-processing facilities. It consists of two components: the pre- and post-processing module PROSTAR and the analysis module STAR. PROSTAR is an interactive, command and menu-driven code whose function is to provide input data for STAR and to process the output corresponding to this data. The code thus combines pre- and post-processing within a self-contained package. The users interaction with the STAR-CD system is always through PROSTAR. STAR is at present run separately as an independent program following completion of the input data preparation phase. It incorporates a numerical

finite-volume procedure for solving the governing partial differential equations. The procedure employs a general body fitted, non-orthogonal and unstructured mesh system that endows it with considerable geometrical flexibility. STAR-CD solutions were obtained for a grid size of 20x20x20 as it would be easier to compare the results with those of FLUENT. The results obtained from STAR-CD were found to be quite consistent with the predictions of FLUENT (see Appendix D). The % deviations were calculated as follows:

$$\Delta U = \frac{ABS(U_{FLUENT} - U_{STAR\text{-}CD})}{(U_{FLUENT} + U_{STAR\text{-}CD})/2} \tag{5.11}$$

Similar definitions apply for ΔV and ΔW. From the tables in the Appendix, it was observed that the average deviation was approximately 2-3%. The maximum deviation was as high as 15%. It is interesting to note that the maximum difference occurred on the X = 10 plane not far from the location where the largest difference between the experimental and numerical method was found.

5.5 Comparison of Experimental and Numerical Results

The velocity profiles obtained from the experimental investigation were compared with those obtained from the CFD packages, FLUENT and STAR-CD. Table 5.12 presents the percentage difference of the velocity values obtained from the experimental

and the numerical schemes on the projected plane X = 10. The difference is calculated in the following way:

$$\Delta U = \frac{[U_e - \frac{(U_{FLUENT} + U_{STAR\text{-}CD})}{2}]}{U_e} \times 100 \qquad (5.12)$$

where

ΔU is the percentage difference between the U-velocities obtained from the experimental and the numerical schemes.

U_e is the U-velocity obtained from the experiment.

U_{FLUENT} is the U-velocity obtained from FLUENT.

$U_{STAR\text{-}CD}$ is the U-velocity obtained from the STAR-CD.

The % differences for the V and W-velocities are similarly calculated. Tables 5.13 through 5.16 present similar information for the planes X = 30, 50, 70, 90. The following general observations were made from the tables. In general, the experimental results were found to be in agreement with the numerical values. There is an average deviation of 10% (approximately) between the results obtained from the numerical simulation and the experiment. Inherently, there are errors present in the recording and processing schemes. These errors are magnified whenever the velocity values are small. In these cases the deviation was found to reach a maximum of 25%. Among the error sources, the uncertainties associated with the 3-D position measurement and the grid size in the correlation process are significant. An uncertainty analysis is provided in Appendix E.

5.6 Summary

1. The orthogonal photogrammetric method provided a significantly better estimate of the depth co-ordinate as compared to stereogrammetric method.

2. The relatively low resolution of the camera is further reduced by the use of a tri-split lens and this affects the system accuracy. Another factor which affects the performance of the system is the error involved in the calibration scheme.

3. The performance of the 3-D PIV measurement system deteriorated slightly when water was included in the test section as compared to that under ideal conditions (in air).

4. The results obtained from STAR-CD and FLUENT were found to be consistent with each other (see Appendix E). There is an average deviation of 2-3%, with a maximum of 15.1%

5. For velocity measurement, the general trend obtained with the experimental investigation was found to be consistent with the numerical predictions. However, there is a maximum deviation of 25% between the experimental and the numerical velocity values, with an average of approximately 10%.

CHAPTER VI Conclusions and Recommendations

6.1 Contributions

1. A PC-based PIV system for measuring 3-D velocity information using a single camera has been implemented and tested. Based on photogrammetric imaging and correlation methods of processing, this system uniquely combined the advantages of stereo and orthogonal views to determine an accurate location of the particle.

2. A calibration target was designed in such a way that, when used in conjunction with the photogrammetric system, it could be imaged in all the three views. The calibration points were so arranged that the their locations spanned the entire test volume. The same target was also used for developing the particle matching routines.

3. The coefficients for all the three views were determined using a two step calibration scheme. In the first step, a pin-hole camera model was used for linear calibration, where a

transformation matrix was used to represent the relationship between the world and the image co-ordinate systems. Radial and tangential lens distortion was incorporated in the non-linear calibration scheme, where the calibration coefficients determined from the first step were fine tuned for a better fit of the camera transformation.

4. Stereo and orthogonal matching routines were implemented. In stereo matching, the probable positions obtained using the linear least square coefficients were found to provide a good starting point for the matching routine. To overcome the difficulties in matching orthogonal images, a new matching routine was developed. It made use of the 3-D position information obtained from the stereo views to obtain an estimate for identifying the orthogonal pairs. The matching routines are independent of any geometrical considerations and this eliminated the need for precise alignment of the optics.

5. A 3-D cross-correlation algorithm, based on FFT's, was implemented. This algorithm provided an average displacement of a group of particles in a small volume. The accuracy of the method is dependent on the grid sizing, size of the test volume and the number of particles in the sub-cube.

6. The system is simple, robust and built with off-the-shelf components. The use of a single camera simplified the system set-up, control and calculation. It also reduced the cost significantly.

6.2 Conclusions

1. The orthogonal views provided a significantly better estimate of the depth co-ordinate as compared to stereo views.

2. The use of 3-D FFT's to perform the cross-correlation resulted in large computation times. However, the procedure eliminated the need for identifying individual particles in different time frames as required by the tracking scheme.

3. The experimental velocity components were found to be consistent with the numerical predictions with a maximum deviation of 25%.and an average of approximately 10%.

4. The results obtained from STAR-CD and FLUENT were found to be consistent with each other with a maximum deviation of 15%.

5. The non-linear camera model performed better than the linear calibration model.

6. It was found that the system performance in water deteriorated slightly as compared to that under ideal conditions (in air).

7. The experimental error in the velocity measurement was estimated to 9.6%.

6.3 Recommendations

The system can be improved in a number of ways:

1. The resolution of the camera relative to the field of view should be increased by using

three separate high resolution cameras instead of one with the tri-split lens.

2. More complicated camera models incorporating various non-ideal factors should be considered for performing the calibration.

3. Higher intensity light source should be used with the system which would allow shorter exposure times.

4. The density of the fluid and the particle should be matched by increasing the density of the working fluid and reducing the size of the particles. This can be done by mixing glycerine in water. This would also require a more powerful light source.

5. The computing speed should be increased by using a standalone SGI Indigo Workstation or another faster computer.

3. The effect of grid sizes and sub cube size on the accuracy should be investigated.

References

Adamczyk, A. A. and Kimai, L., 1988, "Reconstruction of a 3-D flow field from orthogonal views of seed track video images", Experiments in Fluids, 6, pp. 380-386.

Adrian, R.J., 1986, "Multi-point optical measurements of simultaneous vectors in unsteady flow - A review", International Journal of Heat and Fluid Flow, 7, pp. 127-145.

Agui, J.C. and Jimenez, J., 1987, "On the performance of particle tracking", Journal of Fluid Mechanics, 185, pp. 447-468.

Altman, D., 1994, Personal Communication, North West Research Associates, Seattle, Washington State, USA.

Arroyo, M.P. and Greated, C.A., 1991, "Stereoscopic particle image velocimetry", Measurement Science and Technology, 2, pp. 1181-1186.

Brodkey, R.S., 1986, "Image processing and analysis for turbulence research", Chemical Engineering Education, 20, pp. 202-207.

Brown, D.C., 1971, "Close-range camera calibration", Photogrammetric Engineering, 37, pp. 855-866.

Caffyn, J.E. and Underwood, R.M., 1952, "An improved method for the measurement of velocity profiles in liquids", Nature, 169, pp. 239-240.

Carder, K.L., Steward, R.G. and Betzer, P.R., 1982, "In situ holographic measurements of the sizes and settling rates of oceanic particulates", Journal of Geophysical Research, 87, pp. 5681-5685.

Chang, T.P.K., Wilcox, N.A. and Tatterson, G.B., 1984, "Application of image processing to the analysis of three-dimensional flow fields", Optical Engineering, 23, pp. 283-287.

Chang, T.P.K., Watson, A.T. and Tatterson, G.B., 1985a, "Image processing of tracer particle motions as applied to mixing and turbulent flow - I. The technique", Chemical Engineering Science, 40, pp. 269-275.

Chang, T.P.K., Watson, A.T. and Tatterson, G.B., 1985b, "Image processing of tracer particle motions as applied to mixing and turbulent flow - II. Results and Discussion", Chemical Engineering Science, 40, pp. 277-285.

Chen, L.J. and Chen, C., 1991, "Visualization of three-dimensional flow in a cubic chamber with digital correlation method", Third Triennial International Symposium on Fluid Control, Measurement and Visualization (FLUCOME '91), San Francisco.

Cho, Y.C., 1989, "Digital image velocimetry", Applied Optics, 28, pp. 740-748.

Curry III, T.S., Dowdey, J.E. and Murray, Jr., R.C., 1990, "Christensen's Physics of Diagnostic Radiology", 4th edition, Lea and Febiger, London.

Doi, J. and Miyake, T., 1983, "Three-dimensional flow analysis by on-line particle tracking", Proceedings of Third International Symposium on Flow Visualization, Ann Arbor, Michigan, pp. 14-18.

Elkins III, R.E., Jackman, G.R., Johnson, R.R. and Lindgren, E.R., 1977, "Evaluation of stereoscopic trace particle records of turbulent flow fields", Review of Scientific Instruments, 48, pp. 738-746.

Ewan, B.C.R., 1979a, "Holographic particle velocity measurement in the Fraunhofer plane", Applied Optics, 18, pp. 623-626.

Ewan, B.C.R., 1979b, "Particle velocity distribution measurement by holography", Applied Optics, 18, pp. 3156-3160.

Gauthier, V. and Reithmuller, M.L., 1988, "Application of PIDV to complex flows: measurements of the third component", VKI Lecture series on Particle Image Displacement Velocimetry, Brussels.

Gharib, M. and Willert, C., 1989, "Particle tracing: Revisited", Lecture notes in Engineering, Advances in Fluid Flow Measurements, ed. M. Gad-el-Hak, Springer-Verlag, New York, USA, 45, pp. 109-126.

Gonzalez R.C. and Wintz, P., 1987, "Digital Image Processing", Second Edition, Addison-Wesley Publishing Company, Don Mills, Canada.

Guzennec, Y.G. and Kiritsis, N., 1989, "Statistical investigation of errors in particle image velocimetry", Proceedings of ICALEO '89 - Optical methods in flow and particle diagnostics, SPIE Proceedings, 1404, Orlando, Florida, pp. 128-138.

Hassan, Y.A., Blanchat, T.K. and Seeley Jr., C.H., 1992, "PIV flow visualization using particle tracking techniques", Measurement Science and Technology, 3, pp. 633-642.

Johnson, R.R., 1974, "Study on the structure of turbulent shear in wall near layers", Ph.D Dissertation, Department of Engineering Sciences, University of Florida.

Kasagi, N., Ninomiya, N. and Hirata, M., 1988, "Three-dimensional velocity measurement in a turbulent jet by digital image processing", Proceedings of First World Congress on Experimental Heat Transfer, Fluid Mechanics and Thermodynamics, Dubrovnik, Yugoslovia, pp. 1502-1509.

Kaufmann, G.H., Ennos, A.E., Gale, B. and Pugh, D.J., 1980, "An electro-optic readout system for the analysis of speckle photographs", J. Phys. E : Sci. Instrum., 13, pp. 579-584.

Kent, J.C. and Eaton, A.R., 1982, "Stereo photography of neutral density He-filled bubbles for 3-D fluid motion studies in an engine cylinder", Applied Optics, 21, pp. 904-912.

Khalighi, B. and Lee, Y.H., 1989, "Particle tracking velocimetry: An automatic image processing algorithm", Applied Optics, 28, pp. 4328-4332.

Kirita, A., Pickering, C.J.D. and Halliweil, N.A., 1986, "Particle image velocimetry: A new approach to fringe analysis", Optics and Lasers in Engineering, 7, pp. 137-147.

Kline, S.J. and McClintock, F.A., 1953, "Describing uncertainties in single sample experiments", Mechanical Engineering, January, pp. 3-8.

Kobayashi, T., Saga, T. and Sekimoto, K., 1989, "Velocity measurement of three-dimensional flow around rotating parallel disks by digital image processing", Proceedings of Flow Visualization - 1989, Winter Annual Meeting of the ASME, FED Vol. 85, San Francisco, USA, pp. 29-36.

Lenz, R.K. and Tsai, R.Y., 1987, "Techniques for calibration of the scale factor and image centre for high accuracy 3D machine vision metrology", Proceedings of IEEE International Conference on Robotics and Automation, Raleigh, NC.

Larijani, R., 1992, "Parametric study of a digital whole field measurement technique for two-dimensional flow", M.A.Sc Thesis, University of Windsor, Windsor, Canada.

Maas, H.G., Gruen, A. and Papantoniou, D., 1993, "Particle tracking velocimetry in three-dimensional flows - part 1. Photogrammetric determination of particle coordinates", Experiments in Fluids, 15, pp. 133-146.

Majumdar, A., Stoeve, P., Fales, J.L., Algazi, V.R. and Stewart, J.E., 1987, "Teaching computers to track particles. II. Auto tracking algorithm and coordinate transformation", Journal of Imaging Science, 31, pp. 208-219.

Malyak, P.H. and Thompson, B.J., 1984, "Particle displacement and velocity measurement using holography", Optical Engineering, 23, pp. 567-576.

Marko, K.A. and Rimai, L., 1985, "Video recording and quantitative analysis of seed particle track images in unsteady flows", Applied Optics, 28, pp. 3666-3672.

Marquardt, D.W., 1963, "An algorithm for least-squares estimation of non-linear parameters", Journal of Society of Industrial and Applied Mathematics, 11, pp. 431-441.

Menzel, R. and Shoffner, F.M., 1970, "An investigation of Fraunhofer holography for velocimetry applications", Applied Optics, 9, pp. 2973-2978.

Meynart, R., 1982, "Digital image processing for speckle flow velocimetry", Review of Scientific Instruments, 53, pp. 110-111.

Nishino, K., Kasagi, N. and Hirata, M., 1989, "Three-dimensional particle tracking velocimetry based on automated digital image processing", Journal of Fluids Engineering, 111, pp. 384-391.

Okamoto, K., Madarame, H. and Shioya, R., 1991, "Measurement of velocity distribution in a tank by velocity vector histogram", FLUCOME '91, ASME, pp. 601-607.

Park, J.T., Muller, M.A. and Rezaie, B., 1989, "Digital image processing of laminar boundary layer data", Proceedings of Flow Visualization (ASME), San Francisco, pp. 870-894.

Peskin, C.S., 1972, "Flow patterns around heart valves", Ph.D Dissertation, Albert Einstein College of Medicine, Yeshiva University, NY.

Pickering, C.J.D. and Halliwell, N.A., 1985, "Particle image velocimetry: improving fringe signal-to-noise ratio with two-step photographic processing", Journal of Optical Society of America, 2, pp. 1721-1724.

Popovich, A.T. and Hummel, R.L., 1967, "A new method for non-disturbing turbulent flow measurements very close to a wall", Chemical Engineering Science, 22, pp. 21-25.

Prasad, A.K. and Adrian, R.J., 1993, "Stereoscopic particle image velocimetry applied to liquid flows", Experiments in Fluids, 15, pp. 49-60.

Praturi, A. and Brodkey, R.S., 1978, "A stereoscopic visual study of coherent structures in turbulent shear flow, Journal of Fluid Mechanics, 89, pp. 251-272.

Press, W.H., Teukolsky, S.A., Vetterling, W.T. and Flannery, B.P., Numerical Recipes in C: The Art of Scientific Computing, Second Edition, Cambridge University Press, 1992.

Racca, R.G. and Dewey, J.M., 1988, "A method for automatic particle tracking in a three-dimensional flow field", Experiments in Fluids, 6, pp. 25-32.

Schuster, P.R. and Wagner, J.W., 1988, "Holographic velocimetry for flow diagnostics", Experimental Mechanics, 28, pp. 402-408.

Sheu, Y. - H.E., Chang, T.P.K. and Tatterson, G.B., 1982, "A three-dimensional measurement technique for turbulent flows", Chemical Engineering Communication, 17, pp. 67-83.

Sid-Ahmed. M.A. and Boraie, M.T.M., 1990, "Dual camera calibration for 3-D machine vision metrology", IEEE Transactions on Instrumentation and Measurement, 39, pp. 512-516.

Tatterson, G.B., Yuan, H.S. and Brodkey, R.S., 1980, "Stereoscopic visualization of the flows for pitched blade turbines", Chemical Engineering Science, 35, 1369-1375.

Trolinger, J.D., Belz, R.A. and Farmer, W.M., 1969, "Holographic techniques for the study of dynamic particle fields", Applied Optics, 8, pp. 957-961.

Willert, C.E. and Gharib, M., 1991, "Digital particle image velocimetry", Experiments in Fluids, 10, pp. 181-193.

Winter, E.F., 1958, "Flow visualization techniques applied to combustion problems", Journal of Royal Aeronautical Society, 62, pp. 268-276.

Yuan, G., Zhang, Z., Jin, Y. and Chen, C., 1986, "The holography of high speed particles and data processing", Proceedings of Fourth International Symposium on Flow Visualization, Paris, France, ed, Veret, pp. 61-66.

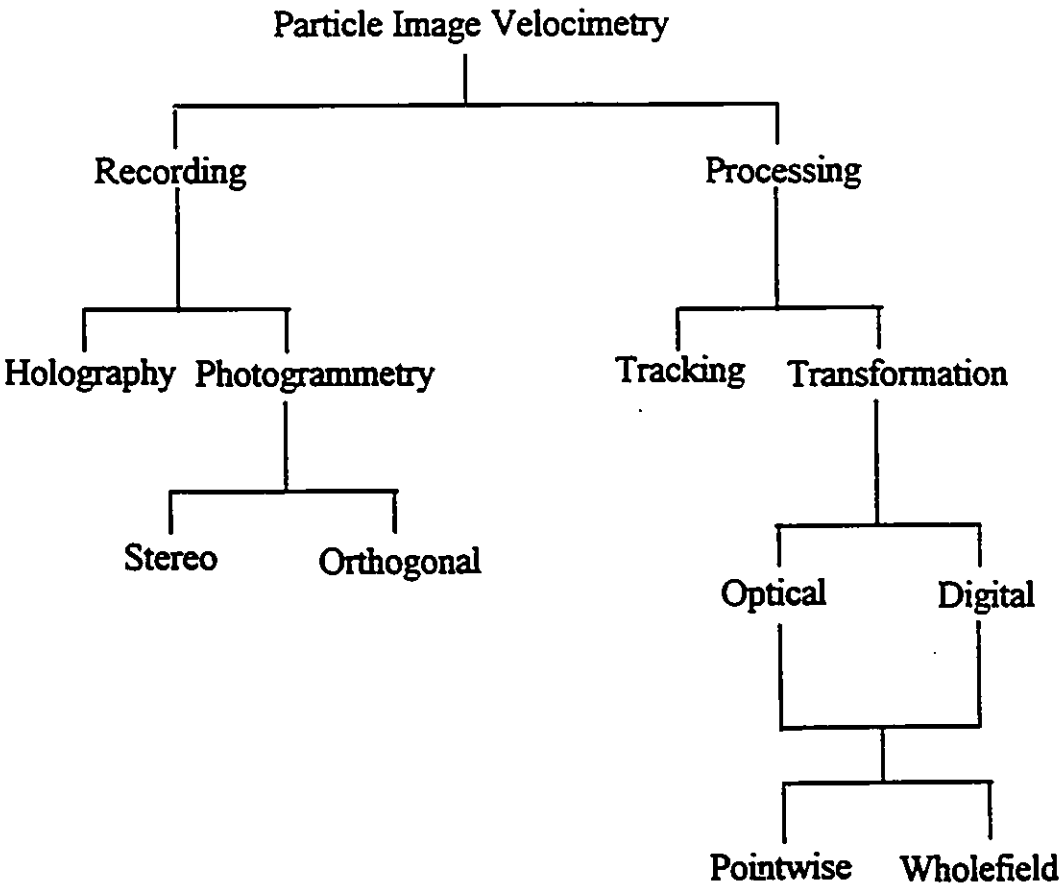

Figure 1.1 Classification of particle imaging techniques

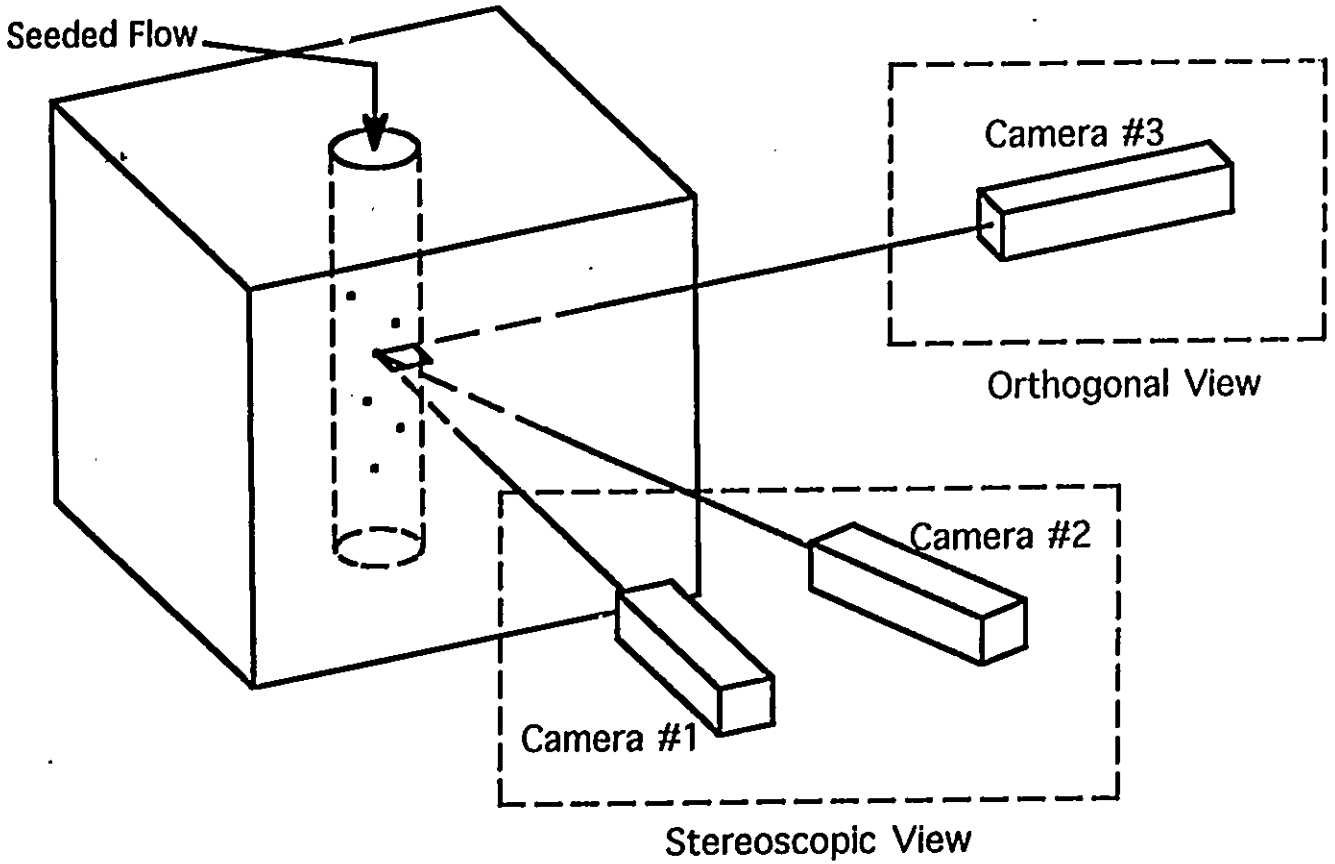

Figure 1.2 Photogrammetric recording arrangement used for flow measurement

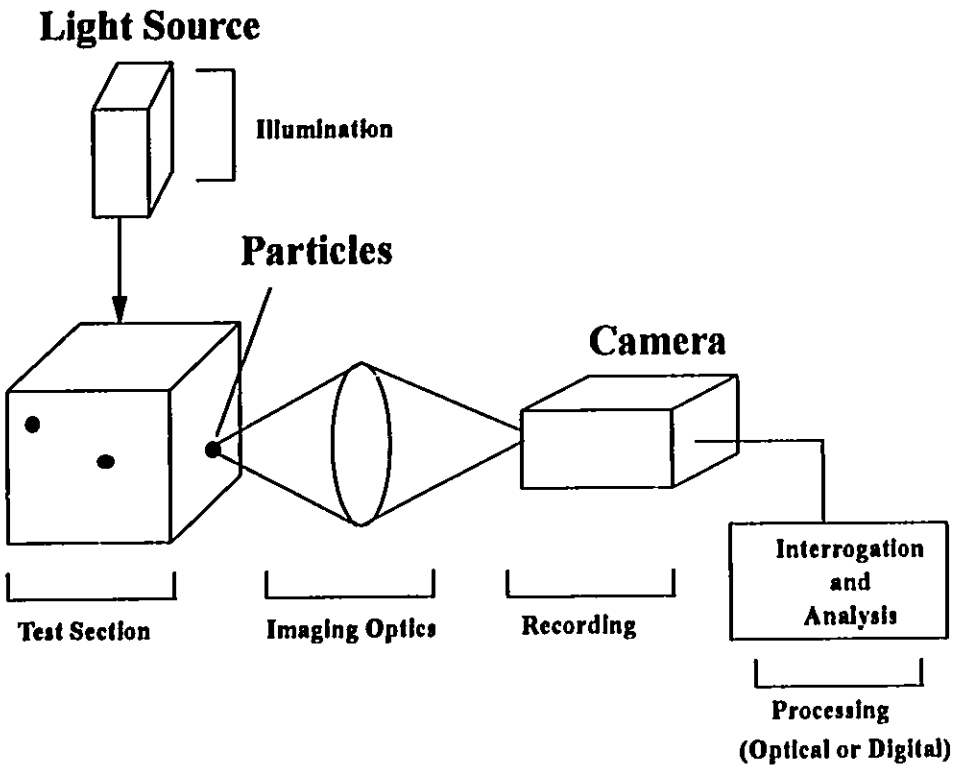

Figure 2.1 Elements of a Particle Imaging System

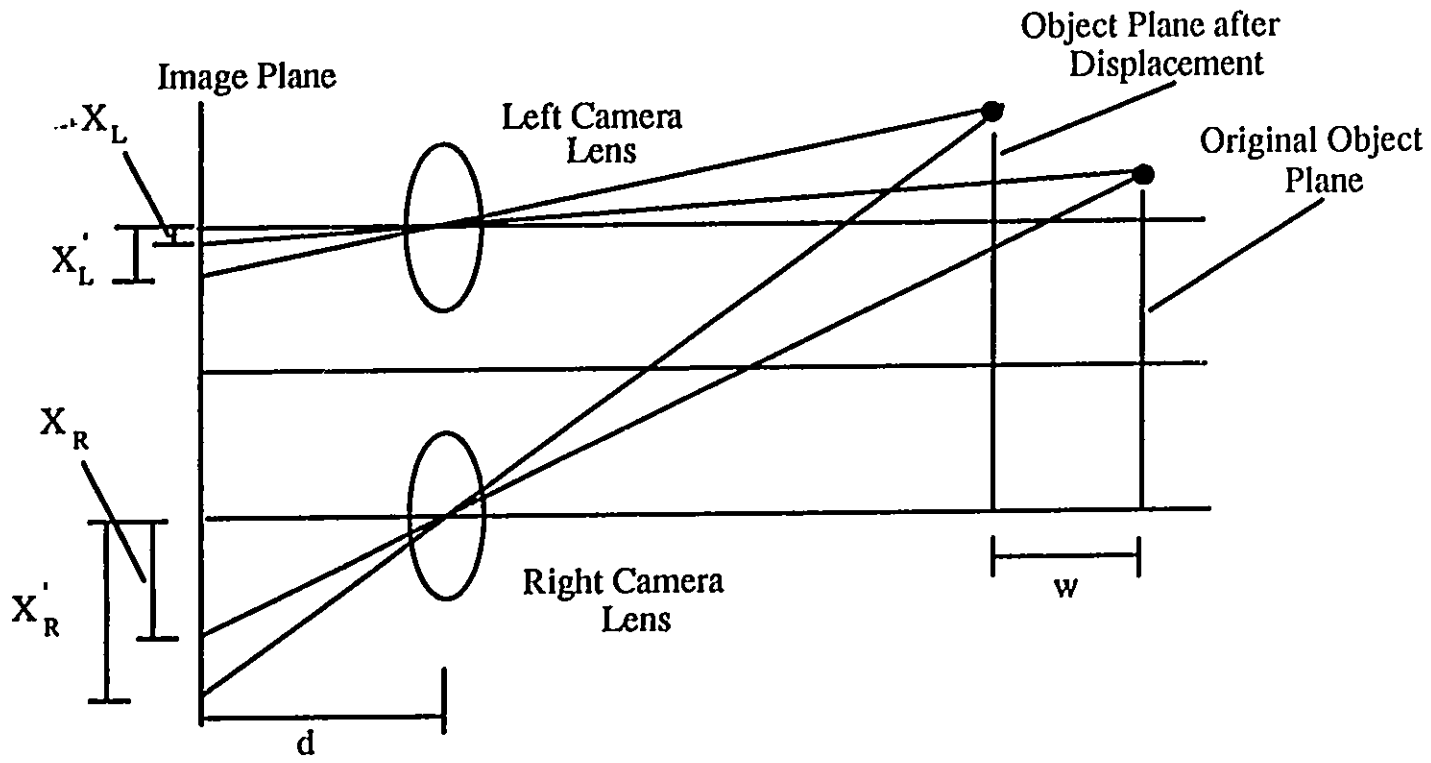

Figure 2.2 Arrangement for recording particle images in stereogrammetric approach

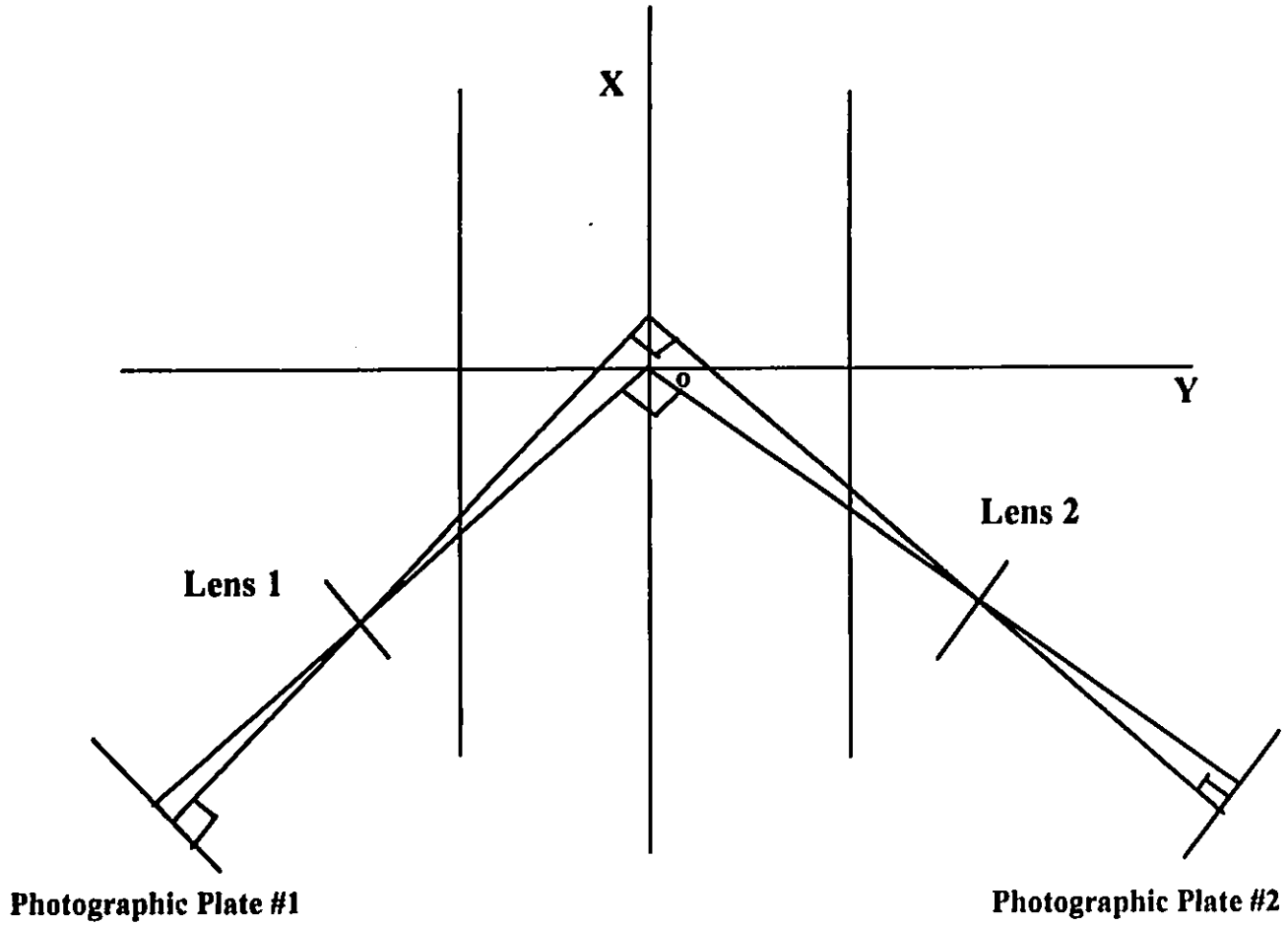

Figure 2.3 Arrangement for recording particle images in orthogonal-view approach

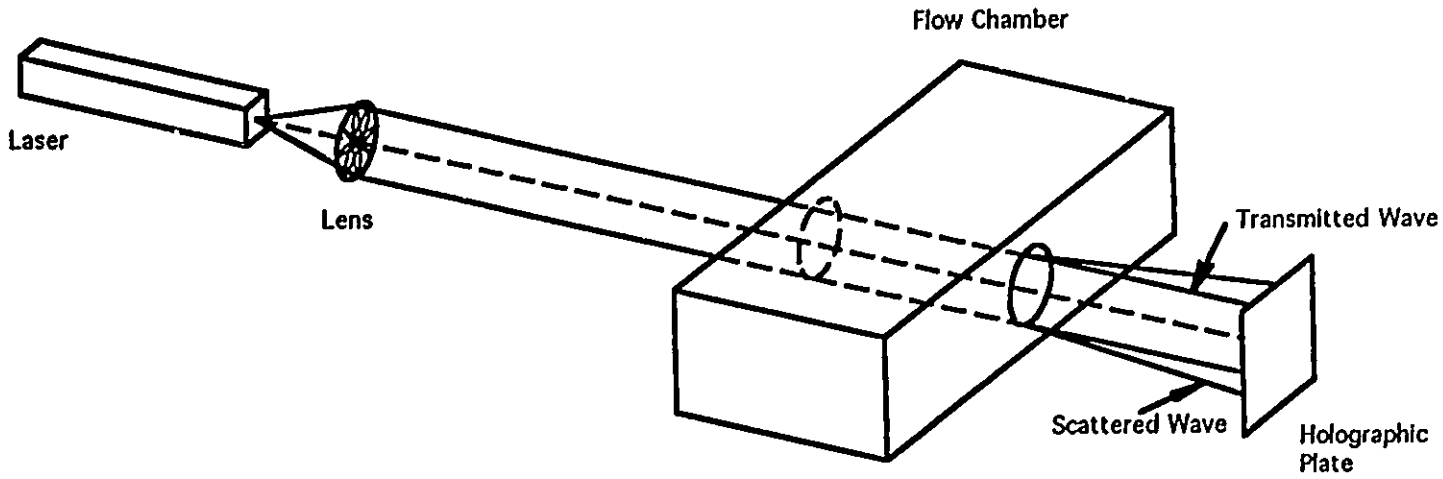

Figure 2.4 A schematic diagram of the holographic recording process

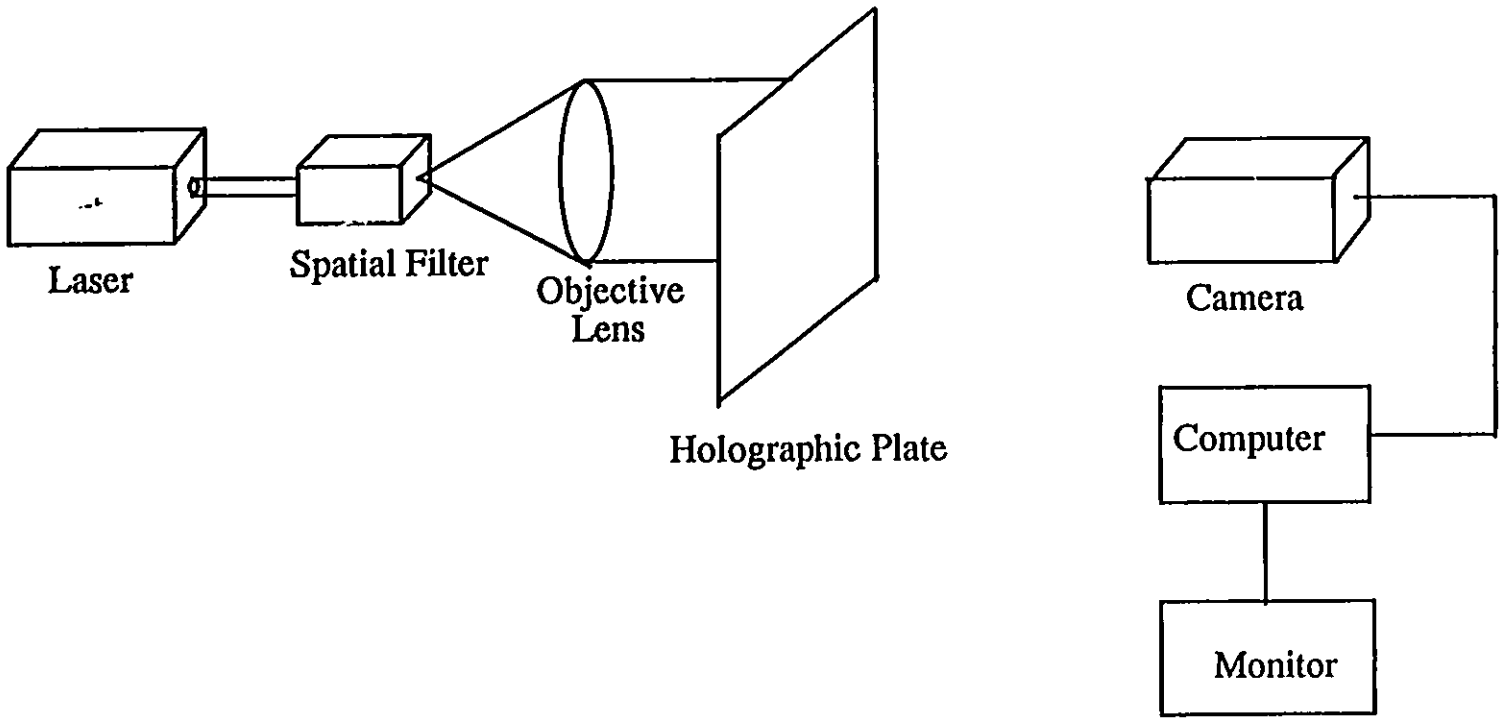

Figure 2.5 A schematic diagram of the reconstruction process in holography

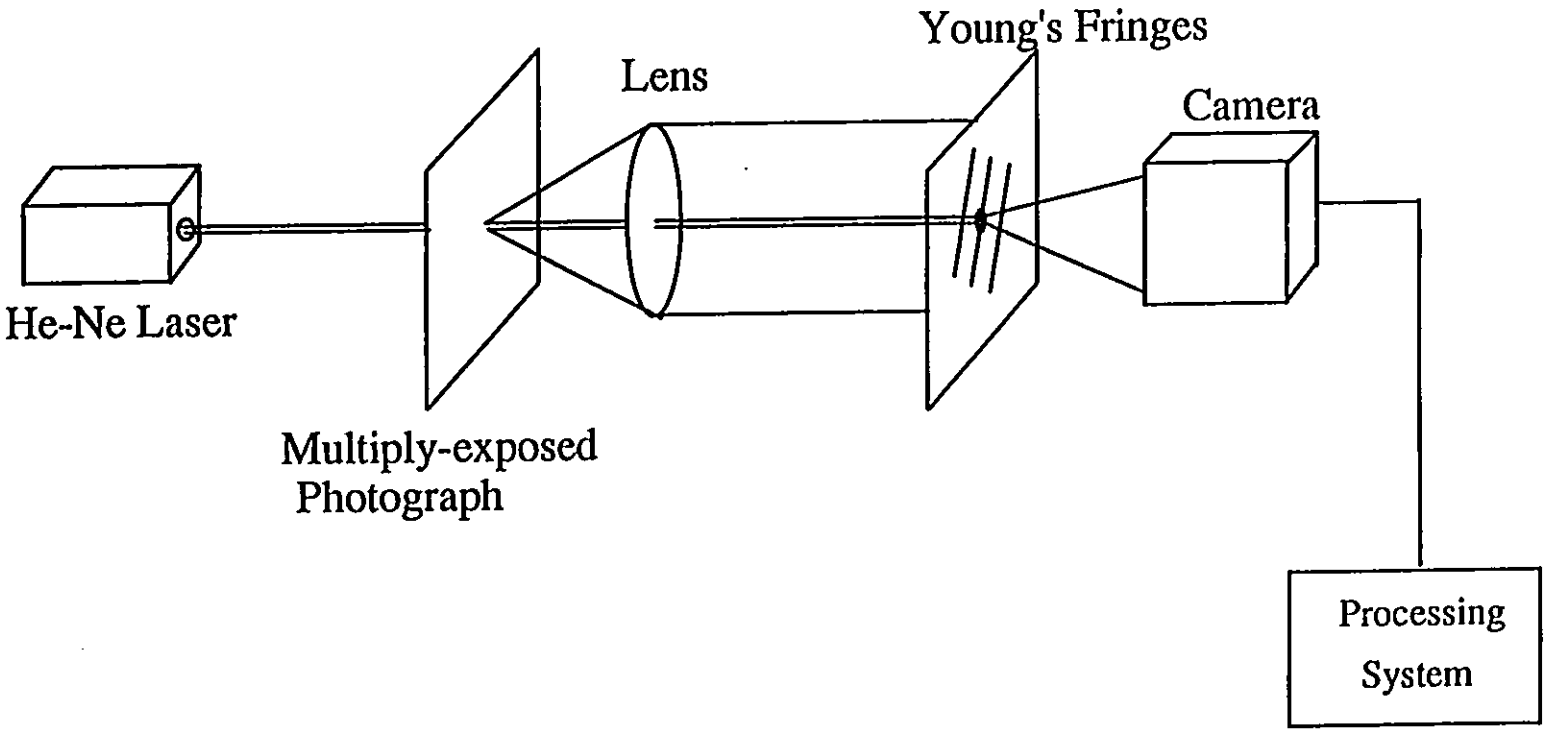

Figure 2.6 Optical set-up for pointwise processing

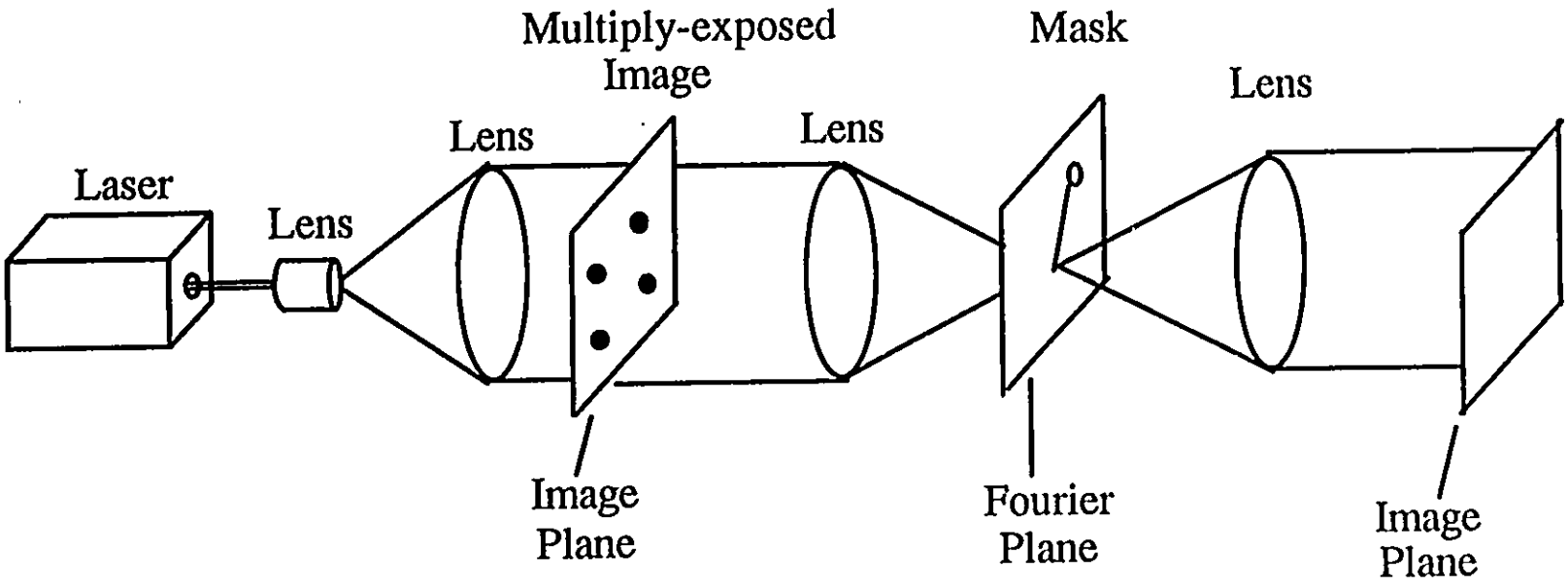

Figure 2.7 Optical set-up for whole-field processing

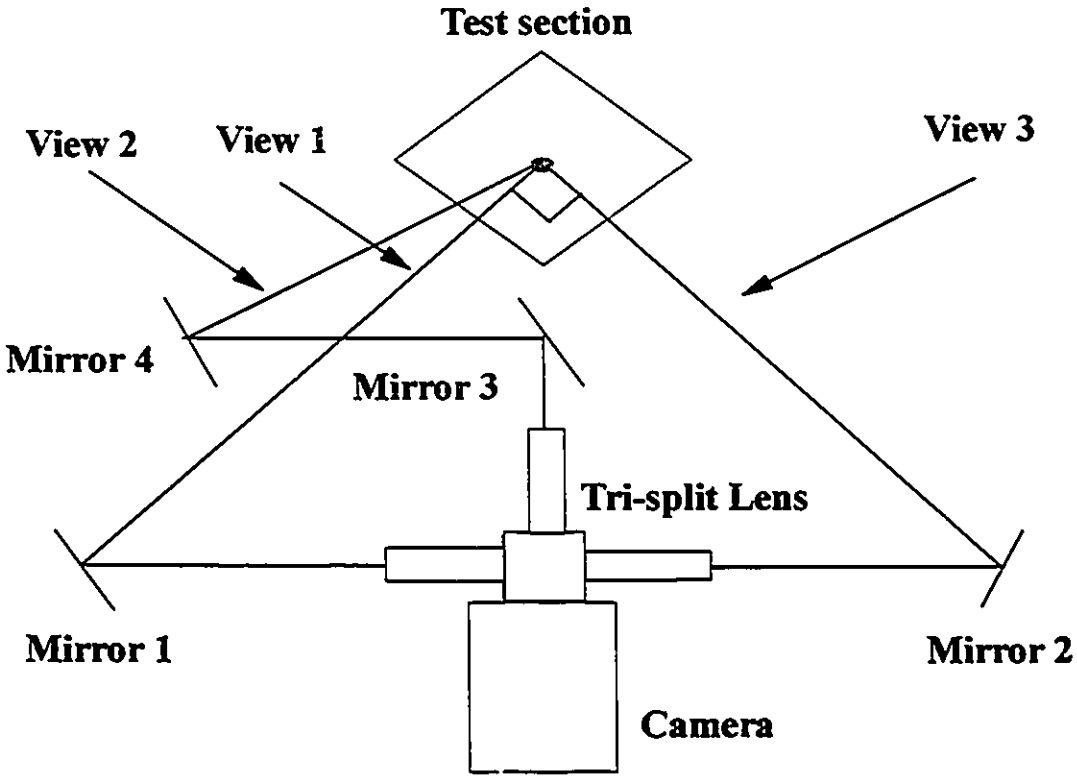

Figure 3.1 A schematic diagram of the experimental set-up

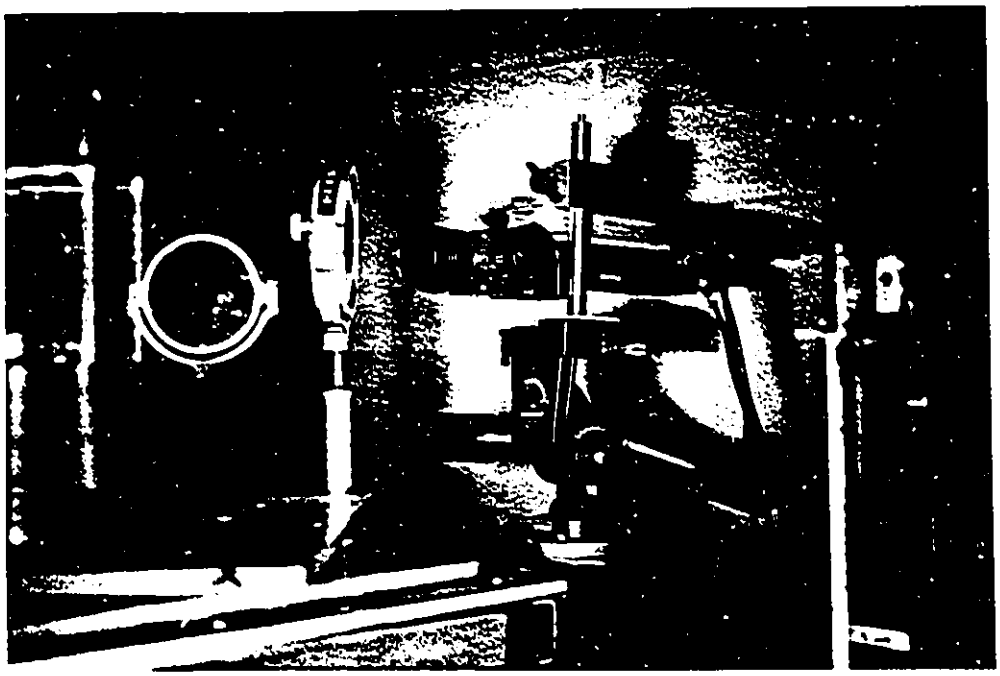

Figure 3.2 A photograph of the optical system

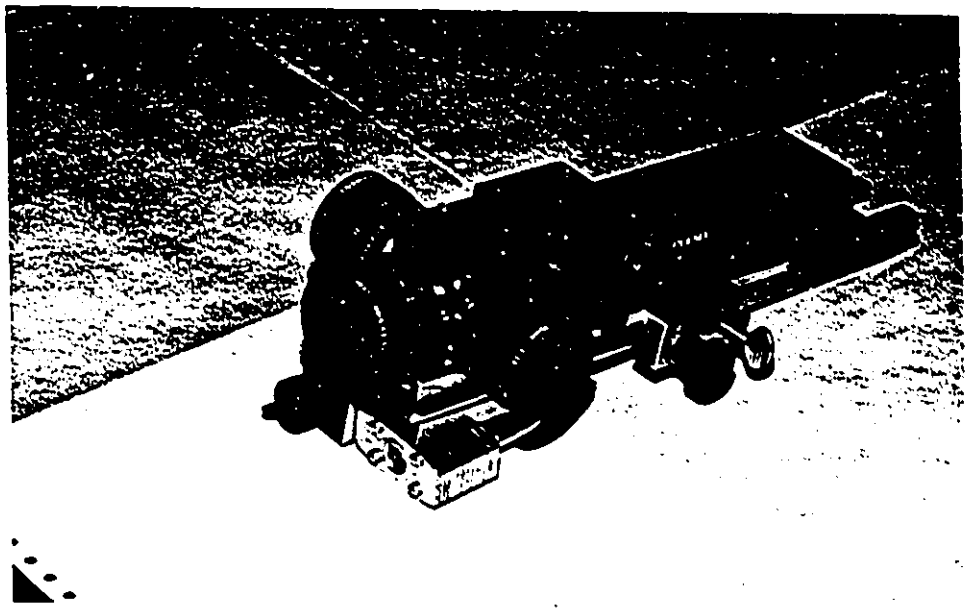

Figure 3.3 A photograph of the CCD camera and the tri-split lens system

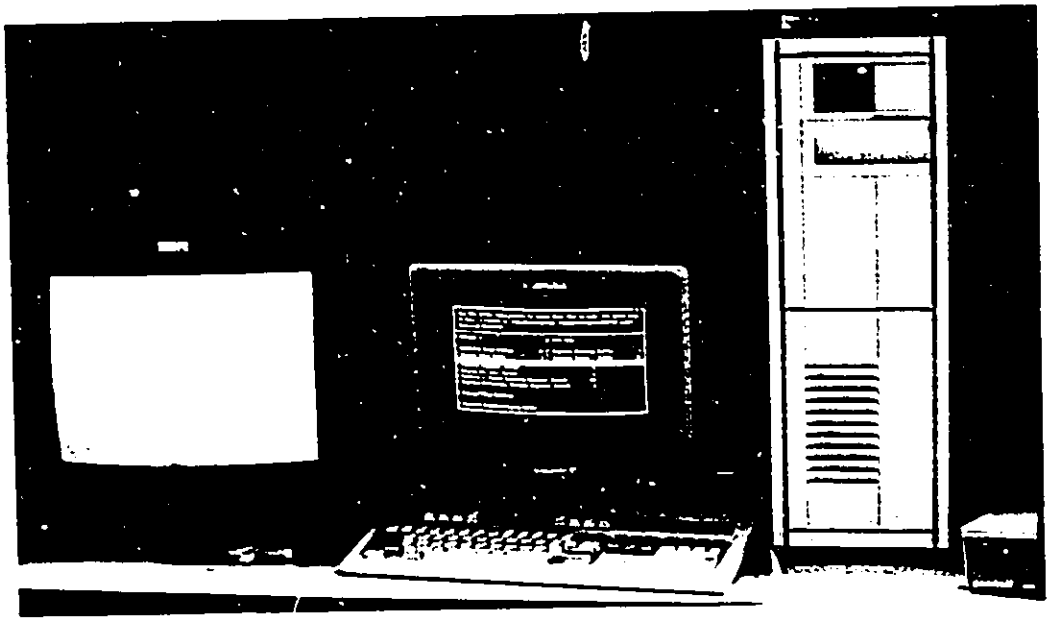

Figure 3.4 A photograph of the data processing unit

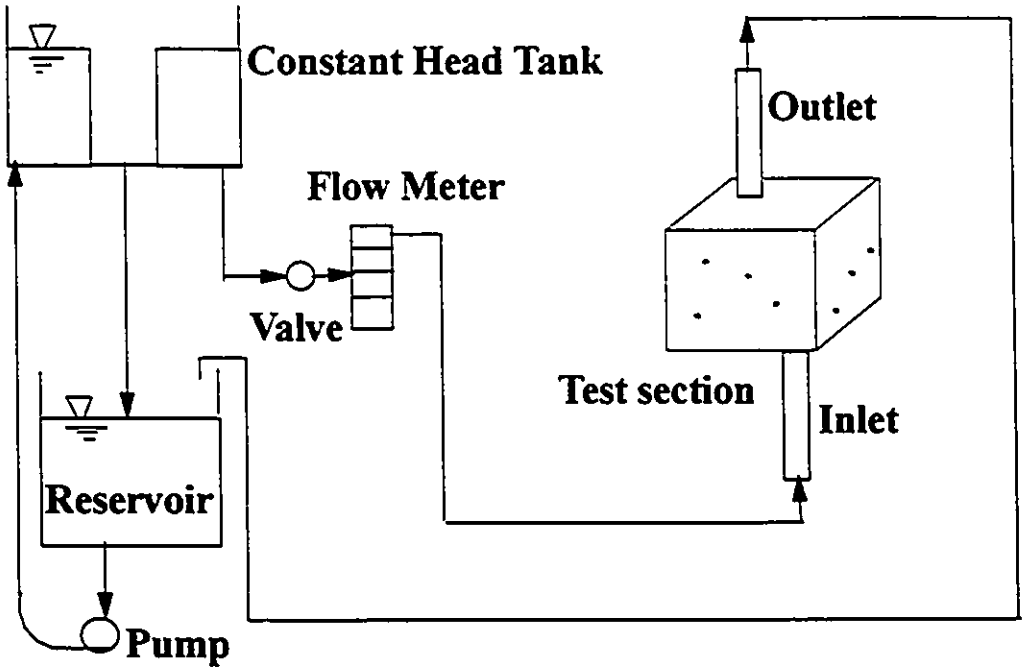

Figure 3.5 A schematic diagram of the test flow facility

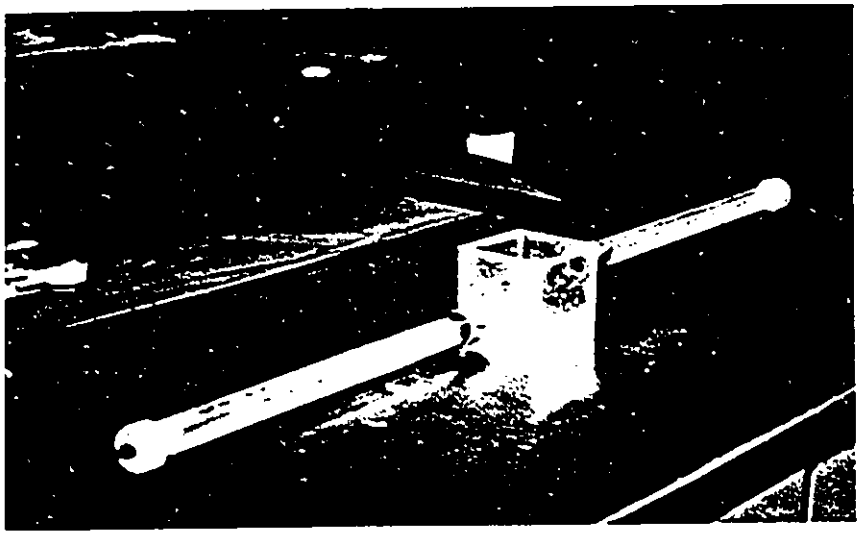

Figure 3.6 A photograph of the cubical test section

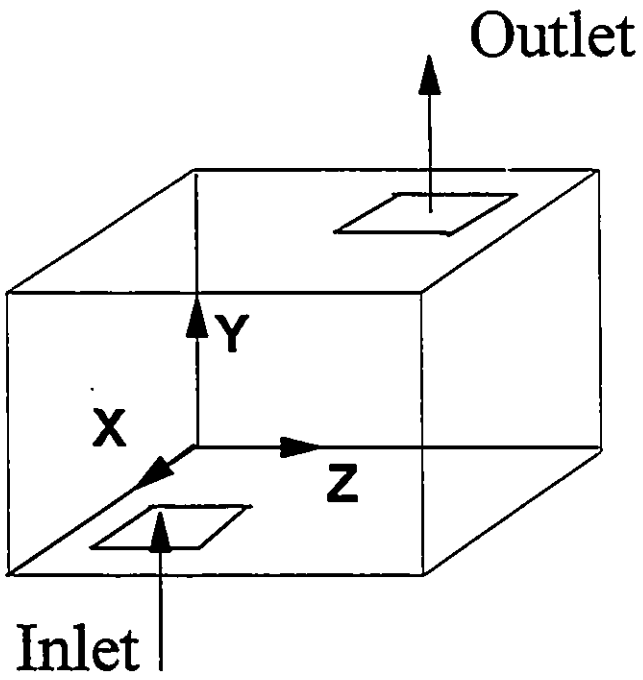

Figure 3.7 A schematic diagram to indicate the placement of inlet and outlet in the test section

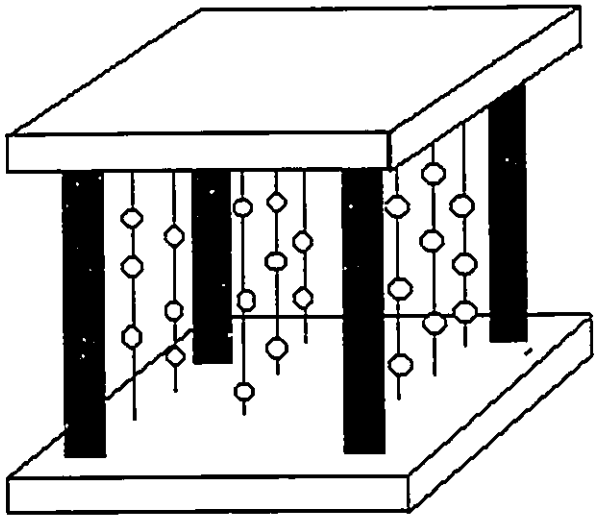

Figure 3.8 A schematic diagram of the calibration target

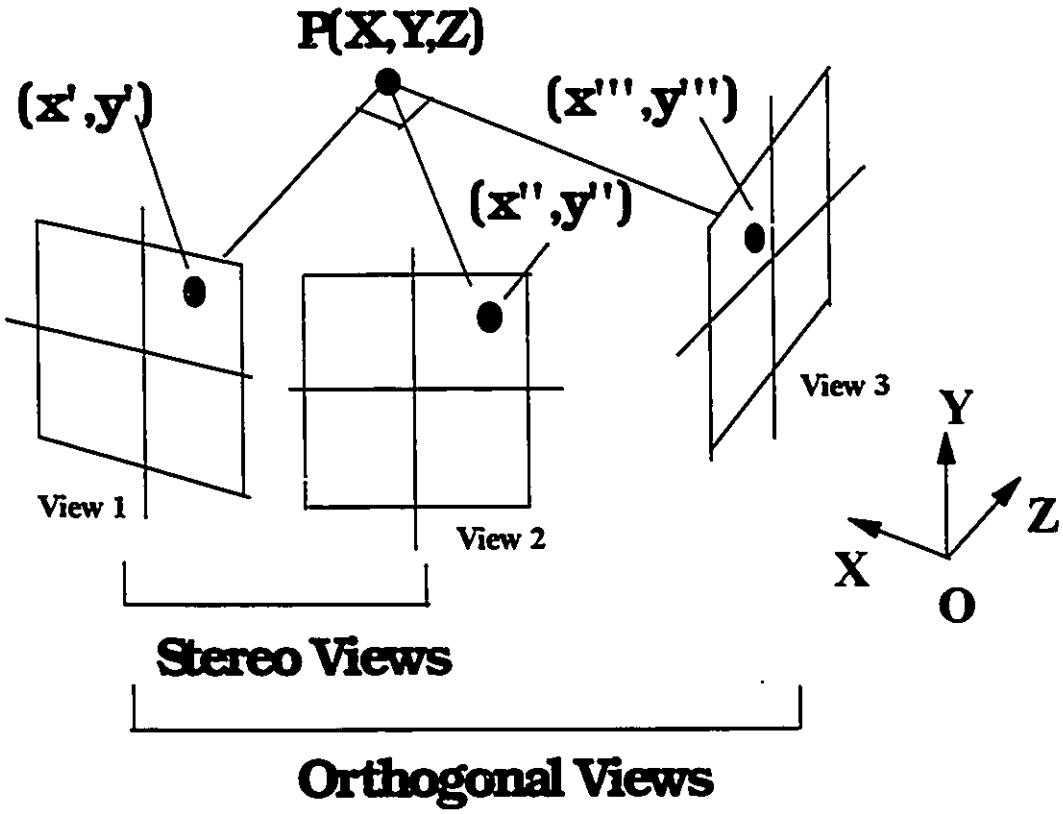

Figure 4.1 A schematic diagram of the imaging system

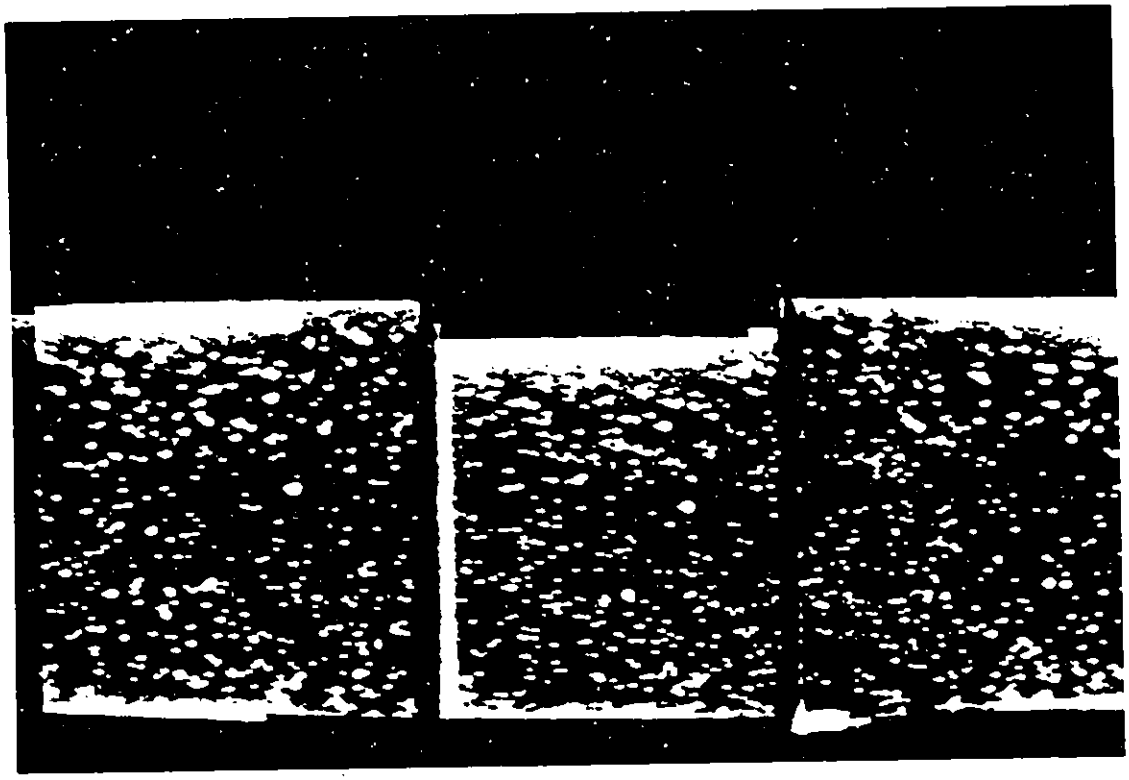

Figure 4.2 A photograph of the digitized image

u1	u2	u3
u4	u5	u6
u7	u8	u9

(a)

x1	x2	x3
x4	x5	x6
x7	x8	x9

(b)

0	-1	0
-1	4	-1
0	-1	0

(c)

Figure 4.3 Laplacian sharpening operator
(a) Mask
(b) 3 x 3 image region
(c)Mask used to compute the Laplacian

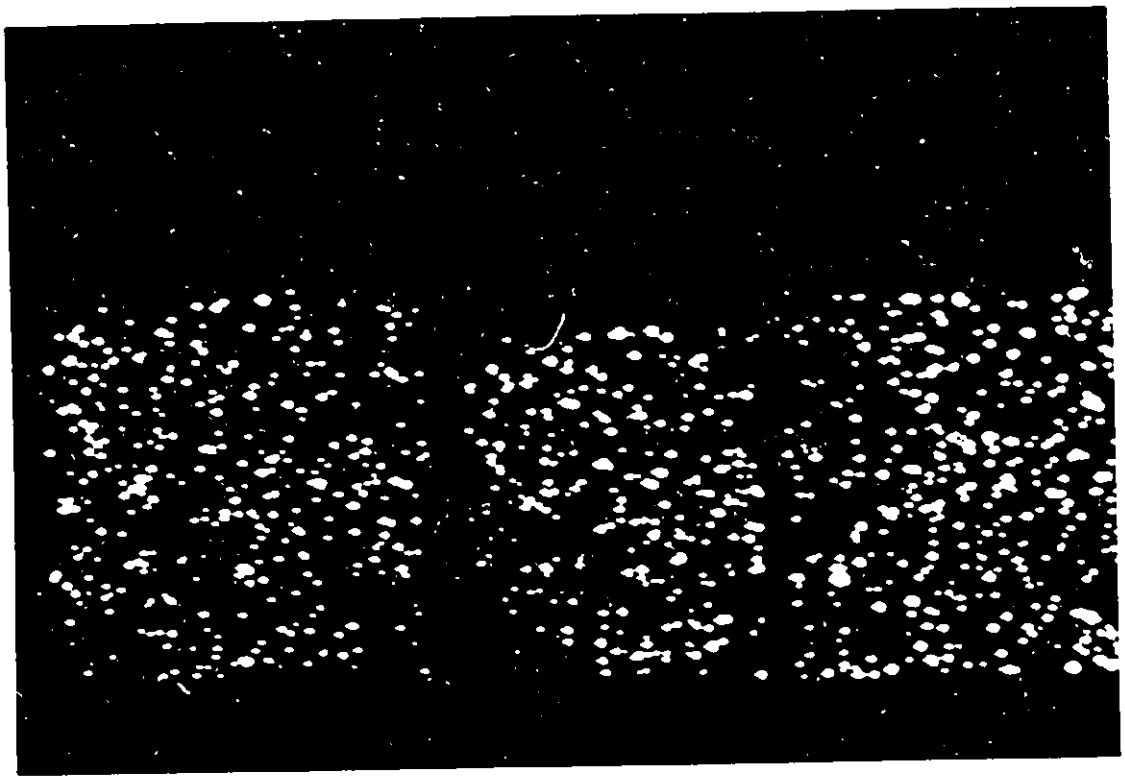

Figure 4.4 A photograph of the thresholded image

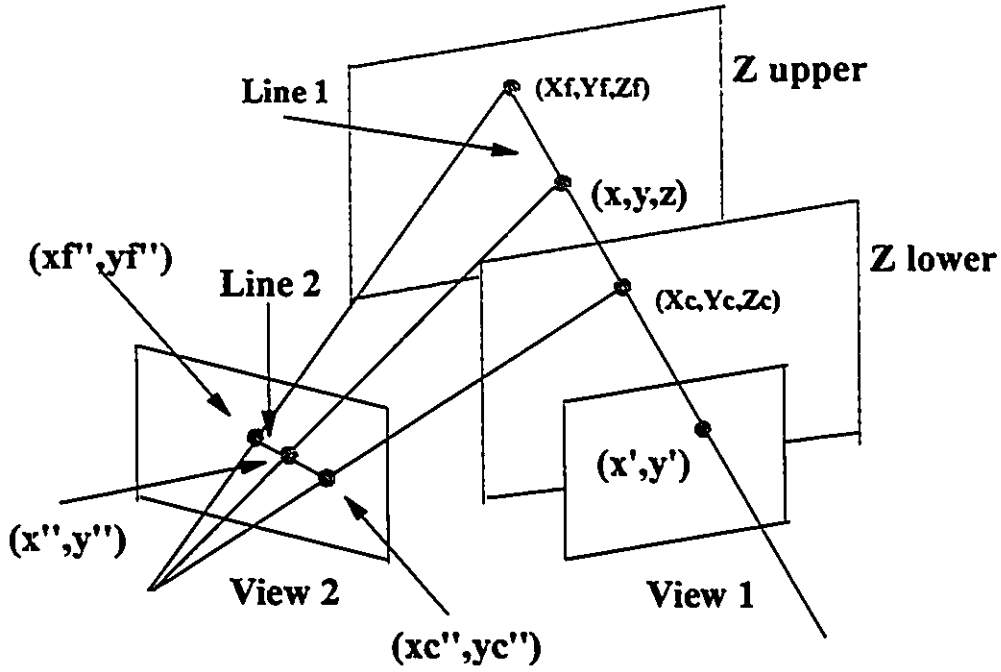

Figure 4.5 A schematic diagram of the epipolar method

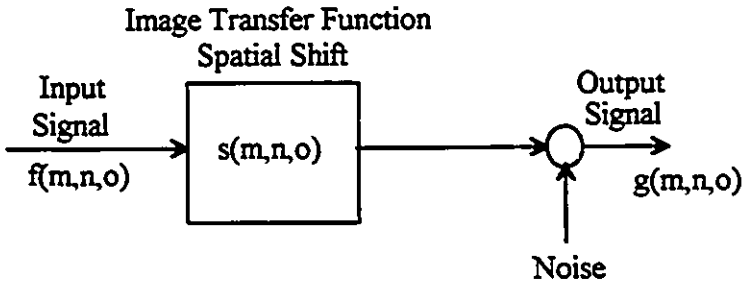

Figure 4.6 A linear system model of two sequential data sets

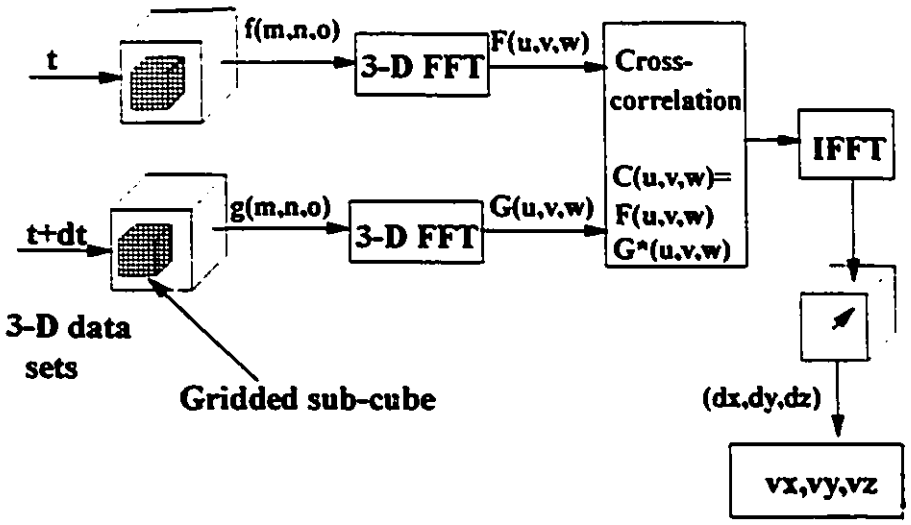

Figure 4.7 A schematic diagram of the cross correlation approach

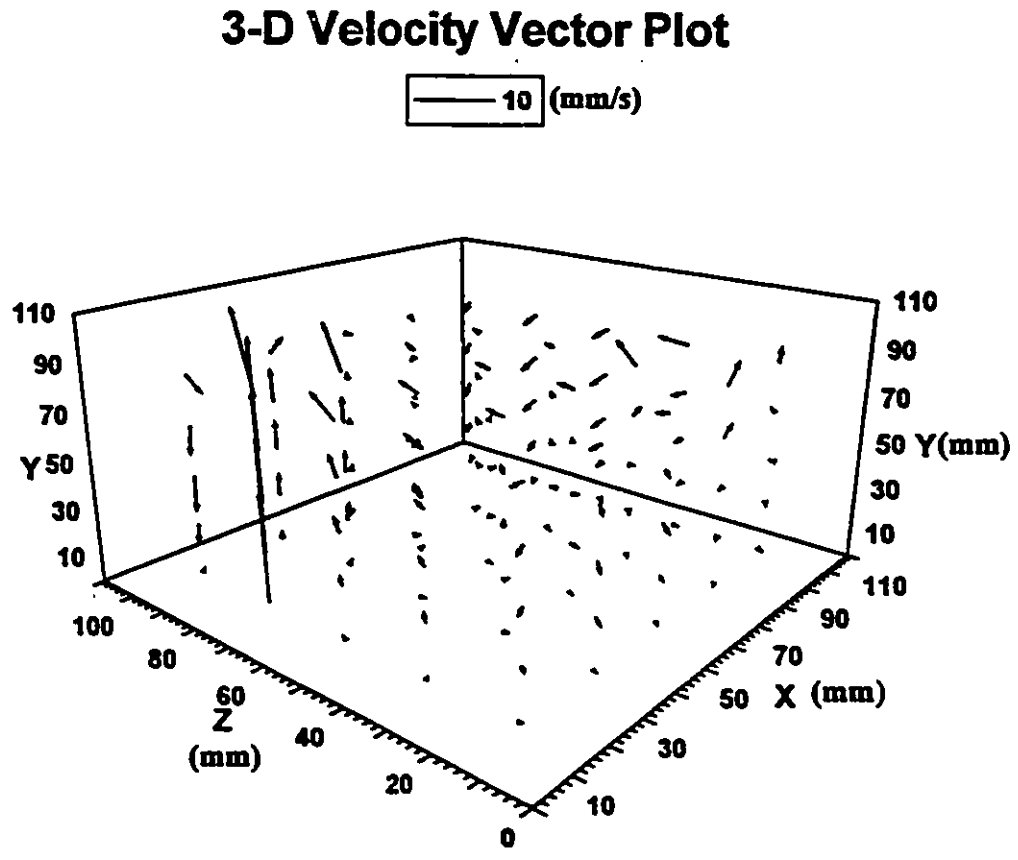

Figure 5.1 3-D velocity vector plot obtained from the experimental investigation

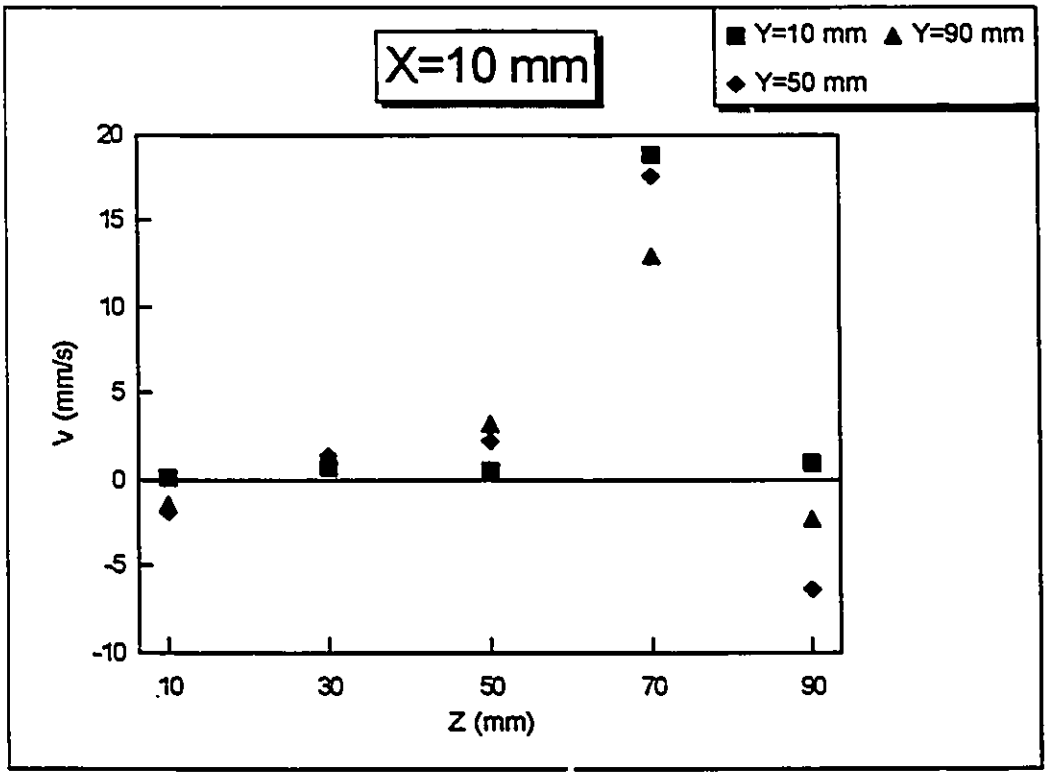

Figure 5.2 V-component velocity profiles on the projected plane X = 10 mm

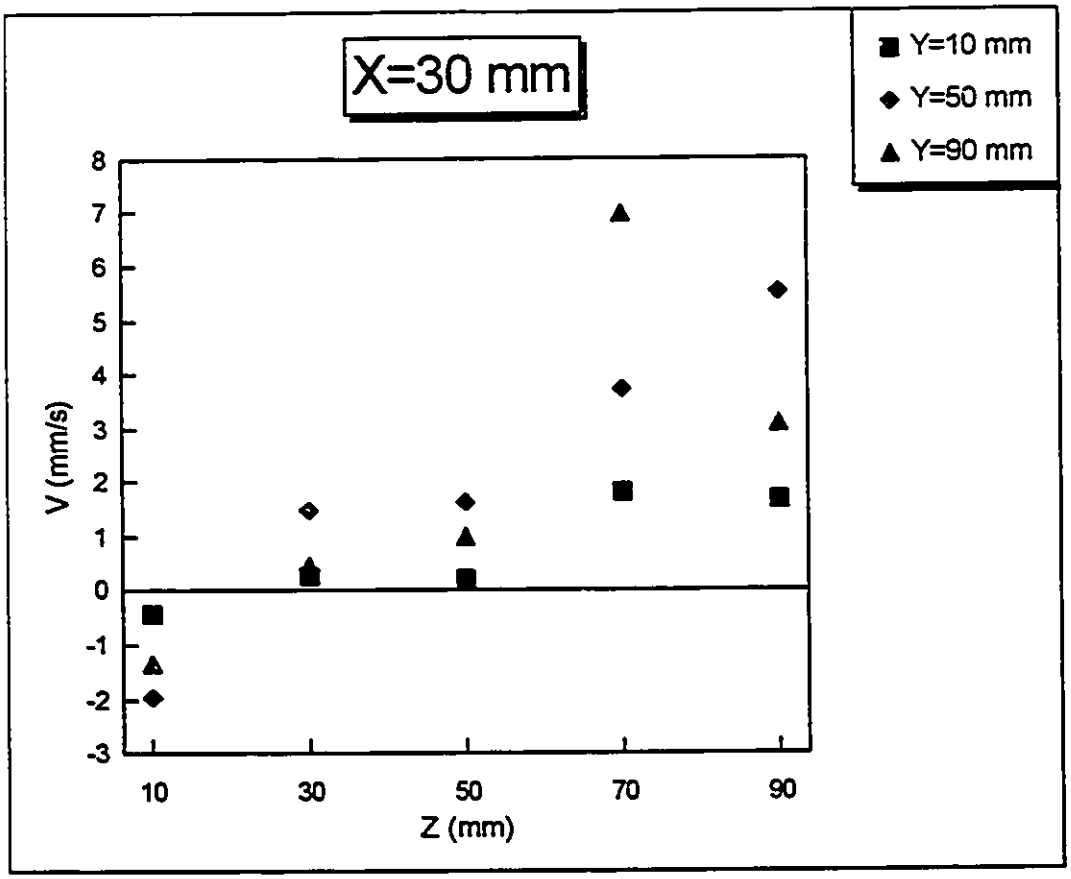

Figure 5.3 V-component velocity profiles on the projected plane X = 30 mm

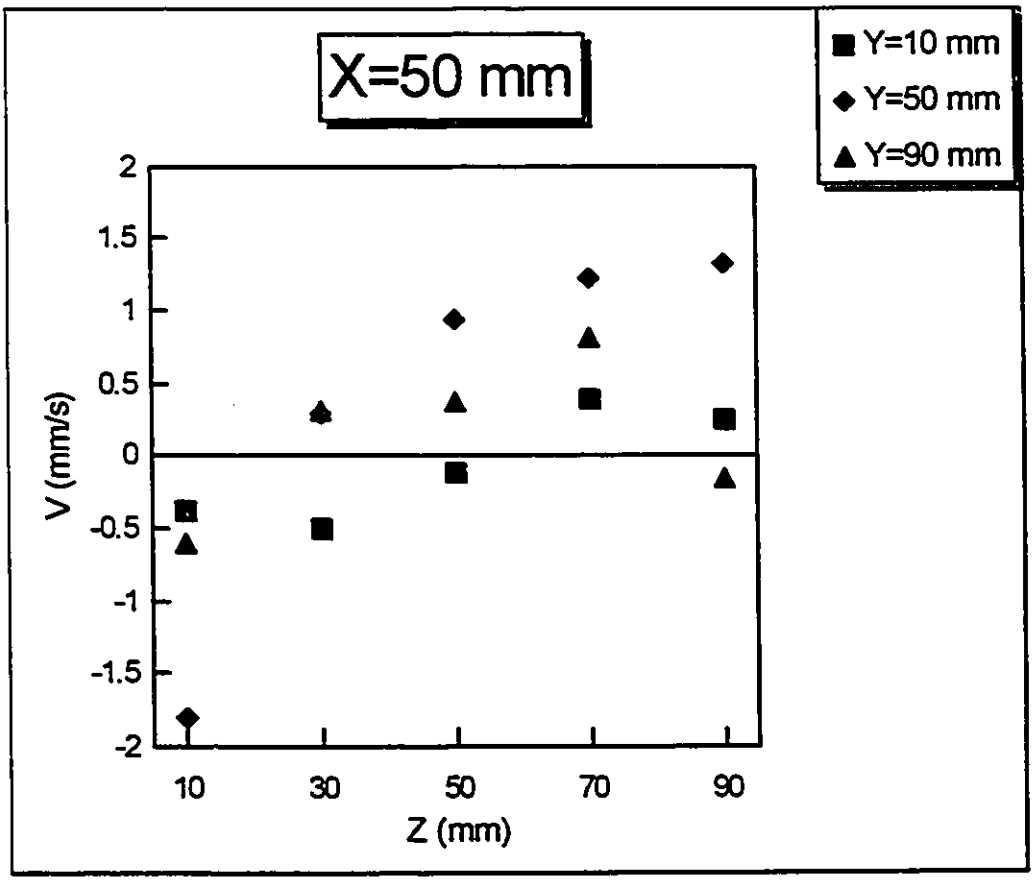

Figure 5.4 V-component velocity profiles on the projected plane X = 50 mm

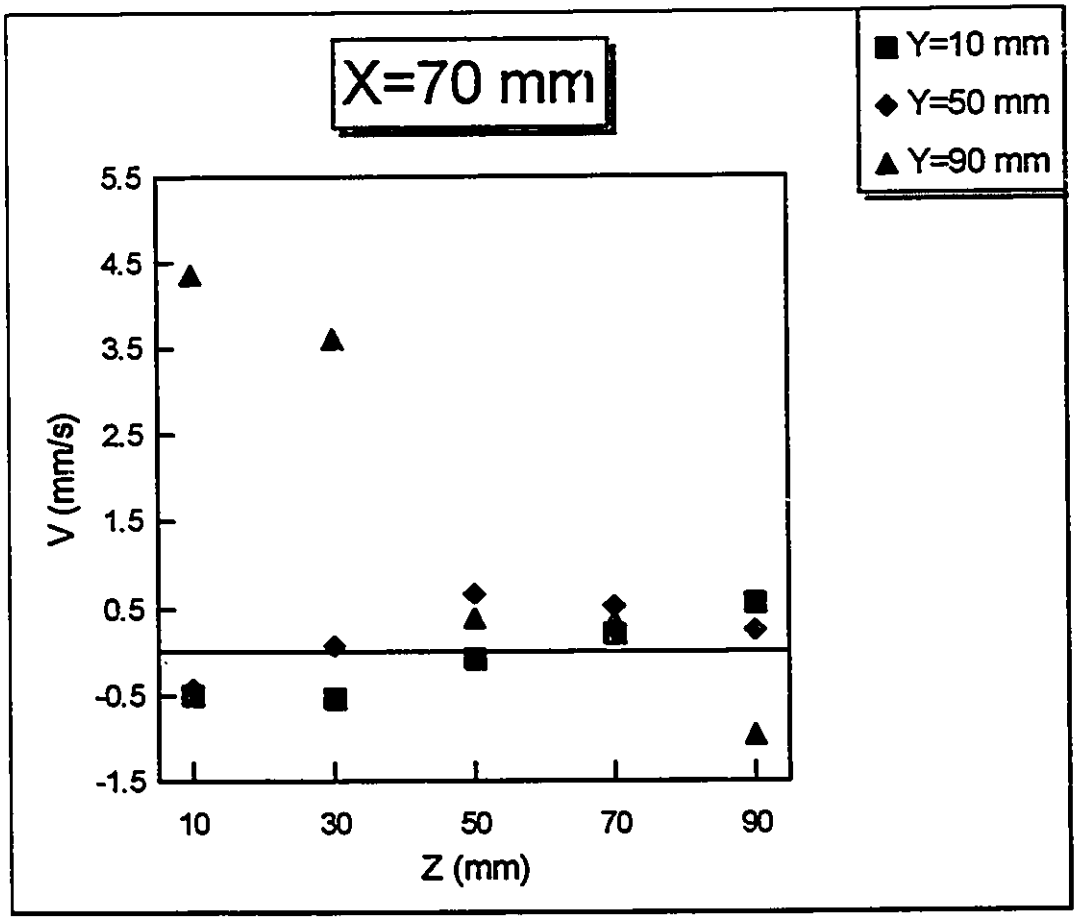

Figure 5.5 V-component velocity profiles on the projected plane X = 70 mm

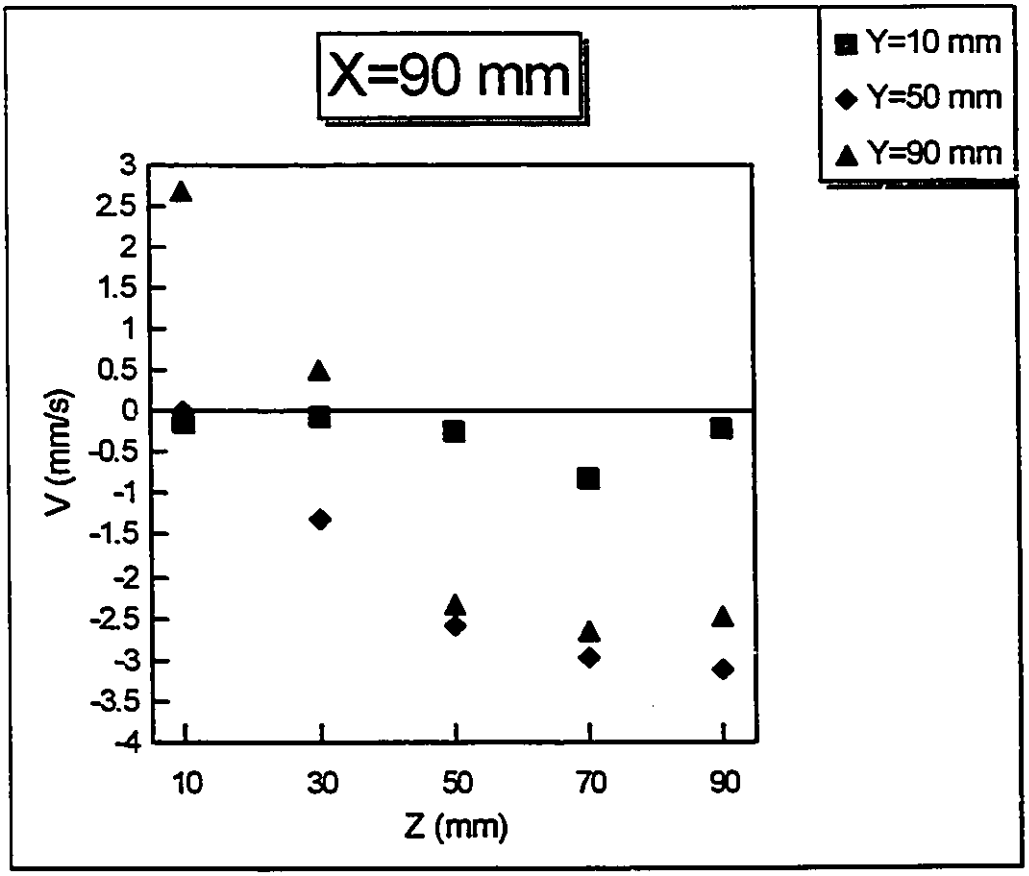

Figure 5.6 V-component velocity profiles on the projected plane X = 90 mm

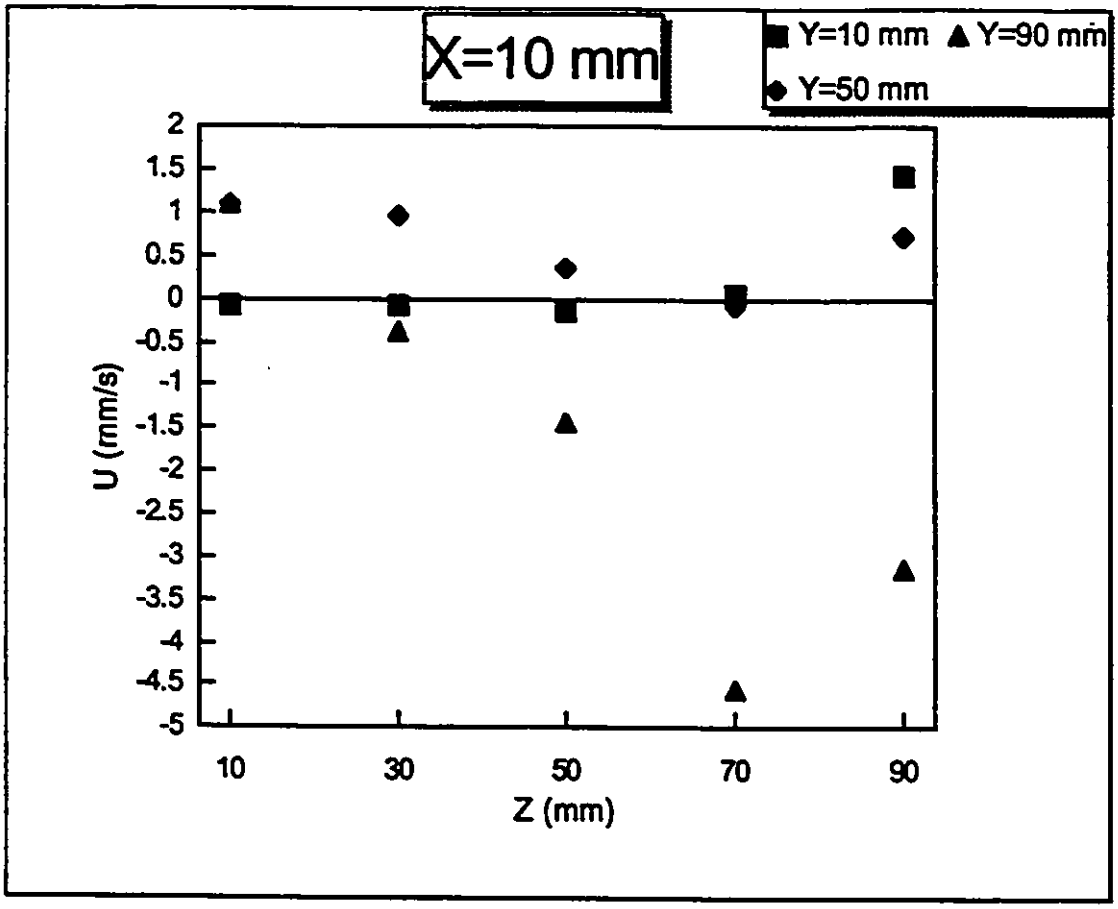

Figure 5.7 U-component velocity profiles on the projected plane X = 10 mm

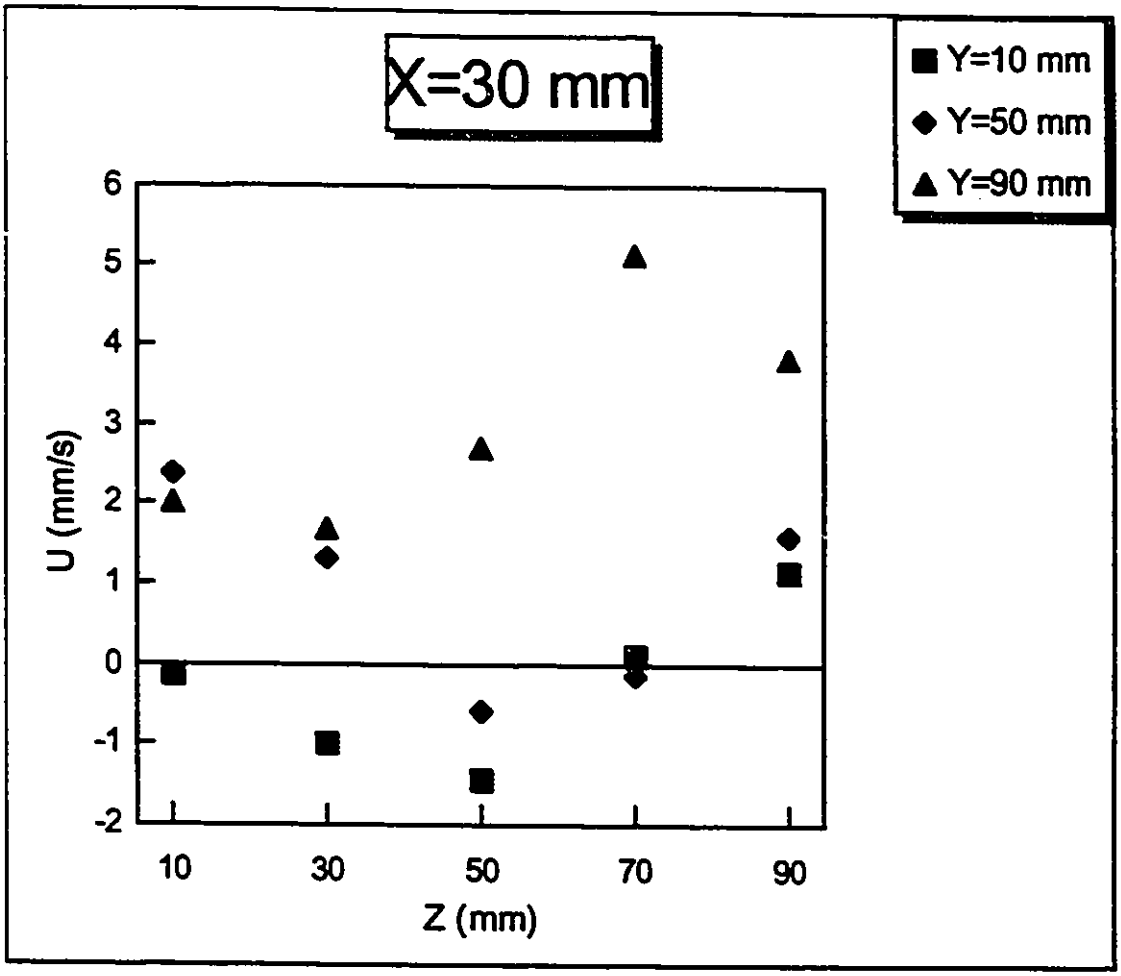

Figure 5.8 U-component velocity profiles on the projected plane X = 30 mm

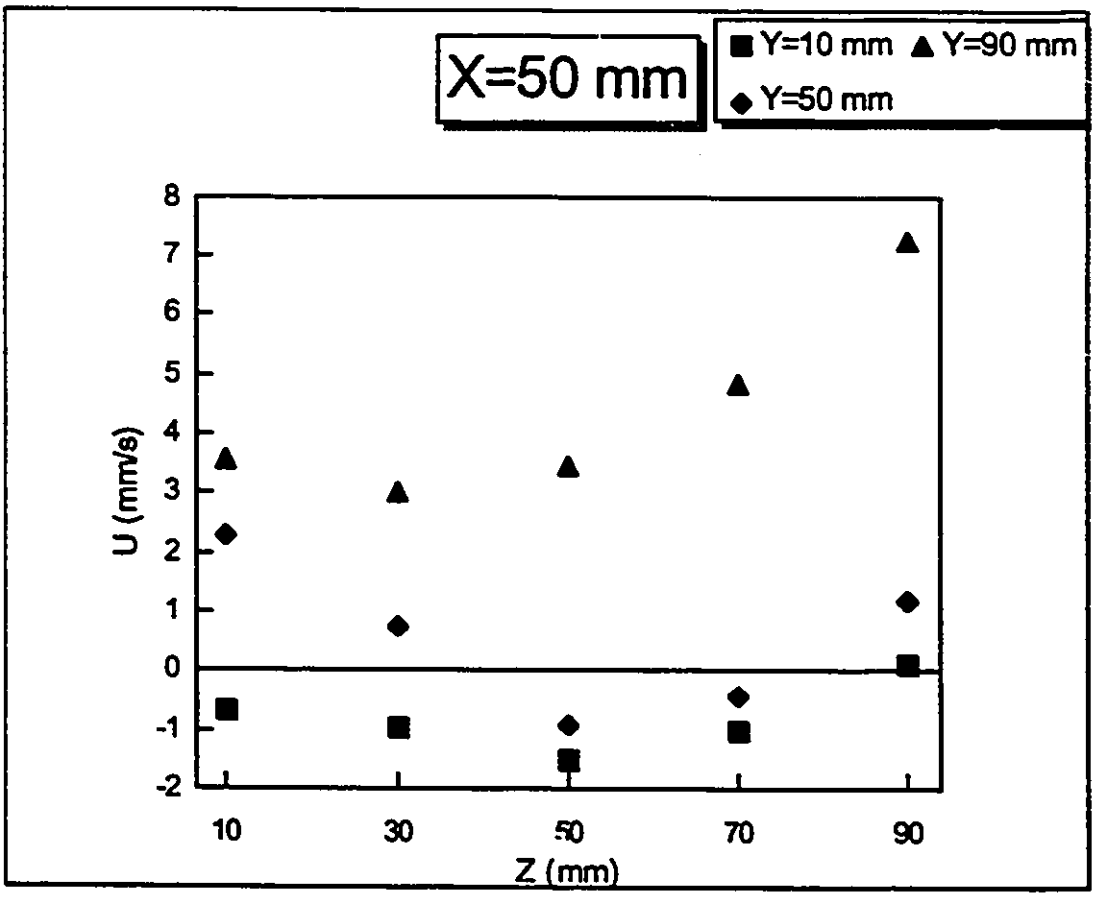

Figure 5.9 U-component velocity profiles on the projected plane X = 50 mm

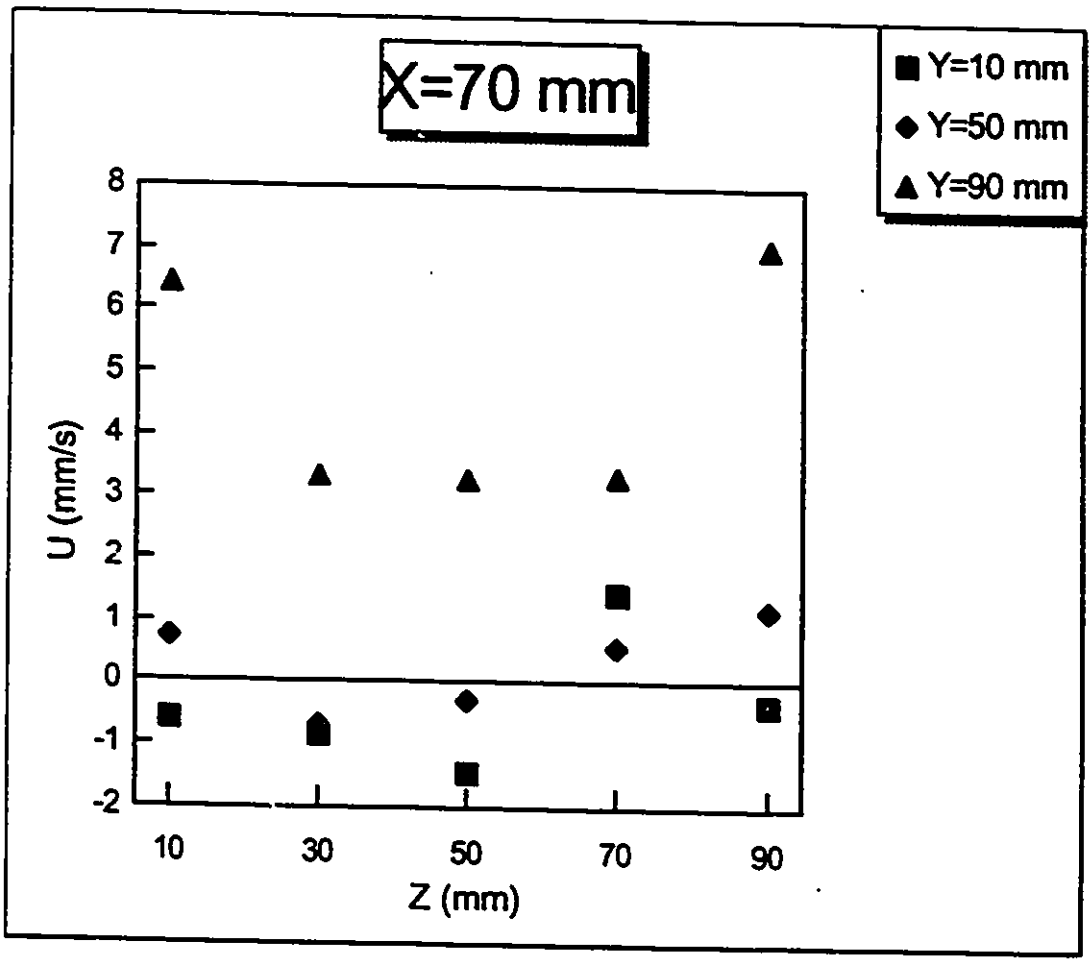

Figure 5.10 U-component velocity profiles on the projected plane X = 70 mm

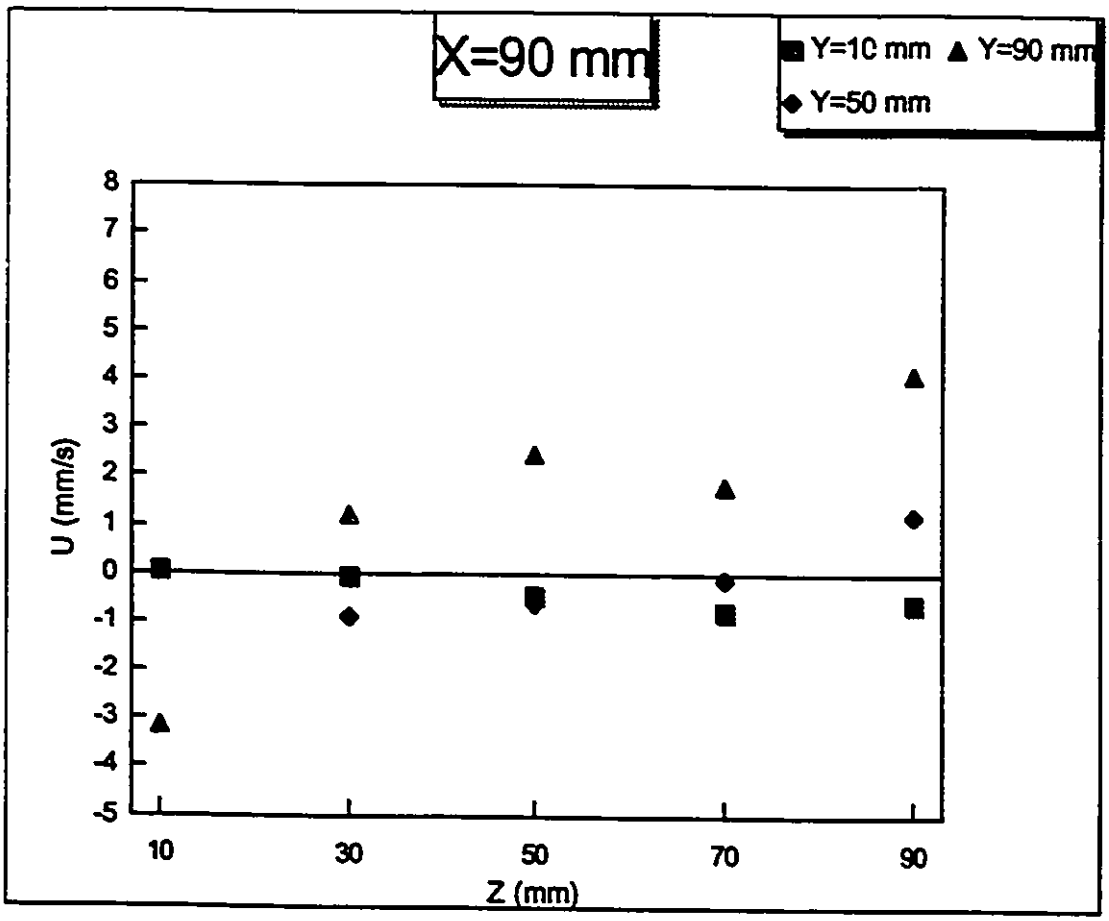

Figure 5.11 U-component velocity profiles on the projected plane X = 90 mm

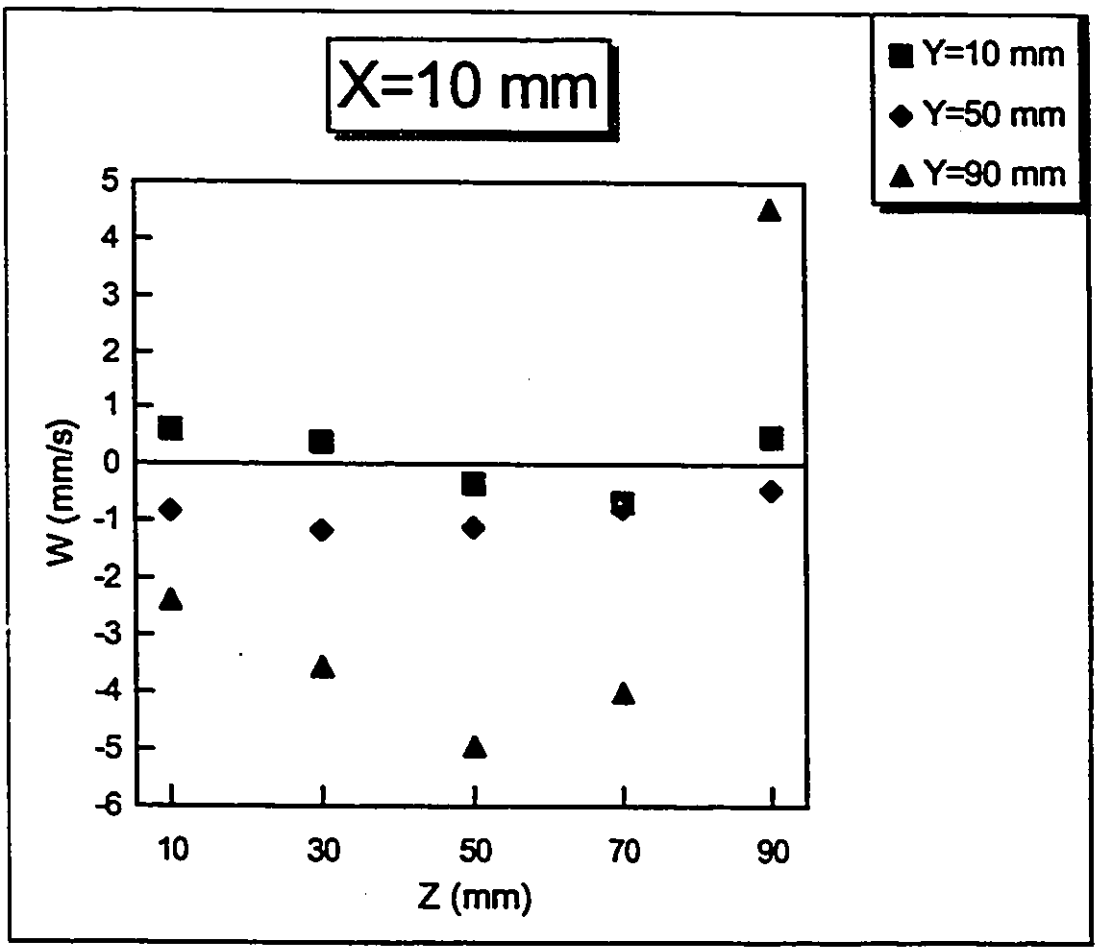

Figure 5.12 W-component velocity profiles on the projected plane X = 10 mm

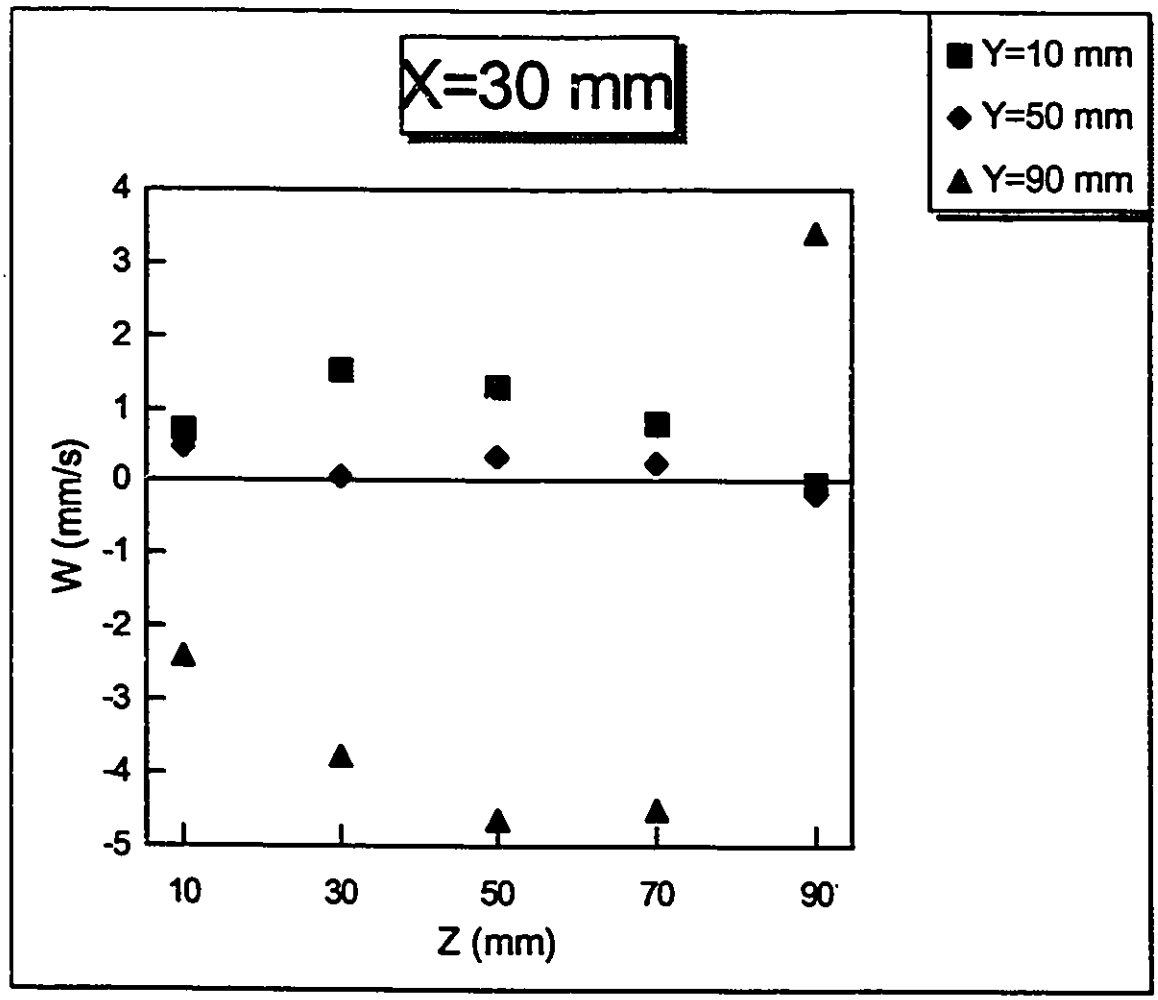

Figure 5.13 W-component velocity profiles on the projected plane X = 30 mm

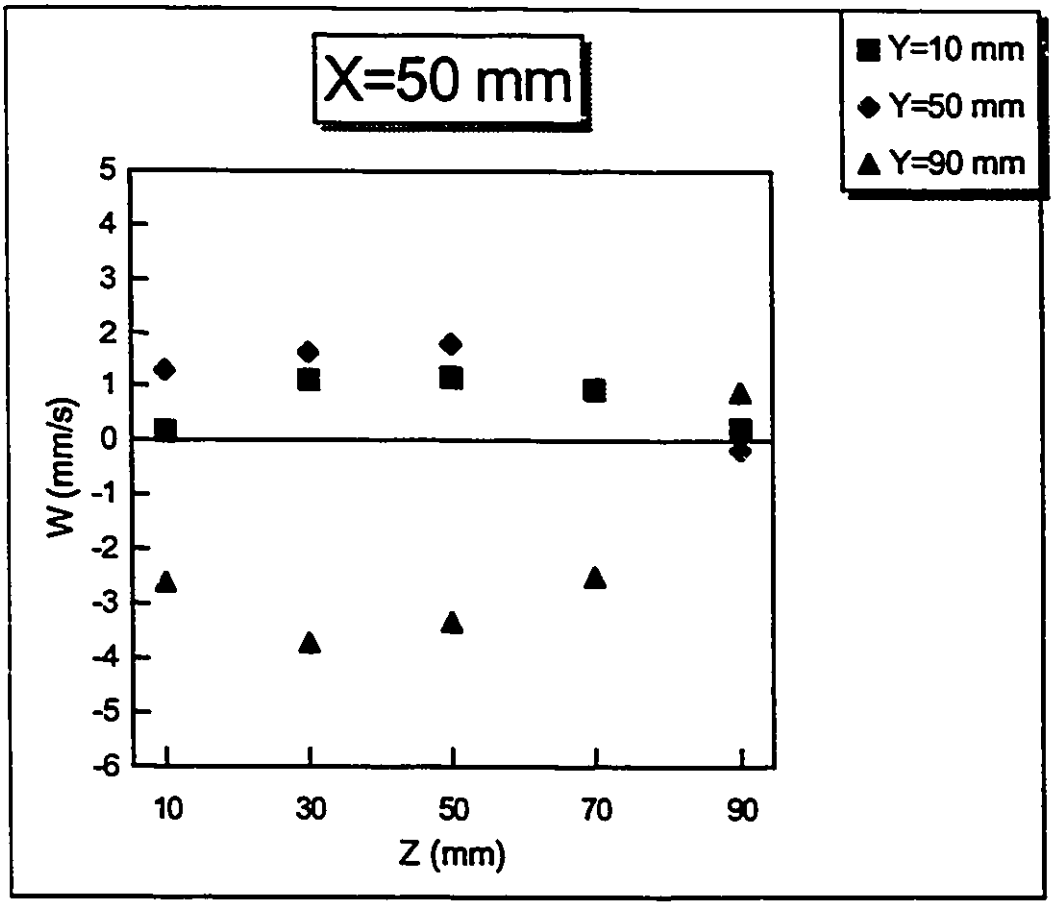

Figure 5.14 W-component velocity profiles on the projected plane X = 50 mm

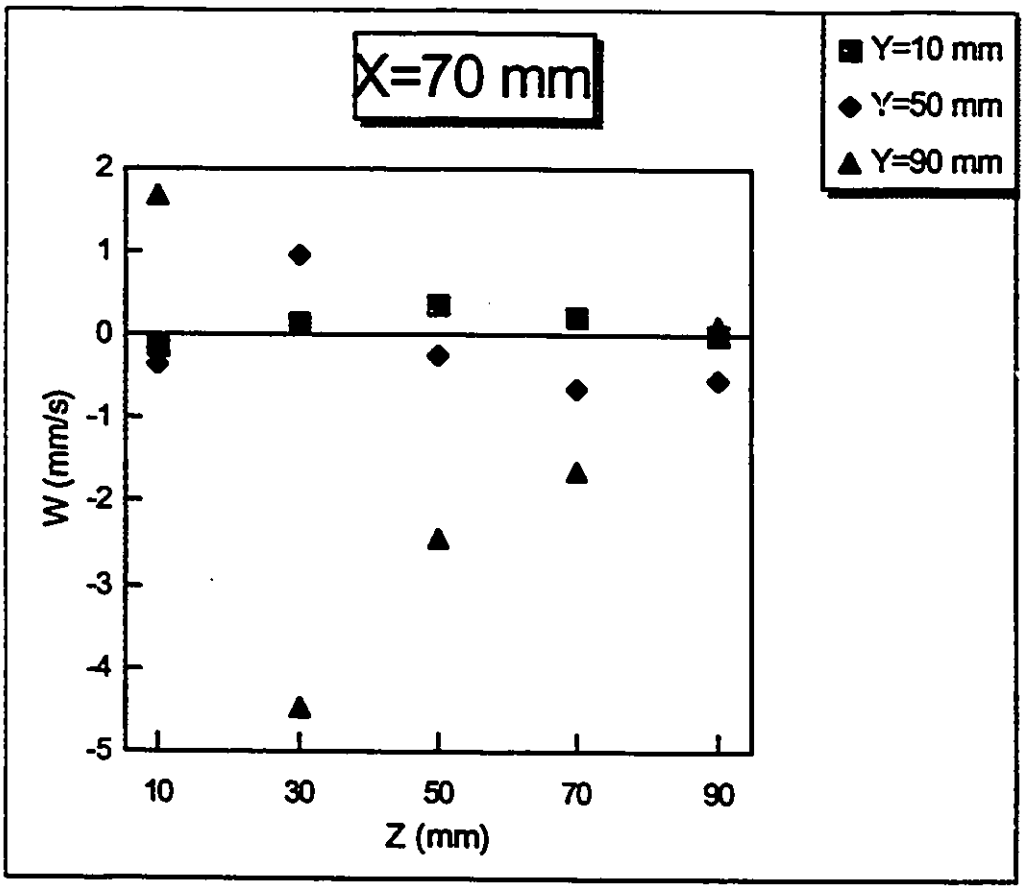

Figure 5.15 W-component velocity profiles on the projected plane X = 70 mm

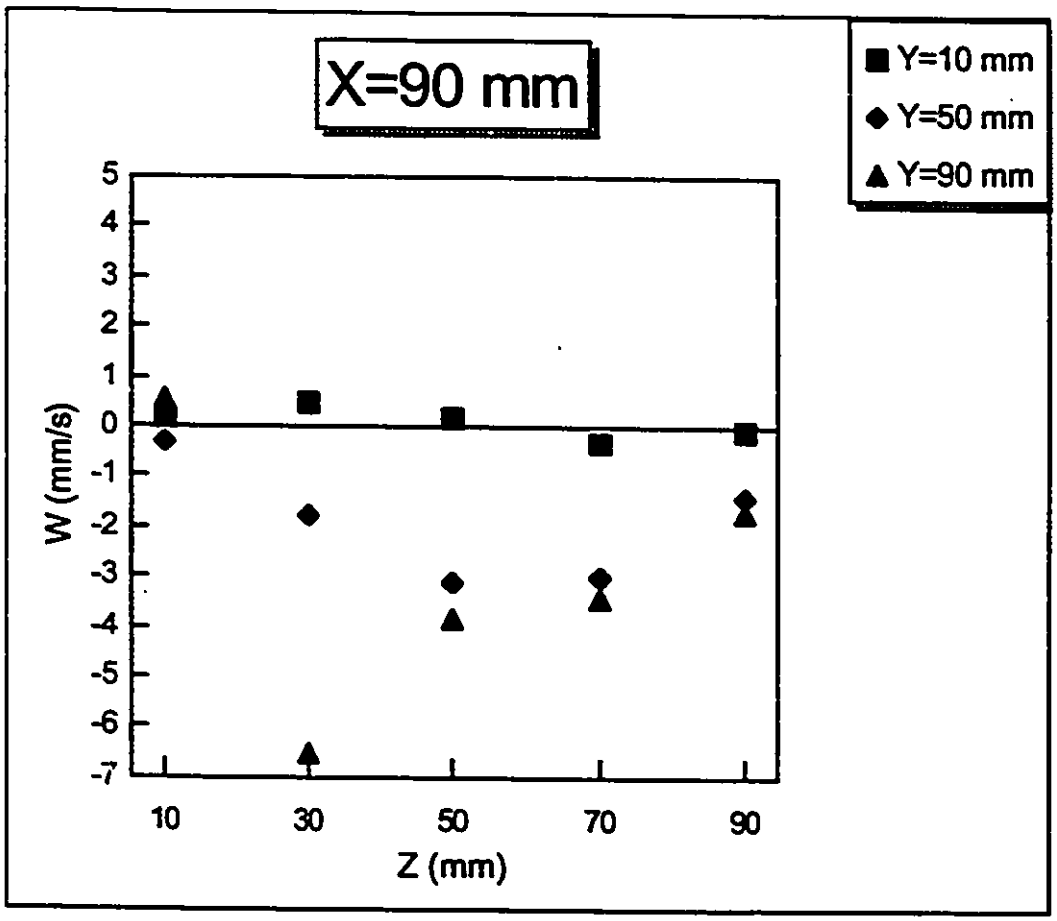

Figure 5.16 W-component velocity profiles on the projected plane X = 90 mm

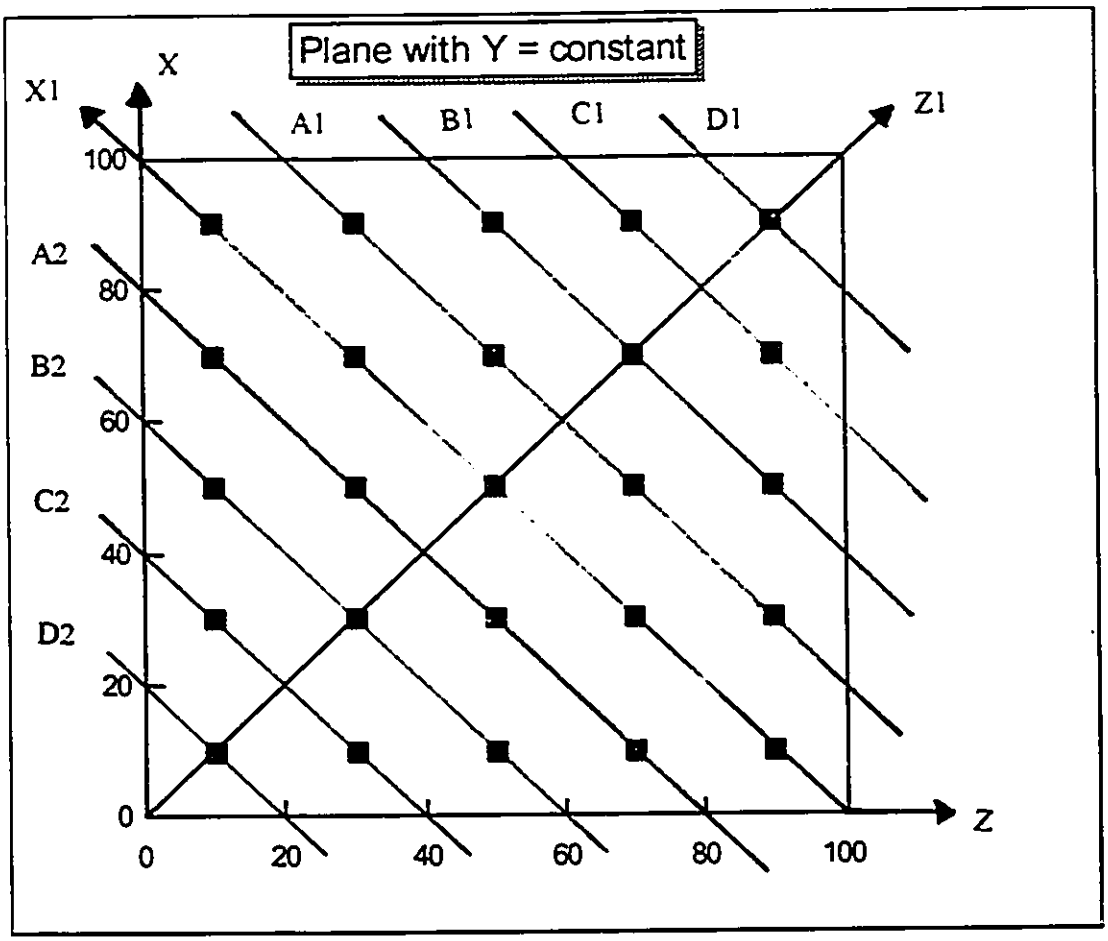

Figure 5.17 Test section showing the plane of symmetry

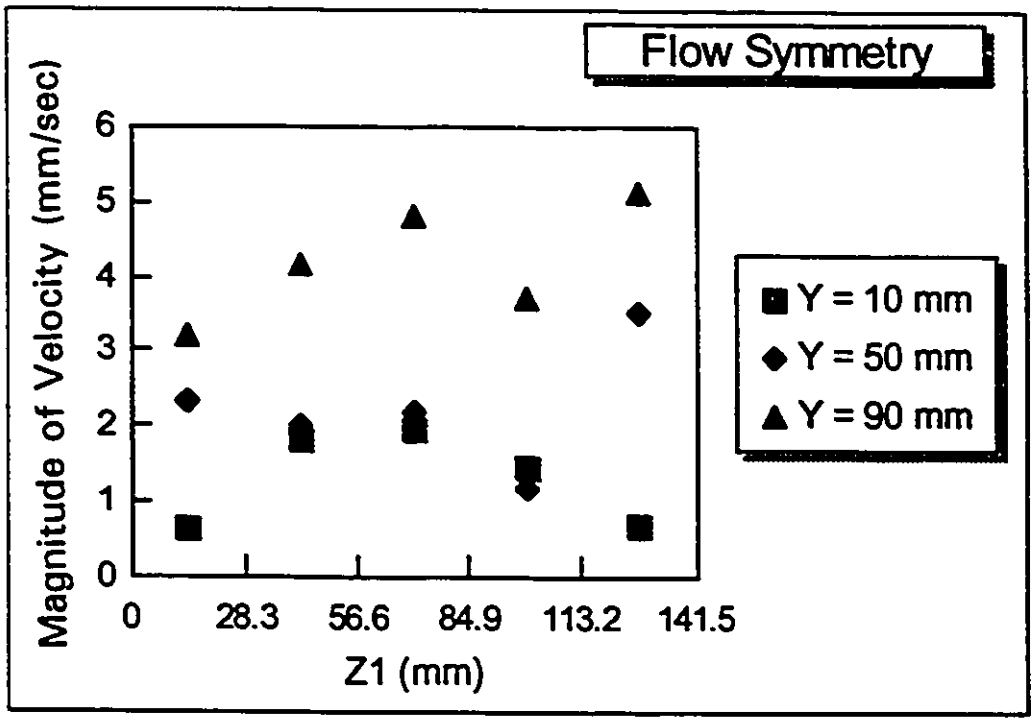

Figure 5.18 Velocity profiles perpendicular to plane of symmetry

Calibration	View #1	View #2	View #3
1	2.442e-006	2.827e-003	3.205e-003
2	-4.104e-005	-4.896e-005	-2.935e-005
3	2.889e-003	-2.182e-004	-1.15e-005
4	-1.324e-001	-1.4571e-001	-1.698e-001
5	4.752e-006	-5.046e-005	-3.268-005
6	-2.913e-003	-2.815e-003	-3.173e-003
7	-8.823e-006	-1.728e-005	-3.25e-006
8	1.288e-001	1.193e-001	1.437e-001
9	-1.007e-003	-4.04e-004	-4.569e-004
10	3.618e-004	5.13e-004	2.739e-004
11	1.688e-005	7.738e-004	9.281e-004
12	-1.168e-000	-4.13e-001	-7.875e-001
13	1.509e+001	-3.592e+001	4.983e+000
14	1.048e+003	1.215e+003	1.872e+002
15	1.632e-002	6.254e-002	2.735e-002
16	5.267e-002	5.503e-002	3.962e-002
17	9.691e-001	9.954e-001	9.891e-001
18	9.739e-001	9.875e-001	9.827e-001

Table 4.1. A typical set of calibration coefficients

Co-ordinate	Calibration error (Average Deviation in mm)		Calibration error (Average Deviation as a Percent of FSV)		Percent improvement of B over A
	Linear (A)	Non-Linear (B)	Linear	Non-Linear	
X	0.176	0.145	0.185	0.152	17.6
Y	0.135	0.106	0.142	0.111	21.5
Z	1.4	1.372	1.47	1.44	2

Table 5.1. Calibration results (average deviation in mm) using stereo views with the target in air

Co-ordinate	Calibration error (Maximum deviation in mm)		Calibration error (Percent of FSV)	
	Linear (A)	Non-Linear (B)	Linear	Non-Linear
X	0.44	0.415	0.46	0.43
Y	0.46	0.43	0.48	0.5
Z	3.56	3.37	3.74	3.5

Table 5.2. Calibration results (maximum deviation in mm) using stereo views with the target in air

Co-ordinate	Calibration error (Average deviation in mm)		Calibration error (Average deviation as a percent of FSV)		Percent improvement of B over A
	Linear (A)	Non-linear (B)	Linear	Non-Linear	
X	0.162	0.135	0.170	0.142	16.6
Y	0.126	0.098	0.132	0.103	22.2
Z	0.148	0.139	0.155	0.146	6

Table 5.3. Calibration results (average deviation in mm) using orthogonal views with the target in air

Co-ordinate	Calibration error (Maximum deviation in mm)		Calibration error (Percent of FSV)	
	Linear (A)	Non-linear (B)	Linear	Non-Linear
X	0.36	0.43	0.38	0.45
Y	0.29	0.254	0.3	0.26
Z	0.58	0.54	0.61	0.57

Table 5.4. Calibration results (maximum deviation in mm) using orthogonal views with the target in air

Co-ordinate	Calibration error (Average deviation in mm)		Calibration error (Average deviation as a percent of FSV)		Percent improvement of B over A
	Linear (A)	Non-Linear (B)	Linear	Non-Linear	
X	0.188	0.144	0.197	0.151	23
Y	0.133	0.111	0.140	0.116	16.5
Z	2.04	1.933	2.140	2.03	5.2

Table 5.5. Calibration results (average deviation in mm) using stereo views with the target in water

Co-ordinate	Calibration error (Maximum deviation in mm)		Calibration error (Percent of FSV)	
	Linear (A)	Non-linear (B)	Linear	Non-Linear
X	0.49	0.49	0.51	0.51
Y	0.51	0.43	0.53	0.45
Z	4.28	3.576	4.5	3.76

Table 5.6. Calibration results (maximum deviation in mm) using stereo views with the target in water

Co-ordinate	Calibration error (Average deviation in mm)		Calibration error (Average deviation as a percent of FSV)		Percent improvement of B over A
	Linear (A)	Non-Linear (B)	Linear	Non-Linear	
X	0.168	0.127	0.176	0.133	24.4
Y	0.135	0.114	0.142	0.120	15.5
Z	0.165	0.162	0.173	0.170	2

Table 5.7. Calibration results (average deviation in mm) using orthogonal views with the target in water

Co-ordinate	Calibration error (Maximum deviation in mm)		Calibration error (Percent of FSV)	
	Linear (A)	Non-linear (B)	Linear	Non-Linear
X	0.41	0.425	0.43	0.44
Y	0.54	0.385	0.57	0.4
Z	0.74	0.523	0.78	0.55

Table 5.8. Calibration results (maximum deviation in mm) using orthogonal views with the target in water

Trial #	x_f (# Pixel)	y_f (# Pixel)
1	61	145.39
2	61.05	145.33
3	60.99	145.33
4	61.03	145.38
5	61.02	145.33
6	61.07	145.3
7	60.99	145.31
8	60.96	145.32
9	61.05	145.29
Mean	61.02	145.33
STD	0.034	0.032
$t_{v,P}$ v=8, P=95	2.306	2.306
Repeatability	0.078	0.073

Table 5.9. Repeatability of calculating the particle-image centroids of calibration target

Trial #1	X (mm)	Y (mm)	Z (mm)
1	90.058	30.18	20.80
2	90.03	30.185	20.761
3	90.054	30.187	20.767
4	90.046	30.165	20.753
5	90.075	30.212	20.785
6	90.066	30.165	20.77
7	90.058	30.174	20.76
8	90.085	30.194	20.731
9	90.088	30.183	20.746
Mean	90.0622	30.182	20.763
Actual Value	90.12	30.21	20.72
STD	0.0175	0.0188	0.0192
$t_{v,p}$ v=8, P=95	2.306	2.306	2.306
Repeatability	0.0405	0.0433	0.0442
Bias	0.0578	0.028	0.043

Table 5.10.Repeatability and bias of position measurement

Co-ordinate	Displacement measured in mm		Calibration error in mm (Difference between tha actual and the experimental)
	Actual (A)	Experimental (B)	
X	1.00	1.125	0.125
Y	1.00	1.134	0.134
Z	1.00	1.145	0.145

Table 5.11 Calibration results using the target in water - Displacement measurement

Z (mm) / Y (mm)	10	30	50	70	90
10	(23.89,7.81,1.8)	(25.0,3.29,3.19)	(16.5,5.46,8.03)	(19.0,3.22,4.85)	(13.4,2.34,4.12)
30	(2.64,25.3,8.7)	(2.5,4.01,5.87)	(5.19,9.53,2.1)	(13.06,2.73,3.2)	(8.11,4.19,4.57)
50	(15.6,8.85,4.07)	(10.09,2.1,2.4)	(1.34,1.57,9.8)	(6.41,3.53,1.67)	(1.95,1.75,5.13)
70	(2.23,6.35,1.18)	(3.54,7.13,10.5)	(11.9,3.92,2.57)	(3.55,3.21,0.45)	(12.04,3.67,3.0)
90	(3.83,4.8,5.46)	(9.57,22.9,1.81)	(2.1,6.97,0.3)	(1.47,2.87,1.01)	(4.85,10.95,5.3)

Table 5.12 Percent difference between experimental and numerical velocity (ΔU, ΔV, ΔW) results (X = 10 mm)

Z (mm) / Y (mm)	10	30	50	70	90
10	(3.8,3.23,4.8)	(17.8,11.23,3.1)	(7.04,8.38,3.06)	(22.9,1.45,1.72)	(4.3,3.23,5.32)
30	(7.13,1.84,5.26)	(18.3,3.25,6.6)	(1.22,11.1,4.87)	(22.9,4.87,2.27)	(18.3,4.8,10.7)
50	(10.3,5.38,11.0)	(6.93,0.9,3.9)	(11.6,1.31,5.04)	(10.9,3.83,17.6)	(12.6,7.82,9.51)
70	(4.07,4.11,0.7)	(8.35,2.55,2.3)	(10.5,5.1,6.82)	(14.4,5.1,10.0)	(3.56,4.06,0.8)
90	(0.66,13.0,4.13)	(3.51,9.95,3.22)	(0.3,2.56,1.86)	(3.55,3.08,2.32	(4.73,4.91,7.55)

Table 5.13 Percent difference between experimental and numerical velocity (ΔU, ΔV, ΔW) results (X = 30 mm)

Z (mm) / Y (mm)	10	30	50	70	90
10	(5.23,2.08,5.29)	(10.0,2.52,0.4)	(0.4,20.9,5.86)	(8.85,7.79,1.06)	(15.5,8.09,3.51)
30	(6.14,4.09,1.36)	(1.5,17.3,2.14)	(0.7,12.6,14.5)	(3.61,6.73,3.02)	(1.19,2.65,6.88)
50	(0.3,4.26,11.7)	(1.02,4.87,8.43)	(3.79,5.15,1.88)	(3.74,4.69,9.41)	(3.52,6.27,15.8)
70	(4.92,3.15,3.78)	(11.3,10.8,7.88)	(20.2,5.04,1.87)	(12.5,10.4,3.21)	(3.39,2.25,3.17)
90	(3.3,3.2,7.27)	(6.26,13.9,2.74)	(3.71,7.82,5.12)	(6.21,6.71,4.4)	(4.22,13.6,4.04)

Table 5.14 Percent difference between experimental and numerical velocity (ΔU, ΔV, ΔW) results (X = 50 mm)

Z (mm) / Y (mm)	10	30	50	70	90
10	(3.64,7.43,18.2)	(5.07,6.63,7.23)	(11.5,7.27,3.83)	(18.2,10.2,6.19)	(8.84,7.35,20.6)
30	(20.9,4.37,8.37)	(4.38,5.32,3.61)	(10.2,8.73,4.9)	(12.6,5.6,2.21)	(4.6,4.77,4.16)
50	(1.87,8.98,5.62)	(4.26,20.6,1.77)	(9.68,4.64,7.58)	(5.95,3.05,3.68)	(0.9,7.42,0.6)
70	(1.36,10.8,6.34)	(15.3,4.9,6.44)	(6.38,1.68,8.29)	(2.64,3.06,3.18)	(6.44,4.93,2.78)
90	(3.52,6.77,5.95)	(8.24,0.2,6.0)	(3.83,9.8,9.3)	(4.84,6.79,7.36)	(2.77,9.31,14.6)

Table 5.15 Percent difference between experimental and numerical velocity (ΔU, ΔV, ΔW) results (X = 70 mm)

Y (mm) \ Z (mm)	10	30	50	70	90
10	(12.1,11.1,5.93)	(7.39,9.28,1.96)	(8.02,13.4,1.45)	(5.14,3.27,7.6)	(1.79,9.28,10.6)
30	(6.35,7.12,3.54)	(5.12,6.36,3.43)	(11.2,3.9,1.1)	(5.91,2.85,1.04)	(8.86,3.6,4.71)
50	(8.95,2,25,3.18)	(3.51,5.46,1.71)	(4.16,3.68,6.68)	(4.69,3.8,5.9)	(17.5,0.6,0.6)
70	(6.41,15.6,4.43)	(5.75,11.0,2.6)	(12.9,7.02,5.03)	(2.88,8.11,4.66)	(10.4,7.4,4.58)
90	(6.0,10.4,3.48)	(11.7,5.58,1.45)	(7.16,5.9,4.28)	(6.38,9.0,3.87)	(4.57,1.17,5.58)

Table 5.16 Percent difference between experimental and numerical velocity (ΔU, ΔV, ΔW) results (X = 90 mm)

Velocity Component	Comparison of velocity values obtained with 10^{-3} and 10^{-4} residuals	Comparison of velocity values obtained with 10^{-4} and 10^{-5} residuals
	Maximum Difference mm/s	Maximum Difference mm/s
U	0.01	0.001
V	0.009	0.002
W	0.007	0.001

Table 5.17 Comparison of the the velocity values obtained from the numerical simulation for different sums of residuals

Velocity Component	Maximum Difference (mm/s)
U	0.242
V	0.310
W	0.357

Table 5.18 Comparison of velocity values for different grid sizes (12x12x12 Vs 21x21x21)

Appendix A

Calibration Curve

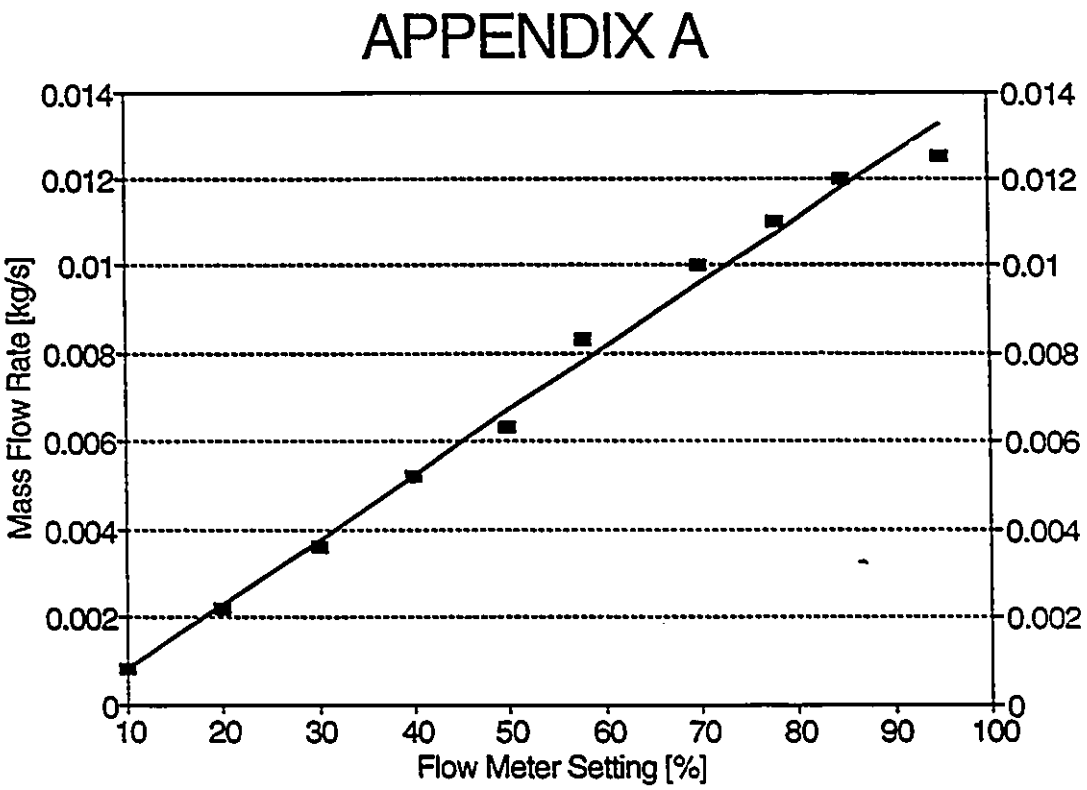

Figure A.1 A plot of the flow meter calibration curve

Appendix B

Camera Transformation

The camera and world co-ordinate systems are brought into alignment by applying a set of transformations. After this, the perspective transformation is applied to obtain the image plane co-ordinates of any given world co-ordinate.

The perspective transformation matrix, P, is the linear transformation that transforms an object into its image point.

$$P = \begin{bmatrix} 1 & 0 & 0 & 0 \\ 0 & 1 & 0 & 0 \\ 0 & 0 & 1 & 0 \\ 0 & 0 & 1/f & 0 \end{bmatrix} \tag{B.1}$$

where f is the focal length of the camera.

The translation of the origin of the world co-ordinate system

$$G = \begin{bmatrix} 1 & 0 & 0 & -X_0 \\ 0 & 1 & 0 & -Y_0 \\ 0 & 0 & 1 & -Z_0 \\ 0 & 0 & 0 & 1 \end{bmatrix} \tag{B.2}$$

where X_0 , Y_0 , Z_0 are the co-ordinates of the camera lens centre. The rotation matrix is

$$R = \begin{bmatrix} \cos\theta & \sin\theta & 0 & 0 \\ -\sin\theta\cos\alpha & \cos\theta\cos\alpha & \sin\alpha & 0 \\ \sin\theta\sin\alpha & -\cos\theta\sin\alpha & \cos\alpha & 0 \\ 0 & 0 & 0 & 1 \end{bmatrix} \quad \text{(B.3)}$$

where θ is the pan angle and α is the tilt angle. The translation from the perspective centre to the image plane centre is

$$L = \begin{bmatrix} 1 & 0 & 0 & 0 \\ 0 & 1 & 0 & 0 \\ 0 & 0 & 1 & -f \\ 0 & 0 & 0 & 1 \end{bmatrix} \quad \text{(B.4)}$$

The overall transformation matrix is

$$H = PLGR \quad \text{(B.5)}$$

Appendix C

Fourier Transform

Discrete Fourier Transform [Gonzalez and Wintz, 1987, Larijani, 1991]

The discrete Fourier transform (DFT) pair that applies to a sampled function is given by:

$$F(o) = \frac{1}{N}\sum_{s=0}^{N-1} f(s)\exp(-j\frac{2\pi os}{N}) \qquad o=0,1,2,...,N-1 \qquad \text{(c.1)}$$

and

$$f(s) = \sum_{o=0}^{N-1} F(o)\exp(j\frac{2\pi os}{N}) \qquad s=0,1,2,...,N-1 \qquad \text{(c.2)}$$

For a three variable case, the DFT pair is given by the following equations

$$F(o_1,o_2,o_3) = \frac{1}{N_1N_2N_3}\sum_{s_1=0}^{N_1-1}\sum_{s_2=0}^{N_2-1}\sum_{s_3=0}^{N_3-1} f(s_1,s_2,s_3)\exp[-j2\pi[(\frac{o_1s_1}{N_1}+\frac{o_2s_2}{N_2}+\frac{o_3s_3}{N_3})] \qquad \text{(c.3)}$$

for $o_1 = 0,1,2,...,N_1 - 1$, $o_2 = 0,1,2,..,N_2 - 1$ and $o_3 = 0,1,2,...,N_3 - 1$ and

$$f(s_1,s_2,s_3) = \sum_{o_1=0}^{N_1-1}\sum_{o_2=0}^{N_2-1}\sum_{o_3=0}^{N_3-1} F(o_1,o_2,o_3)\exp[j2\pi(\frac{o_1s_1}{N_1}+\frac{o_2s_2}{N_2}+\frac{o_3s_3}{N_3}) \qquad \text{(c.4)}$$

for $s_1 = 0,1,2..., N_1 - 1$, $s_2 = 0,1,2..., N_2 - 1$ and $s_3 = 0,1,2,..., N_3 - 1$.

When images are sampled in a square array ($N_1 = N_2 = N_3$), equations (c.3) and (c.4) can be expressed as

$$F(o_1, o_2, o_3) = \frac{1}{N} \sum_{s_1=0}^{N-1} \sum_{s_2=0}^{N-1} \sum_{s_3=0}^{N-1} f(s_1, s_2, s_3) \exp[-j2\pi(\frac{o_1 s_1 + o_2 s_2 + o_3 s_3}{N})] \qquad (c.5)$$

for $o_1, o_2, o_3 = 0,1,2,..., N - 1$ and

$$f(s_1, s_2, s_3) = \frac{1}{N} \sum_{o_1=0}^{N-1} \sum_{o_2=0}^{N-1} \sum_{o_3=0}^{N-1} F(o_1, o_2, o_3) \exp[j2\pi(\frac{o_1 s_1 + o_2 s_2 + o_3 s_3}{N})] \qquad (c.6)$$

for $s_1, s_2, s_3 = 0,1,2, ..., N - 1$.

Where f(n) is a sequence of real numbers and N is even, equation (c.2) can be written as a sum of sine and cosine terms as:

$$f(s) = F_R(o) + \Sigma 2[F_R(o)\cos\frac{2\pi os}{N} - F_I(o)\sin\frac{2\pi os}{N}] + F_R(N/2)\cos\pi s \qquad (c.7)$$

where $F(o) = F_R(o) + jF_I(o)$.

The DFT can be easily extended to 3-D cases. When $f(s_1,s_2,s_3)$ is a sequence of real numbers and N_1, N_2 and N_3 are even, equation (c.4) can be expressed as:

$$f(s_2, s_2, s_3) = \sum_{o_3=0}^{N_3-1} \sum_{o_2=0}^{N_2-1} \sum_{o_1=0}^{N_1-1} F_R(o_1, o_2, o_3)\cos(2\pi[\frac{o_1 s_1}{N_1} + \frac{o_2 s_2}{N_2} + \frac{o_3 s_3}{N_3}])$$
$$+ \Sigma\Sigma\Sigma\, F_I(o_1, o_2, o_3)\sin(2\pi[\frac{o_1 s_1}{N_1} + \frac{o_2 s_2}{N_2} + \frac{o_3 s_3}{N_3}]) \qquad (c.8)$$

From equations (c.7) and (c.8), it is clear that the DFT of a function is essentially the amplitude coefficients of the sine and cosine functions that make up that function.

The DFT given in (c.5) can be expressed in separable form as:

$$F(o_1, o_2, o_3) = \frac{1}{N} \sum_{s_2=0}^{N-1} \sum_{s_3=0}^{N-1} \exp[-j2\pi(\frac{o_2 s_2 + o_3 s_3}{N})] \sum_{s_1=0}^{N-1} f(s_1, s_2, s_3) \exp[\frac{-j2\pi o_1 s_1}{N}] \tag{c.9}$$

The main advantage of the separability property is that $F(o_1, o_2, o_3)$ or $f(s_1, s_2, s_3)$ can be obtained in three steps by successive application of 1-D Fourier transforms or its inverse.

The Fast Fourier Transform [Larijani, 1991]

In its basic form, the DFT is very expensive to implement because it requires N complex additions and multiplications for each coefficient computed. Since there are N coefficients, a complete N-point DFT requires N^2 complex operations. By properly decomposing equation (c.1), the number of multiplications and additions can be made proportional to $N \log_2 N$. The decomposition procedure is called the fast Fourier transform (FFT) algorithm.

The following example demonstrates how a four-point DFT can be calculated more efficiently using the FFT. From the data $f(0), f(1), f(2), f(3)$, the DFT generates the following coefficients:

$$\begin{aligned}
F(0) &= f(0)e^{\frac{-j2\pi 0}{4}} + f(1)e^{\frac{-j2\pi 0}{4}} + f(2)e^{\frac{-j2\pi 0}{4}} + f(3)e^{\frac{-j2\pi 0}{4}} \\
F(1) &= f(0)e^{\frac{-j2\pi 0}{4}} + f(1)e^{\frac{-j2\pi 1}{4}} + f(2)e^{\frac{-j2\pi 2}{4}} + f(3)e^{\frac{-j2\pi 3}{4}} \\
F(2) &= f(0)e^{\frac{-j2\pi 0}{4}} + f(1)e^{\frac{-j2\pi 2}{4}} + f(2)e^{\frac{-j2\pi 4}{4}} + f(3)e^{\frac{-j2\pi 6}{4}} \\
F(3) &= f(0)e^{\frac{-j2\pi 0}{4}} + f(1)e^{\frac{-j2\pi 3}{4}} + f(2)e^{\frac{-j2\pi 6}{4}} + f(3)e^{\frac{-j2\pi 9}{4}}
\end{aligned} \tag{c.10}$$

Since the term $e^{\frac{-j2\pi l}{4}}$ is periodic with a period of 4, the last two terms of $F(2)$ and $F(3)$ can be written with similar arguments:

$$F(2) = f(0)e^{\frac{-j2\pi 0}{4}} + f(1)e^{\frac{-j2\pi 2}{4}} + f(2)e^{\frac{-j2\pi 0}{4}} + f(3)e^{\frac{-j2\pi 2}{4}}$$

$$F(3) = f(0)e^{\frac{-j2\pi 0}{4}} + f(1)e^{\frac{-j2\pi 3}{4}} + f(2)e^{\frac{-j2\pi 2}{4}} + f(3)e^{\frac{-j2\pi 1}{4}} \qquad \text{(c.11)}$$

From equations (c.10) and (c.11), it can be observed that the data is ordered in pairs: $\{f(0), f(2)$ and $f(1), f(3)\}$. The above equations can be re-arranged as:

$$F(0) = \{f(0)+f(2)\}+\{f(1)+f(3)\}$$

$$F(1) = \{f(0)+f(2)e^{\frac{-j2\pi 2}{4}}\)+(f(1)+f(3)e^{\frac{-j2\pi 2}{4}})e^{\frac{-j2\pi}{4}}$$

$$F(2) = \{f(0)+f(2)\}+\{f(1)+f(3)\}e^{\frac{-j2\pi 2}{4}}$$

$$F(3) = \{f(0)+f(2)e^{\frac{-j2\pi 2}{4}}\}+\{f(1)+f(3)e^{\frac{-j2\pi 2}{4}})e^{\frac{-j2\pi 3}{4}} \qquad \text{(c.12)}$$

The equations in (c.12) will compute the same coefficients as the DFT of equation (c.10), but require only 12 complex additions and 5 complex multiplications. Such reorganizations are possible for any DFT with length that is a power of 2 (2, 8, 16, 32,...). This faster implementation of the DFT is called the radix-2 FFT.

Appendix D Comparison of the Numerical Schemes

Y (mm) \ Z (mm)	10	30	50	70	90
10	(4.36,1.27,0.25)	(2.04,0.4,0.2)	(2.27,0.6,0.6)	(15.1,0.4,0.55)	(0.46,0.47,0.35)
30	(0.94,0.33,0.92)	(0.33,0.86,0.72)	(0.78,0.08,1.03)	(1.79,0.39,0.5)	(1.72,0.44,0.45)
50	(0.55,0.54,0.47)	(1.39,0.46,0.11)	(2.18,0.03,0.3)	(10.2,0.22,0.39)	(2.16,0.62,0.61)
70	(0.48,0.17,0.13)	(3.95,0.13,0.28)	(2.4,0.06,0.69)	(2.57,0.49,0.22)	(0.34,0.58,0.22)
90	(0.31,1.8,0.3)	(1.26,1.64,0.21)	(0.35,0.31,0.59)	(1.79,0.56,0.24)	(0.25,0.14,0.1)

Table D.1 Percent difference between velocity values computed from the two numerical schemes (ΔU, ΔV, ΔW) at (X = 10 mm)

Y (mm) \ Z (mm)	10	30	50	70	90
10	(2.63,0.44,0.18)	(1.21,0.86,0.07)	(0.79,1.8,0.14)	(4.63,0.22,0.31)	(1.27,0.24,6.18)
30	(0.87,0.24,0.26)	(1.18,0.11,0.33)	(0.77,0.96,0.3)	(11.4,0.72,0.41)	(2.94,0.77,1.61)
50	(0.45,0.11,1.02)	(2.44,0.1,2.03))	(0.68,0.31,0.36)	(2.54,0.07,0.83)	(0.55,0.96,1.77)
70	(0.14,1.65,0.59)	(0.36,0.22,0.35)	(0.78,0.29,0.8))	(8.75,0.09,10.7)	(0.63,0.48,0.72)
90	(1.26,1.07,0.08)	(0.62,2.5,0.24)	(0.2,0.65,0.21)	(0.25,0.17,0.28)	(0.58,0.46,0.06)

Table D.2 Percent difference between velocity values computed from the two numerical schemes (ΔU, ΔV, ΔW) at (X = 30 mm)

Z (mm) / Y (mm)	10	30	50	70	90
10	(0.66,1.33,0.5)	(1.55,0.54,0.37)	(0.2,2.25,0.22)	(0.11,1.09,0.18)	(2.0,0.29,0.86))
30	(2.32,0.26,0.52)	(1.94,0.19,0.73)	(0.42,1.24,0.16)	(0.68,1.37,0.22)	(0.67,1.01,1.01)
50	(0.5,0.12,0.28)	(1.06,0.79,1.31)	(0.8,0.11,0.1)	(0.65,2.24,0.23)	(0.43,0.02,2.36)
70	(0.67,0.2,0.19)	(0.12,2.26,0.9)	(2.28,0.31,0.53)	(0.8,1.13,0.53)	(0.19,0.06,0.32)
90	(0.11,0.33,0.07)	(0.48,0.77,0.05)	(0.63,0.29,0.42)	(0.85,0.37,0.12)	(0.42,0.58,0.17)

Table D.3 Percent difference between velocity values computed from the two numerical schemes (ΔU, ΔV, ΔW) at ($X = 50$ mm)

Z (mm) / Y (mm)	10	30	50	70	90
10	(0.52,0.56,1.78)	(0.92,0.18,1.91)	(0.41,3.92,0.43)	(0.23,0.97,0.67)	(1.81,0.09,7.78)
30	(1.53,0.35,1.22)	(0.61,0.54,4.07)	(3.24,5.17,1.44)	(7.73,0.28,0.25)	(3.74,0.28,0.78)
50	(0.99,0.65,0.7)	(0.42,2.17,0.28)	(1.84,0.49,1.0)	(0.94,0.25,0.43)	(0.49,1.22,0.98)
70	(1.74,0.82,0.29)	(4.17,0.12,0.28)	(2.65,0.54,0.12)	(0.71,0.15,0.32)	(0.74,0.59,0.24)
90	(0.49,0.51,0.28)	(0.83,0.46,0.84)	(0.64,0.62,0.62)	(0.09,0.7,1.64)	(0.29,0.38,0.66)

Table D.4 Percent difference between velocity values computed from the two numerical schemes (ΔU, ΔV, ΔW) at (X = 70 mm)

Z (mm) / Y (mm)	10	30	50	70	90
10	(0.29,0.38,0.66)	(4.97,1.38,0.4)	(4.94,3.84,0.56)	(0.66,0.92,2.44)	(0.75,0.41,1.65)
30	(0.66,0.5,2.04))	(6.78,1.05,6.15)	(0.82,0.67,0.36)	(0.18,0.1,0.25)	(0.76,0.38,0.19)
50	(4.17,0.09,0.41)	(9.26,14.5,1.05)	(0.55,0.8,0.12)	(0.31,0.03,0.12)	(1.87,0.08,0.04)
70	(0.42,0.31,0.25)	(0.52,0.25,0.48)	(0.49,0.22,0.09)	(1.22,0.78,0.15)	(2.61,0.11,0.19)
90	(1.39,0.13,0.3)	(0.12,0.15,0.34)	(1.96,0.67,0.18)	(0.14,0.11,0.34)	(0.14,0.08,0.29)

Table D.5 % Percent difference between velocity values computed from the two numerical schemes (ΔU, ΔV, ΔW) at (X = 90 mm)

Appendix E

Uncertainty Analysis

The uncertainty analysis was done using the Kline and Mclintock's method [Kline and McClintock, 1953]. The uncertainty in a variable R can be expressed as:

$$R = R(a_1, a_2, ..., a_n)$$

$$W_R = \sqrt{(\frac{\partial R}{\partial a_1} W_{a_1})^2 + (\frac{\partial R}{\partial a_2} W_{a_2})^2 + ... + (\frac{\partial R}{\partial a_n} W_{a_n})^2}$$

where W_R is the uncertainty in R and W_{a1} , W_{a2} are the uncertainties in a_1 , a_2 ..., a_n respectively.

Velocity

The uncertainty analysis is done using data for a Reynolds number of 400 at X = 30, Y = 90 and Z = 70. The velocity at any location is calculated using the following expression:

$$U = \frac{\Delta X}{\Delta t}$$

$\Delta t = \frac{1}{5} \pm \frac{1}{500}$ secs

$\Delta X = 1.05 \pm 0.125$ mm

$$W_U = \sqrt{(\frac{\partial U}{\partial \Delta X} W_{\Delta x})^2 + (\frac{\partial U}{\partial \Delta t} W_{\Delta t})^2}$$

$$= 5.25 \pm 0.508 \text{ mm/s } (\pm 9.6\%)$$

Vita Auctoris

Name:	Satya Kurada
Place of Birth:	Ottawa, Ontario, Canada
Year of Birth:	1964
Education:	B.V.K. Junior College, Vizag, India 1978-1980 Department of Mechanical Engineering Andhra University. Vizag, India 1980-1984 B.E. Department of Mechanical Engineering University of Windsor, Windsor, Ontario, Canada 1986-1988 M.A.Sc. University of Windsor, Windsor, Ontario, Canada 1989-1995 Currently a candidate for the Degree of Doctor of Philosophy in Mechanical Engineering.